

AD-A124 819

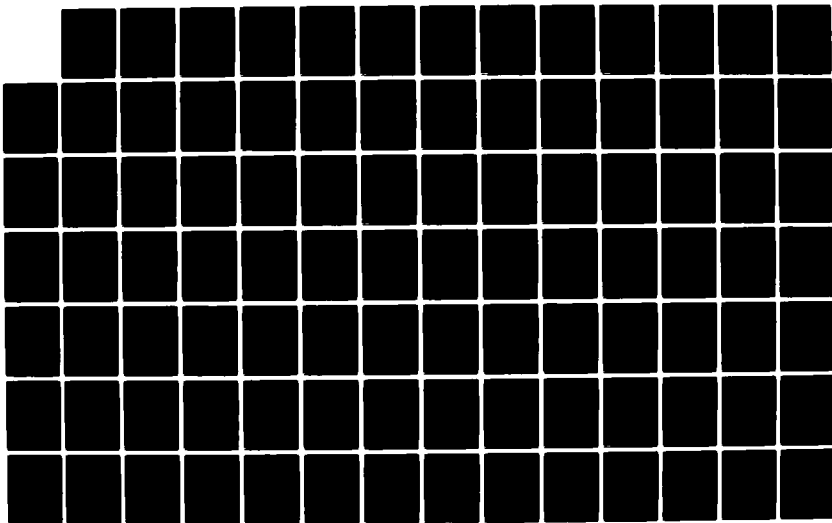
INVESTIGATION OF THE COUPLING OF UNSTEADY LIFT TO LOW
ORDER ACOUSTIC DUCT..(U) PENNSYLVANIA STATE UNIV
UNIVERSITY PARK APPLIED RESEARCH LAB.. J P COWAN
17 JUN 82 ARL/PSU/TM-82-137

1/2

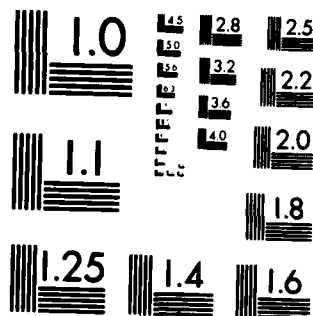
UNCLASSIFIED

F/G 20/1

NL



M-2



MICROCOPY RESOLUTION TEST CHART
NATIONAL BUREAU OF STANDARDS 1963 A

(6)

INVESTIGATION OF THE COUPLING OF UNSTEADY LIFT TO LOW
ORDER ACOUSTIC DUCT MODES IN AN AXIAL FLOW FAN

James P. Cowan

Technical Memorandum
File No. TM 82-137
June 17, 1982
Contract No. N00024-79-C-6043

Copy No. 5

The Pennsylvania State University
Intercollege Research Programs and Facilities
APPLIED RESEARCH LABORATORY
Post Office Box 30
State College, PA 16801

APPROVED FOR PUBLIC RELEASE
DISTRIBUTION UNLIMITED

NAVY DEPARTMENT
NAVAL SEA SYSTEMS COMMAND

DTIC
ELECTE
FEB 23 1983
S E D

83 02 023 109

AD A124819

DTIC FILE COPY

UNCLASSIFIED

SECURITY CLASSIFICATION OF THIS PAGE (When Data Entered)

REPORT DOCUMENTATION PAGE		READ INSTRUCTIONS BEFORE COMPLETING FORM
1. REPORT NUMBER 82-137	2. GOVT ACCESSION NO. A124819	3. RECIPIENT'S CATALOG NUMBER
4. TITLE (and Subtitle) INVESTIGATION OF THE COUPLING OF UNSTEADY LIFT TO LOW ORDER ACOUSTIC DUCT MODES IN AN AXIAL FLOW FAN		5. TYPE OF REPORT & PERIOD COVERED M.S. Thesis, November 1982
7. AUTHOR(s) James Philip Cowan		6. PERFORMING ORG. REPORT NUMBER 82-137
9. PERFORMING ORGANIZATION NAME AND ADDRESS The Pennsylvania State University Applied Research Laboratory, P.O. Box 30 State College, PA 16801		8. CONTRACT OR GRANT NUMBER(s) N00024-79-C-6043
11. CONTROLLING OFFICE NAME AND ADDRESS Naval Sea Systems Command Department of the Navy Washington, DC 20362		10. PROGRAM ELEMENT, PROJECT, TASK AREA & WORK UNIT NUMBERS
14. MONITORING AGENCY NAME & ADDRESS (if different from Controlling Office)		12. REPORT DATE June 17, 1982
		13. NUMBER OF PAGES 131 pages
		15. SECURITY CLASS. (of this report)
		15a. DECLASSIFICATION/DOWNGRADING SCHEDULE
16. DISTRIBUTION STATEMENT (of this Report) Approved for public release, distribution unlimited, per NSSC (Naval Sea Systems Command), July 7, 1982		
17. DISTRIBUTION STATEMENT (of the abstract entered in Block 20, if different from Report)		
18. SUPPLEMENTARY NOTES		
19. KEY WORDS (Continue on reverse side if necessary and identify by block number) unsteady, lift		
20. ABSTRACT (Continue on reverse side if necessary and identify by block number) By using flow distortion screens, the plane wave (0,0) and first higher order (-1,0) and (1,0) spinning modes were generated in a low-speed axial flow fan. The perpendicular unsteady lift force on a segment of a nine-bladed rotor and the acoustic pressure along the duct were measured simultaneously by a strain gage sensor and a flush-mounted microphone, respectively. The total pressure field downstream of the screens was measured by circumferentially traversing a Kiel probe.		

DD FORM 1473

JAN 73

EDITION OF 1 NOV 65 IS OBSOLETE

UNCLASSIFIED

SECURITY CLASSIFICATION OF THIS PAGE (When Data Entered)

UNCLASSIFIED

SECURITY CLASSIFICATION OF THIS PAGE(When Data Entered)

The typical signal-to-noise ratio was sufficiently high for the desired signal isolation with a spectrum analyzer. A phase-locked ensemble averaging technique was used to obtain amplitude and phase measurements of the periodic unsteady signals.

Standing waves set up in the duct between the rotor and duct inlet seemed to cause a back-reaction effect which resulted in an increase and reduction of the unsteady lift force above and below expected levels. If these effects are taken into account, theoretical predictions coupling unsteady lift to acoustic far field pressure levels conform to measured data. Therefore, it is concluded that there is a definite coupling between unsteady lift and acoustic pressure in the duct, yet determination of an unambiguous coupling factor would require more extensive data acquisition.

Accession For	
NTIS GRA&I	<input checked="checked" type="checkbox"/>
DTIC TAB	<input type="checkbox"/>
Unannounced	<input type="checkbox"/>
Justification	
By	
Distribution	
Availability Codes	
Dist	



UNCLASSIFIED

SECURITY CLASSIFICATION OF THIS PAGE(When Data Entered)

ABSTRACT

By using flow distortion screens, the plane wave (0,0) and first higher order (-1,0) and (1,0) spinning modes were generated in a low-speed axial flow fan. The perpendicular unsteady lift force on a segment of a nine-bladed rotor and the acoustic pressure along the duct were measured simultaneously by a strain gage sensor and a flush-mounted microphone, respectively. The total pressure field downstream of the screens was measured by circumferentially traversing a Kiel probe.

The typical signal-to-noise ratio was sufficiently high for the desired signal isolation with a spectrum analyzer. A phase-locked ensemble averaging technique was used to obtain amplitude and phase measurements of the periodic unsteady signals.

Standing waves set up in the duct between the rotor and duct inlet seemed to cause a back-reaction effect which resulted in an increase and reduction of the unsteady lift force above and below expected levels. If these effects are taken into account, theoretical predictions coupling unsteady lift to acoustic far-field pressure levels conform to measured data. Therefore, it is concluded that there is a definite coupling between unsteady lift and acoustic pressure in the duct, yet determination of an unambiguous coupling factor would require more extensive data acquisition.

TABLE OF CONTENTS

	<u>Page</u>
ABSTRACT	iii
LIST OF FIGURES	vi
LIST OF TABLES	x
LIST OF SYMBOLS	xi
ACKNOWLEDGMENTS	xiv
CHAPTER	
I. INTRODUCTION	1
1.1 The Basis of Compressor Noise Investigation	1
1.1.1 Generation	2
1.1.2 Transmission	3
1.1.3 Radiation	6
1.2 Previous Theoretical and Experimental Relevant Work	6
1.3 Object of This Work	12
II. EXPERIMENTAL ASPECTS	13
2.1 Introduction	13
2.2 Apparatus	17
2.3 Instrumentation	20
2.3.1 Velocity Survey	20
2.3.2 Acoustic and Lift Measurements	22
2.4 Calibration	24
2.4.1 Strain Gage Calibration	24
2.4.2 Microphone Calibration	26
2.4.3 Spectrum Analyzer Calibration	29
2.4.4 Distortion Screens	29
2.5 Measurement	33
2.6 Experimental Accuracy, Repeatability, and Possible Sources of Error	37
2.6.1 Velocity Surveys	37
2.6.2 Unsteady Life and Acoustic Pressure Measurement	40
2.7 Background Levels and Data Validity	41

TABLE OF CONTENTS (continued)

	<u>Page</u>
III. THEORY, RESULTS, AND COMPARISON WITH THEORY	46
3.1 Acoustic Fields in Annular Ducts	46
3.1.1 General Acoustic Pressure Field	46
3.1.2 Standing Wave Phenomena	49
3.2 Theoretical Coupling of Unsteady Lift Force to Acoustic Modal Pressures	56
3.3 Comparison of Experimental Results With Theoretical Predution	63
3.3.1 Propagation and Decay of Acoustic Modal Pressure Fields	63
3.3.2 Distortion Screen Performance	66
3.3.3 Unsteady Lift Force	72
3.3.4 Acoustic Modal Pressure	82
3.3.5 Coupling of Unsteady Lift to Acoustic Modal Pressures	91
IV. SUMMARY, CONCLUSIONS, AND RECOMMENDATIONS FOR FURTHER RESEARCH	97
4.1 Summary and Conclusions	97
4.2 Recommendations for Further Research	99
REFERENCES	101
APPENDIX A: DISTORTION SCREEN DESIGN	104
APPENDIX B: DYNAMIC LIFT GAGE CALIBRATION	110
APPENDIX C: EFFECTS OF VARYING FLOW COEFFICIENTS	117
APPENDIX D: CORRELATION OF MEASURED AND HARMONIC LEVELS	123

LIST OF FIGURES

<u>Figure</u>	<u>Page</u>
1. Transmission Characteristics of Acoustic Duct Modes	5
2. Rotor-Stator Flow Interaction for Cascades of Airfoils	7
3. Schematic Diagram of Noise Mechanisms and Experimental Measurements	14
4. The Instrumented Rotor Blade	16
5. The Axial Flow Research Fan (AFRF)	18
6. Relative Locations of Distortion Screen, Rotor Cascade, and Microphone Positions	21
7. Instrumentation Block Diagram for Velocity Survey Measurement	23
8. Instrumentation Block Diagram for Acoustic Pressure and Unsteady Lift Measurements	25
9. Dynamic Lift Gage Response from the Envelope of the Broadband Spectral Output	27
10. Spectrum of Microphone Output from Pistonphone Signal . . .	28
11. Typical Velocity Profiles for 8-, 9-, and 10-Cycle Distortion Screens at Rotor Midspan	31
12. Typical Harmonic Level Plots for 8-, 9-, and 10-Cycle Distortion Screens at Rotor Midspan	32
13. Flow Orientation and Reference for Phase Angle Measurement	34
14. 0-Cycle Distortion Screen Velocity Profiles for Constant V_x at Three Radial Locations	38
15. Typical Broadband Levels versus Rotor Speed for the AFRF	42
16. Spectral Comparison of Microphone Outputs Above the Cut-Off Frequency for the (1,0) Mode	43
17. Spectral Comparison of Lift Gage Outputs Above the Cut-Off Frequency for the (1,0) Mode	45

LIST OF FIGURES (continued)

<u>Figure</u>	<u>Page</u>
18. The Effect of Changing Temperature on the AFRF (1,0) Mode Cut-Off Frequency	50
19. Acoustic Pressure Pattern for the Second Overtone (Fifth Harmonic) Standing Wave in the AFRF	54
20. Temperature versus the AFRF (1,0) Mode Cut-Off Frequency and the Second Overtone Standing Wave Frequencies for the (0,0) and (1,0) Modes	57
21. Fourier Harmonics of 8-Cycle Screen versus Mean Axial Flow Velocity for Current Work	60
22. Fourier Harmonics of 9-Cycle Screen versus Mean Axial Flow Velocity for Current Work	61
23. Fourier Harmonics of 10-Cycle Screen versus Mean Axial Flow Velocity for Current Work	62
24. SPL versus Microphone Position with the 8-, 9-, and 10-Cycle Screens Installed in the Duct Below and Above the (1,0) Mode Cut-Off Frequency	65
25. Fourier Harmonic Amplitudes of the 8-Cycle Screen	67
26. Fourier Harmonic Amplitudes of the 9-Cycle Screen	68
27. Fourier Harmonic Amplitudes of the 10-Cycle Screen	69
28. Modal Pressure Decay Rate for the AFRF	71
29. Typical Spectrum of Lift Gage Output	73
30. Typical Fourier Harmonic Analysis of Lift Gage Output	74
31. Unsteady Lift Coefficient versus (1,0) Mode Cut-Off Ratio for 8-Cycle Screen Measurement for Current Work	75
32. Unsteady Lift Coefficient versus (1,0) Mode Cut-Off Ratio for 9-Cycle Screen Measurement	76
33. Unsteady Lift Coefficient versus (1,0) Mode Cut-Off Ratio for 10-Cycle Screen Measurement	77
34. Unsteady Lift versus (1,0) Mode Cut-Off Ratio for 10-Cycle Screen Measurement	79

LIST OF FIGURES (continued)

<u>Figure</u>	<u>Page</u>
35. Typical Spectrum of Microphone Output	83
36. Typical Fourier Harmonic Analysis of Microphone Output . .	84
37. SPL Magnitude and Phase Angle Measurement versus (1,0) Mode Cut-Off Ratio for 8-Cycle Screen Measurement	85
38. SPL Magnitude and Phase Angle Measurement versus (1,0) Mode Cut-Off Ratio for 9-Cycle Screen Measurement	86
39. SPL Magnitude and Phase Angle Measurement versus (1,0) Mode Cut-Off Ratio for 10-Cycle Screen Measurement	87
40. Predicted and Measured (0,0) Mode Steady State Waveform	89
41. Predicted and Measured (1,0) Mode Steady State Waveform	90
42. Measured SPL Waveforms at the (0,0) Mode Second Overtone Standing Wave Frequency	92
43. SPL of (0,0) Mode versus (1,0) Mode Cut-Off Ratio from 9-Cycle Screen Measurement	93
44. SPL of (1,0) Mode versus (1,0) Mode Cut-Off Ratio from 8- and 10-Cycle Screen Measurement	94
A1. Theoretical and Designed Resistance Coefficient Variation for the 8-Cycle Distortion Screen	106
A2. The 8-Cycle Distortion Screen	107
A3. Theoretical and Designed Resistance Coefficient Variation for the 9-Cycle Distortion Screen	108
A4. Theoretical and Designed Resistance Coefficient Variation for the 10-Cycle Distortion Screen	109
B1. Instrumentation Setup for Static Calibration of the Lift Gage	111
B2. Setup for Dynamic Lift Gage Calibration Using a Small Shaker	112

LIST OF FIGURES (continued)

<u>Figure</u>	<u>Page</u>
B3. Instrumentation Setup for Dynamic Lift Gage Calibration Using a Large Shaker	114
B4. Dynamic Response of the Lift Gage from the Large Shaker Calibration Technique	116
C1. Flow Coefficient versus Mean Flow Incidence Angle	118
C2. SPL versus Flow Coefficient	120
C3. Unsteady Lift versus Flow Coefficient	121
D1. Comparison of Spectrum to Harmonic SPL Data	
(a) 8-Cycle Screen Data	125
(b) 9-Cycle Screen Data	126
(c) 10-Cycle Screen Data	127
D2. Comparison of Spectrum to Harmonic Unsteady Lift Data	
(a) 8-Cycle Screen Data	128
(b) 9-Cycle Screen Data	129
(c) 10-Cycle Screen Data	130

LIST OF TABLES

<u>Table</u>	<u>Page</u>
I. Geometrical Parameters of Nine-Bladed Cambered Rotor	19
II. Test Matrix of Unsteady Lift and Acoustic Pressure Parameters	36

LIST OF SYMBOLS

<u>Symbol</u>	<u>Description</u>
A	amplitude of Fourier harmonic
a	duct inner wall radius
a_{mn}	wavenumber coefficient
B	number of rotor blades
C	chord length
\tilde{C}_L	unsteady lift coefficient
C_{mn}	normalization constant of radial modal distribution
c	speed of sound
D	diffusion factor
E_{mn}	radial pressure distribution function of (m,n) mode
e	duct length end correction factor
f	frequency
f^*	cut-off frequency
$f_{SW(0,0)}$	standing wave frequency for (0,0) mode in the duct
$f_{SW(1,0)}$	standing wave frequency for (1,0) mode in the duct
i	flow incidence angle
J_m	Bessel function of the first kind of order m
K	flow resistance coefficient
k	wavenumber
k'	normalized wavenumber
ℓ	length of duct between rotor cascade and bellmouth inlet
\tilde{L}	unsteady lift force
M	Mach number

LIST OF SYMBOLS (continued)

<u>Symbol</u>	<u>Description</u>
m	circumferential mode order
n	radial mode order
P_s	static pressure
p	acoustic pressure
Q_{mn}	characteristic constant for (m,n) mode
r	radial coordinate
s	rotor blade opening
T	temperature
t	time
U	rotor blade rotational velocity
V	flow velocity
\bar{V}_x	mean axial flow velocity
W	relative velocity
x	axial distance coordinate
Y_m	Bessel function of the second kind of order m
α	helix angle
β	relative flow angle
γ	cut-off ratio
λ	wavelength
$\lambda_{SW(0,0)}$	standing wave wavelength for (0,0) mode in the duct
$\lambda_{SW(1,0)}$	standing wave wavelength for (1,0) mode in the duct
θ	circumferential coordinate
ρ	air density
σ	hub-to-tip radius ratio

LIST OF SYMBOLS (continued)

<u>Symbol</u>	<u>Description</u>
---------------	--------------------

ϕ	flow coefficient
ω	rotor angular velocity

Subscripts

a	rotor tip radius
b	rotor hub radius
e	rotor exit
f	fundamental
i	rotor inlet
m	mean radius
mn	modal order (m = circumferential, n = radial)
s	static
x	axial direction
(0,0)	associated with plane wave mode
(1,0)	associated with (1,0) mode

ACKNOWLEDGMENTS

This investigation was conducted under the sponsorship of the Naval Sea Systems Command through the Applied Research Laboratory of The Pennsylvania State University (ARL/PSU) as an Exploratory and Foundation (E&F) research project.

With sincere appreciation, the author acknowledges the guidance and support of his advisors, Drs. F. S. Archibald and R. E. Henderson. The helpful suggestions and assistance of Dr. D. E. Thompson are also greatly appreciated. Special recognition must be given to Messrs. W. L. Nuss, S. E. Alvarez, and G. B. Gurney for their aid with electronic problems as they arose during operation of the facility, and to Mr. G. D. Henderson for his computer programming help. The frequent mechanical assistance of Mr. C. E. Gearhart and Mr. J. E. Gilbert, along with the rest of the Garfield Thomas Water Tunnel crew, was also greatly appreciated.

The author wishes to acknowledge the assistance of Messrs. D. Schweinitz, R. C. Marboe, and D. J. Azevedo in data acquisition and analysis. Appreciation also is expressed to Dr. G. C. Lauchle for reading and reviewing this manuscript as a thesis committee member and to Mr. C. S. Lee for advice in operational techniques.

CHAPTER I

INTRODUCTION

1.1 The Basis of Compressor Noise Investigation

The high level of noise generated by turbomachines, such as jet engines, has caused great concern, especially in residential areas. Researchers in the aircraft industry have spent much time and effort to reduce jet engine noise because of its annoying and deleterious effects on people and structures. In their efforts to control jet engine noise, researchers began working on reducing exhaust noise generated during the takeoff process. Substantial reductions in noise levels were achieved; however, the reduction of exhaust noise made the compressor inlet noise generated during landing approach more obvious and, thus, the aircraft engine noise problem had not been totally solved. As a matter of fact, since the exhaust noise is generally broadband in nature and the compressor noise is composed of broadband noise and discrete frequency tones (which occur in the frequency range of maximum auditory response), reduction of the broadband noise levels resulted in more objectionable noise problems than previously existed due to the loud (above the threshold of pain) discrete frequency tones. Therefore, a major and important area of jet engine noise research is compressor inlet noise.

In the process of any noise reduction study, three main aspects of the noise must be studied. These are: (1) generation, (2) transmission, and (3) radiation. Once these aspects are thoroughly

understood, the noise reduction process can proceed with confidence. This investigation was designed to explain part of the noise generation process in a jet engine compressor or fan section and to answer some questions on the transmission characteristics of that noise. If these characteristics are better understood, the noise control engineer can propose effective noise reduction designs and substantial decreases will be achieved in jet engine noise. The three noise characteristics will now be discussed briefly as they are related to this study.

1.1.1 Generation

In general terms, the compressor inlet noise of a turbomachine is similar to fan noise since, in both cases, there is a rotor blade row spinning in a duct which generates flow. The turbojet engine has stationary stator blades in addition to a rotor, in order to control the swirl placed in the flow by the rotor. The interaction between the distorted flow leaving the stator blades and the flow leaving the rotor blades causes unsteady forces on the rotor blades which, in turn, cause acoustic pressure fields to travel downstream and upstream of the rotor blades. These acoustic pressure fields exist at the fundamental and harmonics of rotor blade passing frequency (BPF), which is the rotor shaft speed in rps multiplied by the number of rotor blades. These discrete tones are much higher in acoustic sound pressure level (SPL) than the turbomachine broadband noise level. When the wavelength associated with the unsteady force is much greater than the rotor blade chord, the force on each blade approximates a compact acoustical dipole. This is analogous to a pair of pulsating point sources which

which are 180° out of phase with each other, equal in magnitude and separated by a distance which is small compared to the acoustic wavelength. The dipole generates a fluctuating force principally along a line connecting the two sources. This force, in this case of the turbomachine blading, corresponds to the unsteady lift vector.

1.1.2 Transmission

The transmission of an acoustic pressure wave in an annular duct can be described in terms of an infinite series of acoustic modes. This infinite series is a solution to the wave equation in cylindrical coordinates with the boundary conditions applied at the duct walls. The acoustic modes correspond to zeroes of Bessel functions and their derivatives whose arguments are frequency dependent. Except for the plane wave mode, these modes have the property that, below a critical frequency, the modes decay exponentially along the duct in the axial direction and, above this frequency, the modes propagate unattenuated through the duct. The frequency at which this transition from decay to propagation along the duct occurs is termed the cut-off frequency and will be denoted by f^* . Therefore, there exists a definite set of eigenfrequencies, which are dependent upon the duct geometry, at which modes begin propagating in the annular duct. The mathematical evaluation of the above will be given in Chapter III.

The duct acoustic modes are labeled according to the number of nodal (or zero pressure) lines that exist circumferentially, m , and radially, n , where m and n can be zero or positive integers. All modes having no circumferential nodal lines, or for $m = 0$, consist of pressure wavefronts travelling purely axially along the duct. Modes of

one or more circumferential nodal lines, or for $m = 1, 2, \dots$, consist of pressure wavefronts which spin along the duct at a specific helical angle, α , which is dependent upon rotor speed. Thus, the lowest order mode is the (0,0) mode, otherwise known as the plane wave mode. This mode has a uniform distribution of acoustic pressure over the entire duct cross section and a cut-off frequency of 0 Hz, so the plane wave propagates along the duct at the free field speed of sound for all rotor speeds. Each subsequent higher order mode has a higher cut-off frequency dependent on the duct geometry and has supersonic phase speed for BPF's greater than f^* . In the usual annular geometry case, the higher order modes have local pressure maxima at the duct walls. Figure 1 shows the general transmission characteristics of the acoustic duct modes. The solid lines in Figure 1 represent peaks of sound pressure. The pitch of the helix in the middle diagram is frequency dependent. As the BPF is decreased towards the cut-off value, the axial wavelength increases and the helical pitch increases until the limiting value of the cut-off condition where the wavefronts spin at right angles to the duct axis.

In this study, the plane wave (0,0) mode and the first higher order (1,0) mode with no radial nodal lines are investigated. Due to the spinning nature of the higher order modes, the same mode can be generated to spin in the same circumferential direction as the rotor rotation (co-rotational), designated as the (+1,0) mode, and to spin in the opposite circumferential direction as the rotor rotation (counter-rotational), designated as the (-1,0) mode. Thus, positive and negative signs denote modal rotational direction with respect to that of the rotor. An investigation of this mode for the (1,0) and

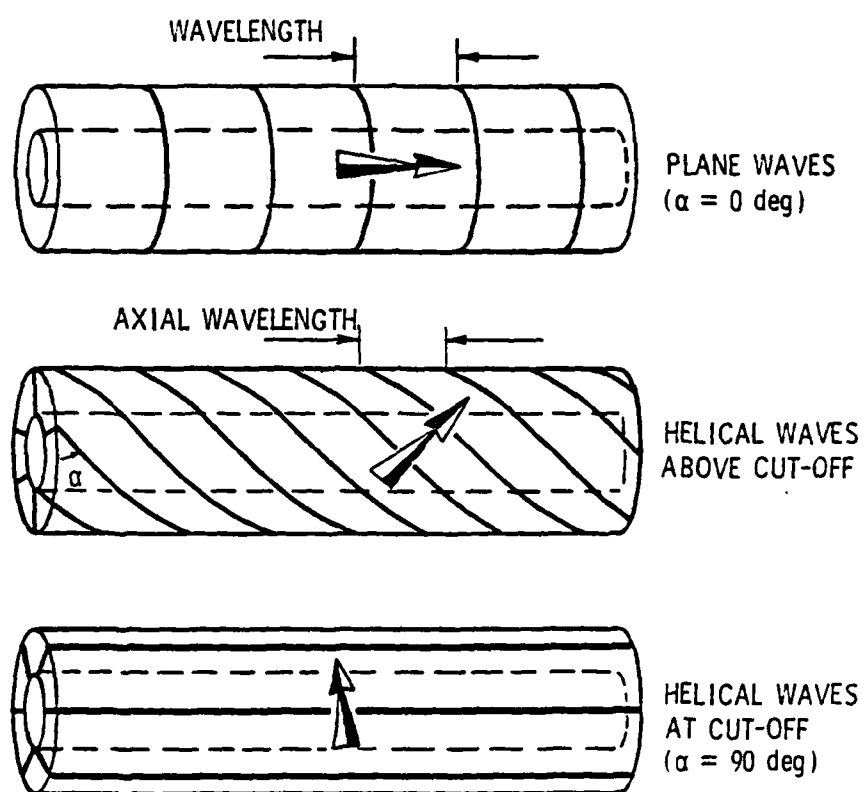


Figure 1. Transmission Characteristics of Acoustic Duct Modes

(-1,0) cases was thus included in this study for a thorough observation of the modal characteristics in the duct.

Since the plane wave always propagates axially along the duct, an investigation of the first higher order mode must, in addition, involve an investigation of the plane wave mode below the (1,0) mode cut-off BPF and a combination of the (0,0) and (1,0) modes above the (1,0) cut-off BPF. Since higher order modes are cut on at successively higher BPF's, investigations of them would include contributions from all lower order modes. Thus, experimentally for optimum modal isolation, the lowest order modes should be observed.

1.1.3 Radiation

The directivity patterns from the duct inlet are dependent upon the modes propagating along the duct. The plane wave has a pressure maximum along the duct axis, while the (1,0) mode above cut-off has pressure cancellations along the duct centerline. Directivity studies were not stressed in this investigation and only in-duct observations were necessary for the purposes of this study.

1.2 Previous Theoretical and Experimental Relevant Work

Theoretical and experimental work on compressor noise has primarily been concerned with two domains--unsteady aerodynamic lift force, and acoustic pressure generation. Figure 2 represents the rotor-stator flow interaction for a cascade of airfoils. The stator blades, while introducing a swirl into the inlet flow, introduce velocity deficiencies due to the boundary layers on the blades which cause a change in the magnitude and direction of the flow velocity incident on the rotor blades with time. This velocity variation

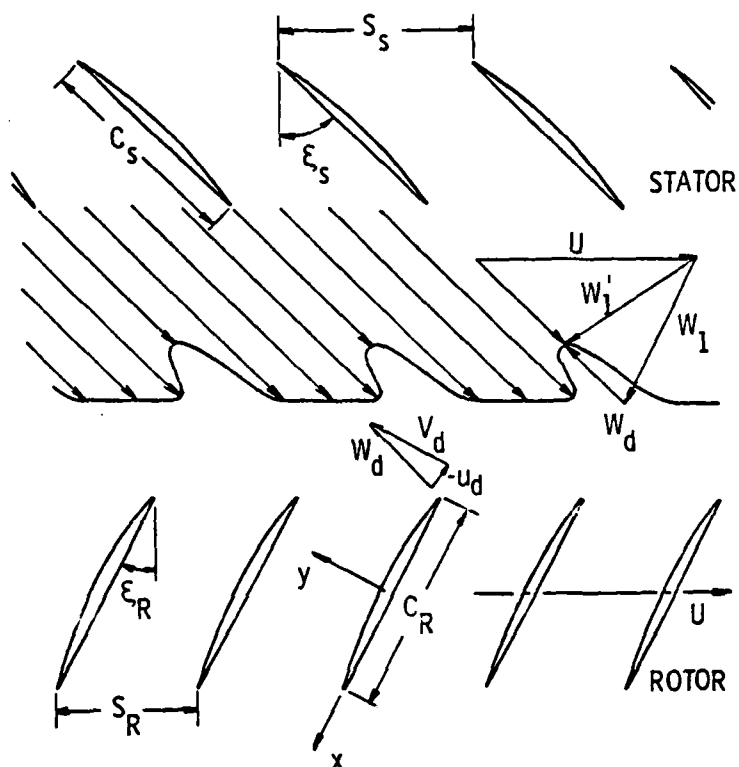


Figure 2. Rotor-Stator Flow Interaction for Cascades of Airfoils

generates unsteady lift forces on the rotor blades. Kemp and Sears [1]* calculated the unsteady lift force on rotor and stator blades in turbomachines using isolated thin airfoil theory for nonuniform motion. This model considered zero-degree flow incidence only, neglected the effects of cascade spacing, and considered only the flow disturbances normal to the blade chord. Horlock [2] extended this theory to analyze the unsteady lift on an isolated flat airfoil subjected to low disturbances having parallel and normal components to the blade chord. Whitehead [3, 4] introduced the effects of cascade spacing and included the effect of nonuniform inflow. Specifically, Whitehead's model consisted of an infinite, two-dimensional cascade of flat blades in inviscid, incompressible flow at zero mean incidence. Henderson and Daneshyar [5] took the analysis one step further by including the effects of blade camber and incidence angle on the unsteady lift forces. Smith [6] performed an analysis to yield the same results as Whitehead, but also extended this work to include a closed-form solution for the unsteady lift and the acoustic pressure generated by compressor rotor-wake interaction. Smith extended Whitehead's analysis to take into account five additional inputs to the situation (gust vorticity, torsional oscillations and heaving of the blade, and upstream and downstream acoustic waves impinging on the blades) and five corresponding outputs from them (downstream shed vorticity, torsional and lift coefficients, and upstream and downstream wavefronts from reflections). Sound generation by rotor-stator interaction was also analyzed by Kaji and Okazaki [7], who modeled a flat-plate cascade

*Numbers in brackets [] indicate References, see page 101.

by an array of acoustic dipoles. They found the ratio of the number of blades in the rotor to the number of stator blades greatly affects the sound pressure generated due to the change caused in the sound wave propagation angle. Mani [8] used linearized equations and assumed the blade chord and spacing to be small compared with the sound wavelength to analyze discrete frequency noise generation in an axial flow fan. Linearized potential flow equations were used by Osborne [9] to approximate unsteady motion of a two-dimensional thin airfoil in a compressible subsonic flow. These linearized theories were restricted to low Mach numbers and low reduced frequencies.

Acoustic generation and transmission of axial flow compressor noise was described in a classic paper by Tyler and Sofrin [10]. They described the duct acoustics of the situation and demonstrated how a rotor with a subsonic tip speed interacting with wakes from a stator can generate a rotating pressure pattern with a supersonic phase speed which can excite spinning acoustic modes in the duct. Morfey [11] described acoustic duct mode generation and transmission in greater detail than Tyler and Sofrin, discussing sound transmission in infinite as well as finite ducts. Finite duct analysis involves introducing boundary conditions and reflections in the duct, which can be applied to the wave equation solution in cylindrical coordinates.

Experimental effort has concentrated either on measuring the unsteady lift force on blades in cascades or on measuring acoustic duct pressure. Bruce [12] has measured the unsteady lift response of a rotor blade to a known inflow distortion. His measurements were performed with a strain gage blade segment at the midspan section of a rotor blade. Satyanarayana et al. [13] performed unsteady lift

measurements using miniature pressure transducers mounted around a blade of a stationary cascade. The measurements taken were found to be in good agreement with the analysis of Reference [5]. It also demonstrated the significance of contributions from neighboring cascade blades, thus invalidating isolated airfoil theory for these cases. Gallus et al. [14] also used miniature pressure transducers, but mounted them on both a rotor and a stator blade on both pressure and suction surface sides. Differences that currently exist between experimental results and theory can be accounted for by the restrictions introduced by the idealized conditions of the theories.

Noise measurements from fans and turbojet compressors have been performed by several people. Sharland [15] explained various broadband and discrete noise sources in axial flow fans. He described how rotor-stator aerodynamic interaction generated discrete frequency noise and how vortex shedding at blade trailing edges and flow turbulence generated broadband noise. He also describes how discrete frequency noise is strongly dependent upon axial spacing between blade rows. Bragg and Bridge [16] reported from deliberations of a panel of academic experts on compressor noise. They found that the noise was dipole in origin and came mainly from the first two compressor stages of the turbojet engine, in addition to previously documented findings. A more comprehensive compressor noise study was carried out by Lowson [17], in which a direct unsteady lift force—acoustic duct pressure relationship is suggested. Benzakein [18] discussed the phenomenon of multiple pure tone generation in high-speed fans. These subharmonic tones can be of comparable, if not higher, levels than the blade

passing frequency tones for high-tip-speed compressors and thus cannot be ignored in compressor noise studies.

Lipstein and Mani [19] set up two different arrays of rods upstream of a compressor rotor to generate acoustic modes normal and parallel to the blade force to investigate discrete frequency noise generated by unsteady blade forces. They obtained good agreement with the theory of References [1] and [8]. Harel and Perulli [20] used a six-bladed rotor with low axial flow speed and measured the discrete frequency noise generated. They obtained agreement with duct mode models theorized in Reference [10]. Moore [21] determined the acoustic source distribution by processing microphone signals obtained over a plane perpendicular to the duct axis. In this manner, radial and circumferential duct modes were observed. Similar measurements were taken by Smith [6] in a high hub-to-tip ratio compressor rotor running in a parallel-walled annular duct. He measured inflow distortions generated by screens and, after accounting for reflections from the duct inlet, obtained good agreement with his theory.

The phenomenon of an acoustic pressure field influencing an essentially incompressible fluid dynamic field has been termed back-reaction [22]. This suggests the possibility of the acoustic duct pressure, at high levels, altering the unsteady lift forces on rotor blades in a jet engine compressor. Lee [23] suggested this phenomenon as a reason for unexplainable trends in his data when attempting to correlate unsteady lift and acoustic pressure measurements. Archibald [24, 25] showed that high intensity acoustic fields, such as those which exist at acoustic resonance, could control vortex shedding and laminar boundary layer instability. Also, Crow and Champagne [26]

found that, for a low Mach number jet, an acoustic field could produce a more orderly structure in the flow.

On the basic subject of aerodynamic and turbomachinery noise, Morfey [27] and Cumpsty [28] have written brief, but thorough, critical reviews. Most recently, Lee [23] simultaneously monitored unsteady lift forces on a rotor blade and acoustic duct pressure in an attempt to find a coupling factor between the two. Due to anomalies he attributed to back-reaction around the cut-off frequency for the first higher order spinning duct mode, he could not conclusively determine that coupling factor.

1.3 Object of This Work

As discussed above, a substantial number of experimental studies have been conducted of the unsteady lift forces on rotor blades and the acoustic pressure patterns in compressor-type apparatus. However, the simultaneous measurement of the two physical phenomena has only been accomplished by Lee. While theoretical couplings of the unsteady lift to the acoustic pressure has been accomplished, it has not yet been verified experimentally. Lee's difficulties in obtaining precise experimental results revealed the necessity for a more extensive study of the situation. In Lee's investigation, the plane wave and first higher order spinning wave modes rotating in the direction opposite to the rotor, $(-1,0)$, were considered. In the present study, those modes plus the $(+1,0)$ mode will be generated and studied. This will increase the understanding of back-reaction effects around the cut-off frequency noted by Lee and establish a coupling factor (which has only been theorized before) between the unsteady lift and acoustic pressure.

CHAPTER II

EXPERIMENTAL ASPECTS

2.1 Introduction

In the experiment, BPF tone levels at different wall locations and unsteady lift (normal) force levels at the midspan of the rotor blade were measured for a range of rotor speeds, blade mean flow incidence angles, and reduced frequencies in a large, low-speed axial flow fan. The noise-producing mechanisms and the measurements conducted in the experiment are schematically presented in Figure 3.

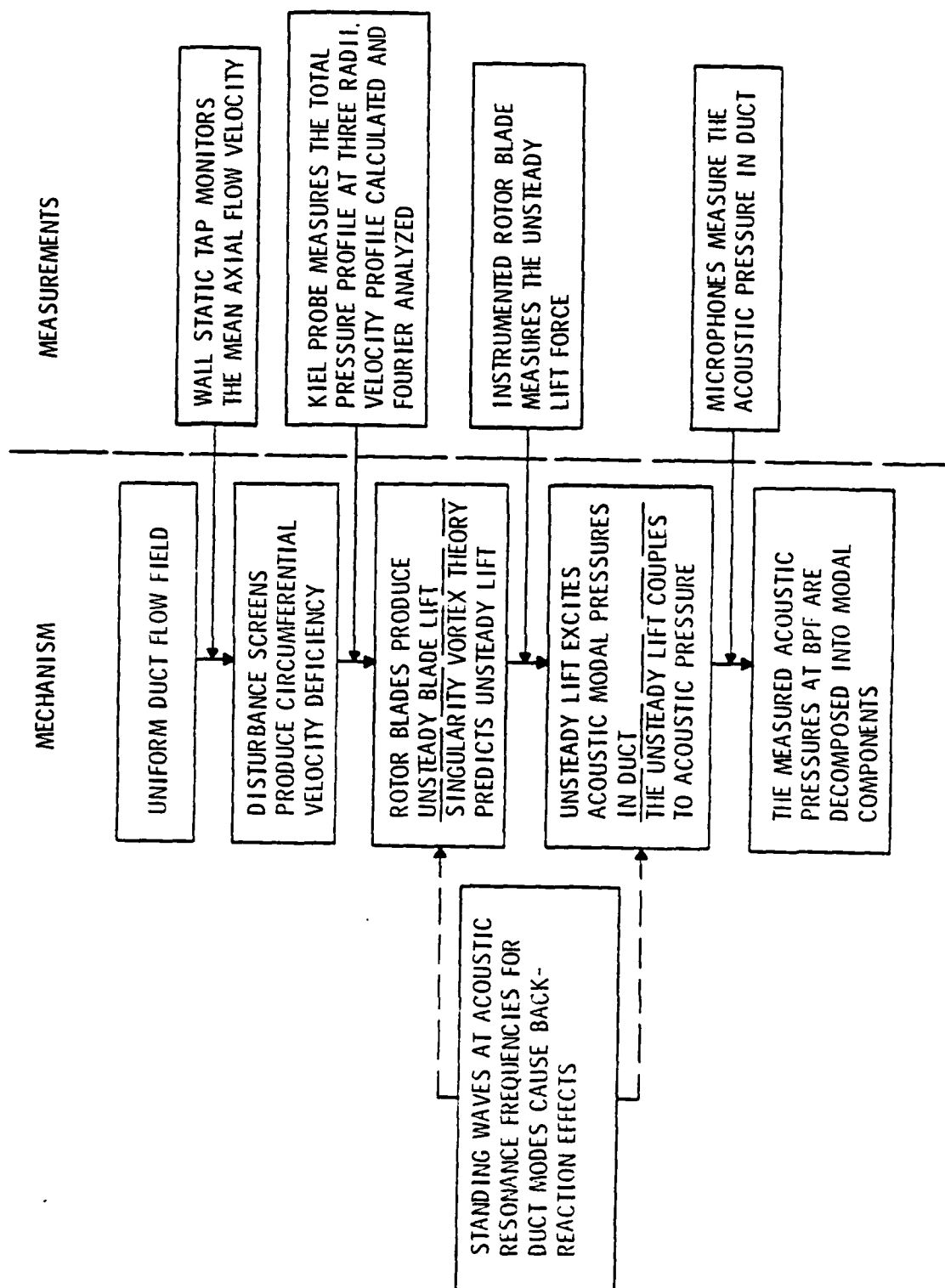
A circumferential sinusoidally varying flow field was generated by distortion screens. The interaction between the rotor and the distorted flow generated an unsteady lift force on each rotor blade which, in turn, excited acoustic duct modes which were transmitted through the duct. The levels of these modes could be seen as discrete BPF peaks which were well above the broadband level.

The unsteady lift force on a rotor blade was measured by a stainless steel strain gage sensor mounted inside a one-inch spanwise section at midspan of a blade. This instrumented rotor blade is shown in Figure 4.

The acoustic pressure in the duct was measured using a 0.318 cm (1/8 inch) Brüel and Kjaer (B&K) microphone. Holes were drilled at different locations in the wall of the duct so that a microphone could be flush-mounted on the duct inner wall. Four microphone positions were used for the main body of the experiment since four acoustic

Figure 3. Schematic Diagram of Noise Mechanisms and Experimental Measurements

14



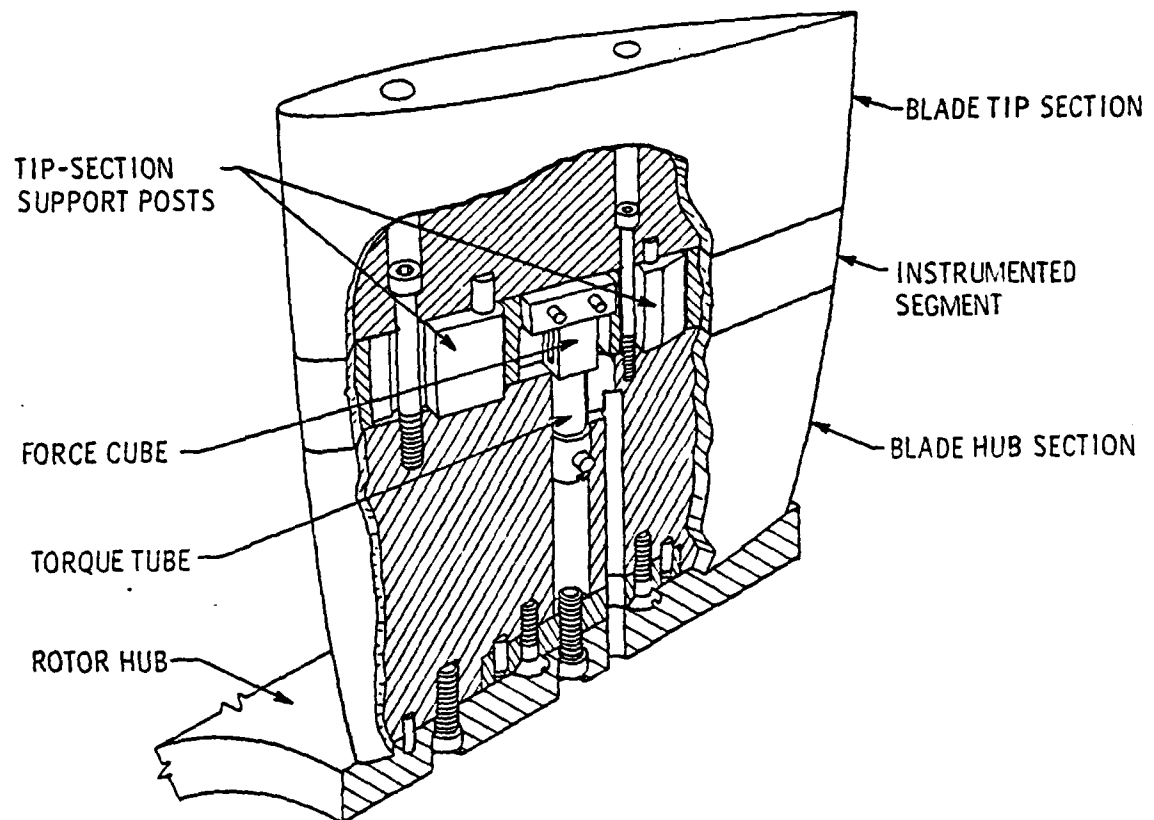


Figure 4. The Instrumented Rotor Blade

pressure measurements were needed for each rotor speed in order to decompose theoretically the pressure readings into duct mode waveforms. Three flow distortion screens generated predominantly three acoustic modes, as will be discussed in more detail later. With each duct mode predominating, the coupling between the acoustic pressure in the duct and the unsteady lift force on the rotor blades can be investigated.

2.2 Apparatus

The experiment was performed in the Garfield Thomas Water Tunnel Building at The Pennsylvania State University. The facility employed is the Axial Flow Research Fan (AFRF) which is pictured in Figure 5 and described in detail by Bruce [29]. Not shown in Figure 5 is an anechoic chamber, described by Fitzgerald and Marboe [30], which was built around the bellmouth inlet for the purpose of directivity studies from the fan. The auxiliary fan in the downstream end of the AFRF draws air through the bellmouth inlet to generate a nearly uniform flow through the duct inlet before the flow encounters a distortion screen. This simulates an air flow similar to that encountered by a turbojet engine in flight. The auxiliary fan is driven by a 52,200 watt motor and has a maximum intake rate of $2550 \text{ m}^3/\text{s}$ of air at a pressure of 872 N/m^2 .

The test rotor is driven by a separate 15,000 watt motor. This enables separate adjustment of rotor and flow speeds for operation at different blade mean flow incidence angles. The rotor consists of nine cambered blades, each having a chord length and span of six inches. It has a hub-to-tip radius ratio of 0.443. The blade profile has a circular arc camberline and a 10% maximum thickness-to-chord ratio. Table I presents the geometric parameters of the rotor blades and Lee described the details of the rotor design.

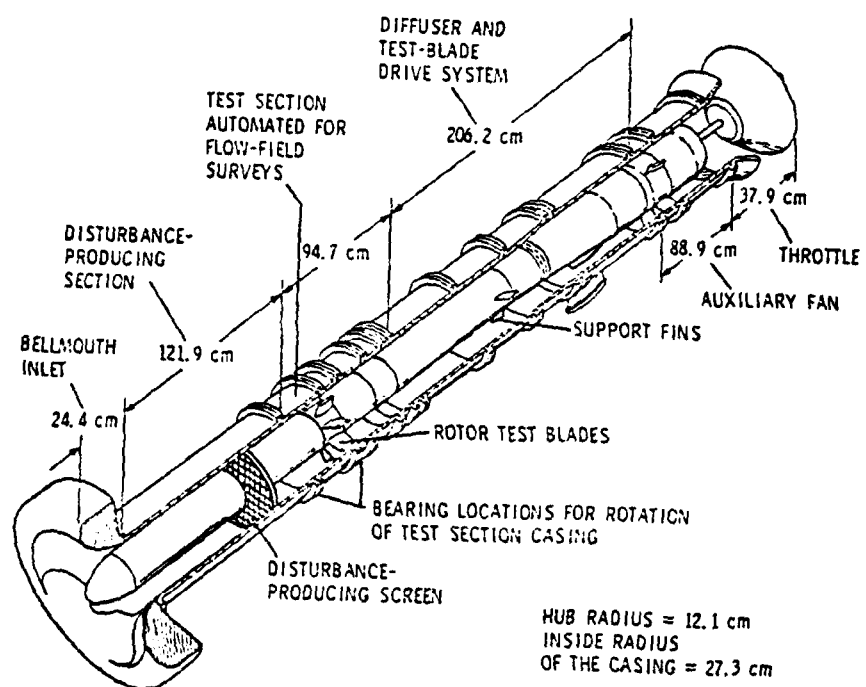


Figure 5. The Axial Flow Research Fan (AFRF)

TABLE I
GEOMETRICAL PARAMETERS OF NINE-BLADED CAMBERED ROTOR

Radius (meters)	Chord (meters)	Space-to- Chord Ratio	Maximum Camber (meters)	Camber Angle (deg)	Stagger Angle (deg)	Inlet Flow Angle (deg)	Outlet Flow Angle (deg)
0.121	0.1524	0.5526	0.004481	35.64	23.14	40.96	5.27
0.136	0.1524	0.6225	0.002225	28.12	31.02	45.58	16.90
0.166	0.1524	0.7621	0.000579	17.87	42.44	51.38	33.55
0.197	0.1524	0.9018	0.000168	11.74	50.28	56.14	44.39
0.227	0.1524	1.0414	0.000051	8.01	55.78	59.63	51.77
0.258	0.1524	1.1810	0.000018	5.71	59.85	62.71	57.04
0.273	0.1524	1.2508	0.000010	4.80	61.59	63.99	59.19

Lee also described how he selected the four microphone measurement positions to discriminate between modes after considering acoustic reflection effects from the rotor cascade and the duct inlet open end. In order to study the decay of sound pressure level (SPL) with distance from the rotor blades at different rotor speeds and constant mean incidence angles, in this investigation, nine additional holes were drilled at different axial locations along a straight line (at the same circumferential locations) upstream of the test rotor along the duct. The locations of the distortion screen, test rotor, and major microphone positions are shown in Figure 6. The procedure used to design the distortion screens is presented in Appendix A.

2.3 Instrumentation

2.3.1 Velocity Survey

A Kiel probe located in the plane of the rotor leading edge with the rotor removed was used to measure the local total pressure of the flow in the AFRF. The Kiel probe was positioned downstream of the flow distortion screen and attached to the outer duct wall. The duct section in which the probe was housed was rotated in two-degree increments by a Slo-Syn Type SS1800-1007 driving motor which was controlled by a Slo-Syn Indexer. A wall tap near the bellmouth inlet monitored the wall static pressure at that location as a means of determining the mean flow velocity in the duct. At each circumferential measurement location (at constant probe radius in the duct), the pressures from the Kiel probe and wall static tap were converted into DC voltages by two separate transducers. The voltages were then processed by a multi-channel integrating digital voltmeter with the

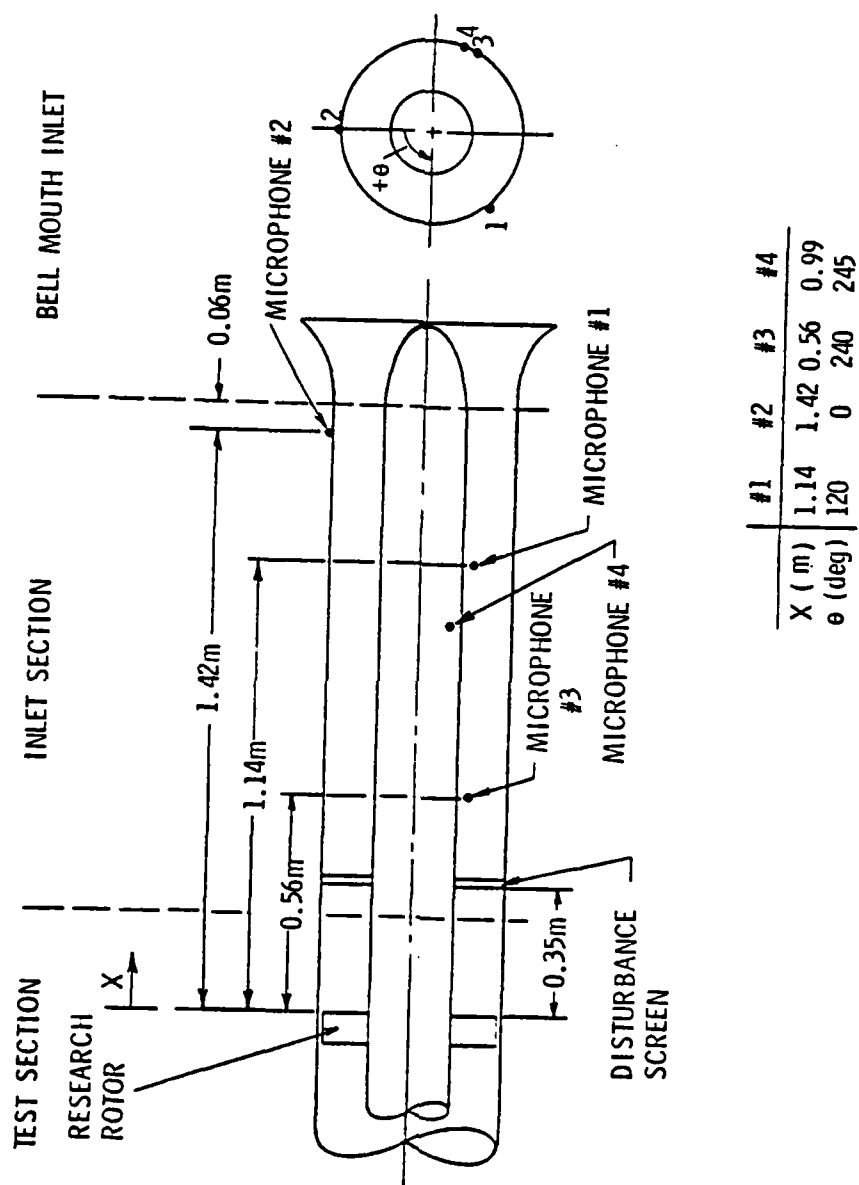


Figure 6. Relative Locations of Distortion Screen, Rotor Cascade, and Microphone Positions

output punched onto a paper tape. A barometer and digital thermometer measured the atmospheric pressure and the temperature, respectively, so the air density could be calculated. The paper tape along with the air density reading was then input to a computer for data reduction. The computed circumferentially varying velocity profiles were then Fourier analyzed and the magnitudes and phase angles of the first thirty harmonics were determined and plotted.

Figure 7 shows a block diagram of the instrumentation and data reduction described above.

2.3.2 Acoustic and Lift Measurements

An amplifier was used to boost the varying DC voltage signal from the strain gage in the instrumented rotor blade which was supplied with a constant four volts DC. The voltages to and from the strain gage passed through silver coil slip-rings in the hub of the fan. The position and speed of the rotor was determined using a photodiode. Light passing through a single slit in a disk on the rotor shaft was sensed by a photodiode, thus generating a once-per-revolution circumferential reference position pulse. Light passing through an inner row of 60 slits on the same disk was tracked by another photodiode which gave a direct reading of the shaft speed in rpm in a one-second time period. The unsteady pressure was measured by a B&K Type 4138 0.318 cm (1/8 inch) microphone connected to a B&K Type 2603 amplifier which supplied a constant DC voltage to the microphone. The flush-mounted microphone was moved systematically to each of the four microphone positions in the duct wall.

The output signals from the strain gage and microphone were fed into a Spectral Dynamics (SD) Corporation Model 360 dual channel Fourier

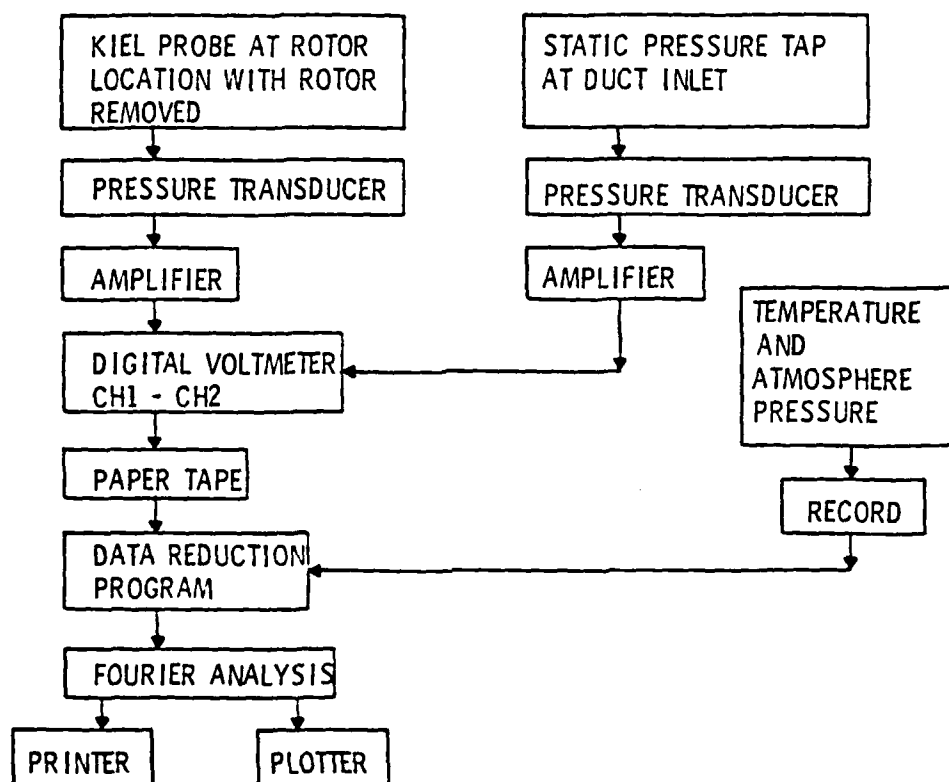


Figure 7. Instrumentation Block Diagram for Velocity Survey Measurement

processor. One function of this processor is a Fast Fourier Transform (FFT) analysis technique which can produce an ensemble-averaged spectrum for the incoming signal. Another function of the processor is phase-locked averaging with subsequent FFT analysis in the time domain which outputs harmonic levels and phase angles as a function of harmonic numbers. In order to perform time domain analysis of the signals, the SD 360 must be used in conjunction with a Spectral Dynamics Model 134A tracking ratio tuner and a once-per-revolution time reference pulse.

With the once-per-revolution signal, the tracking ratio tuner generates 1024 pulses for each complete rotor revolution which triggers the analyzer to take the input signal and completely fill the analyzer memory in each shaft revolution. The signals from each subsequent revolution are averaged with previous data which results in an ensemble average of the signal in the time domain. A schematic diagram of the unsteady measurement and signal processing used is shown in Figure 8. To check that the appropriate signals were being sent from the lift gage and microphone to the analyzer, an oscilloscope was periodically used to monitor the signals. A wall static pressure tap (which was connected to a pressure transducer and was, in turn, connected to a DC voltmeter) was positioned near the bellmouth inlet. This sensor monitored the wall static pressure in the duct and provided a means of setting the mean axial flow velocity to set the conditions for each test.

2.4 Calibration

2.4.1 Strain Gage Calibration

Lee conducted a static calibration of the same steel strain gage used in this experiment by applying different masses to the instrumented

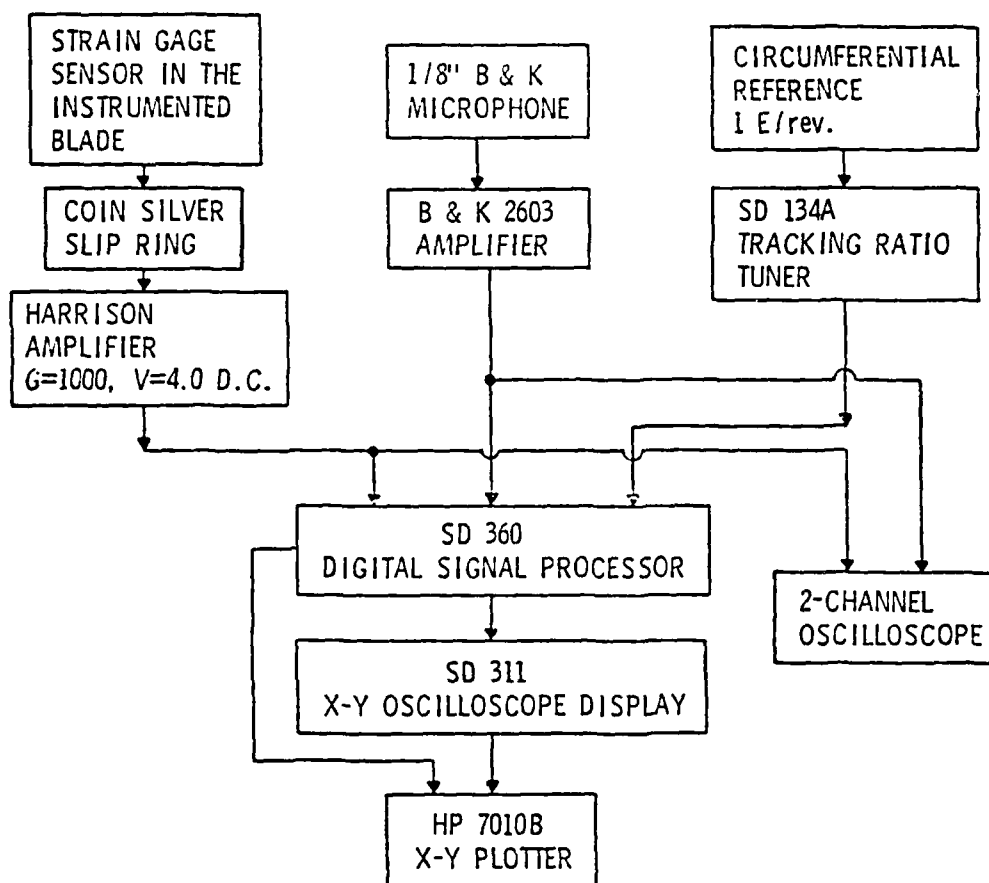


Figure 8. Instrumentation Block Diagram for Acoustic Pressure and Unsteady Lift Measurements

blade and observing the gage output. This resulted in a gage sensitivity of 4.32 N/volt for normal forces. A dynamic calibration was also necessary to determine the effect of frequency on the gage output. The dynamic response of the lift gage can be obtained from observation of the envelope of the broadband lift gage spectrum with no distortion screen in the duct, which is shown in Figure 9. Other more reliable methods which were used for determining the dynamic response of the gage are described in Appendix B. In all strain gage calibration cases, the gage was in place in the instrumented section of the rotor blade and the blade was rigidly supported at the hub end and free at the tip end. All methods of dynamic calibration used yielded a mechanical resonance peak at approximately 490 Hz, which is well above the maximum frequency of 350 Hz being observed in these studies. Since the gage response was shown to be relatively flat over the frequency range of interest to 350 Hz, the DC calibration constant can be applied with confidence to any of the analyzed frequencies.

2.4.2 Microphone Calibration

A B&K Type 4220 pistonphone provided a known acoustic source level of 124 dB (re 2×10^{-5} N/m²) at a known frequency of 246 Hz to calibrate the microphone. The spectrum of the microphone when excited by the pistonphone, Figure 10, shows a large peak at 246 Hz corresponding to the 124 dB tone. Because the B&K microphone has a flat frequency response over the frequency range of measurement, this single tone procedure is valid. Since the analyzer gives data in a dB scale, the peak level can be labeled as the reference level of 124 dB corresponding to a certain dB voltage level (with reference to

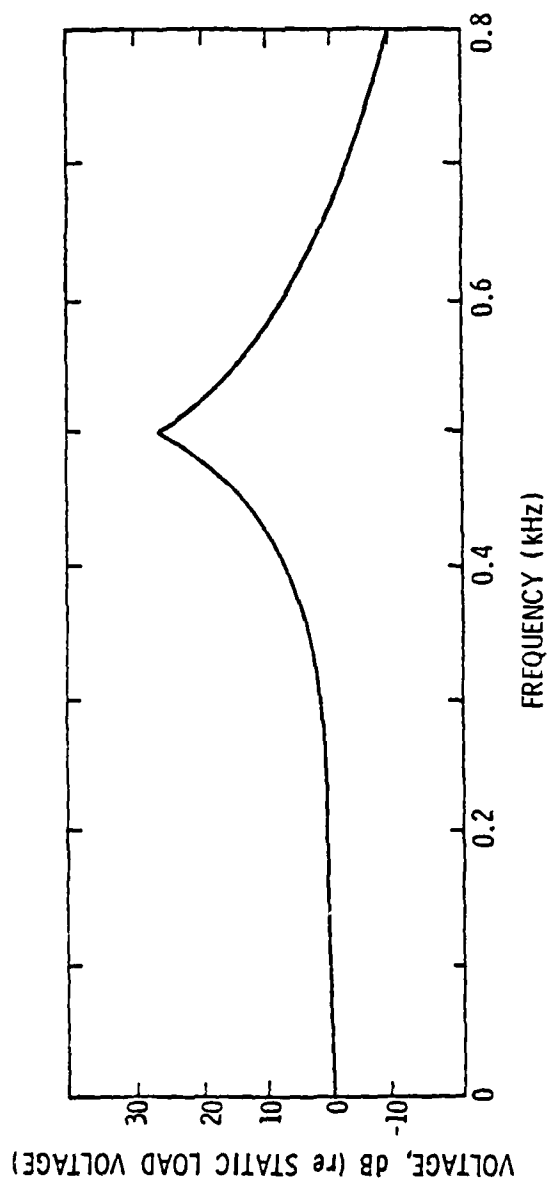


Figure 9. Dynamic Lift Gage Response from the
Envelope of the Broadband Spectral Output

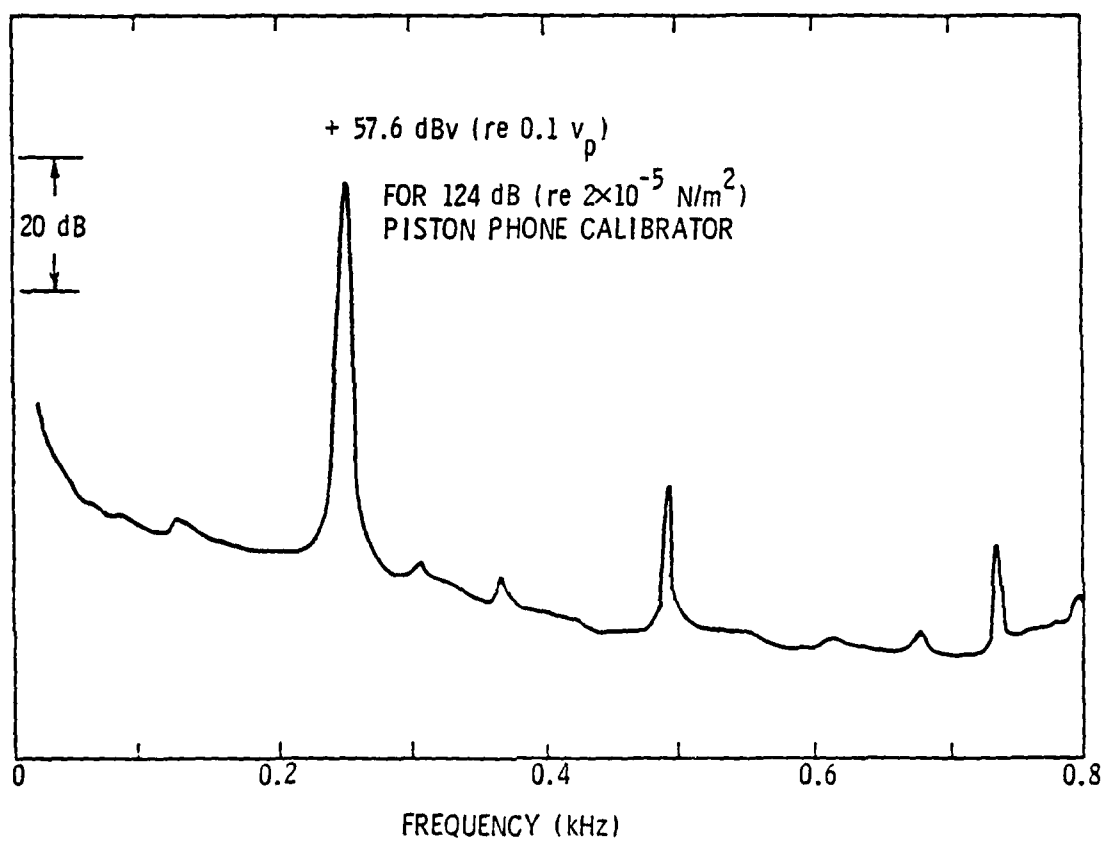


Figure 10. Spectrum of Microphone Output from Pistonphone Signal

0.1 volts peak). Other levels can be identified in terms of dB (re $2 \times 10^{-5} \text{ N/m}^2$) by simple addition of levels from the analyzer and accounting for attenuation levels of the B&K microphone amplifier and the SD 360 analyzer and bandwidth corrections.

2.4.3 Spectrum Analyzer Calibration

The SD 360 has its own internal calibration tone level of 0 dB, or 676 linear scale units, with reference to 0.0707 volts rms at approximately 25% of the frequency range being observed. The 0 dB reference had been set using this calibration tone each time the analyzer power switch was turned on.

2.4.4 Distortion Screens

The flow distortion screens were calibrated using flow velocity surveys. The flow measurements performed using the Kiel probe mentioned earlier were made at three radial positions in the duct--at midspan [$r = 0.197 \text{ m}$ (7.75 inches)], 2.54 cm from the rotor hub [$r = 0.146 \text{ cm}$ (5.75 inches)], and 2.54 cm from the duct wall [$r = 0.248 \text{ cm}$ (9.75 inches)]. The circumferential surveys were performed in two-degree increments by keeping the distortion screen spatially fixed and rotating a downstream portion of the outer casing which supported the probe. The rotor was removed for these tests to avoid contamination of the measurements. The mean axial velocity in the duct was set by the auxiliary fan which was powered by a Borg Warner 220 Volt Inverter with dial settings.

Bernoulli's equation for incompressible flow, given by

$$\Delta p = \frac{1}{2} \rho v^2 \quad ,$$

where Δp is the difference in pressure between that at the wall static tap and that from the Kiel probe in the flow, ρ is the air density, and V is the (axial) velocity of the flow, was solved for the velocity at each of the circumferential locations in the survey. Temperature and atmospheric pressure were recorded for each survey in order to calculate ρ . The paper tape output for each survey was fed into the computer, read, and analyzed. A Fourier analysis subroutine was also programmed to decompose the velocity profile into Fourier components. Sample plots of these results are shown in Figures 11 and 12.

The screens were designed to produce a circumferential sinusoidal variation of the flow with 8, 9, and 10 cycles over 360° . Figure 11 shows measured velocity variations for each screen at midspan. Figure 12 shows sample harmonic level plots. These plots show the approximations to the other main design feature of the screens. The level of the fundamental harmonic (the number of distortion cycles per 360°) of each screen was designed to be 20% of the circumferential mean velocity. A zero harmonic level is desired for all other harmonics, which would be the case for a purely sinusoidal distortion of N cycles in the flow, N being the fundamental harmonic number. Due to compromises in design and nonuniformities in the flow, 10% of the fundamental level would be an acceptable and expected ceiling level for harmonics other than the fundamental. Therefore, these two plots--the velocity profile, and the harmonic level plots--are essentially the calibration curves for the flow distortion screens. Lee had calibrated the 9- and 10-cycle screens previously, but the work was repeated here. The 8-cycle screen was designed specifically

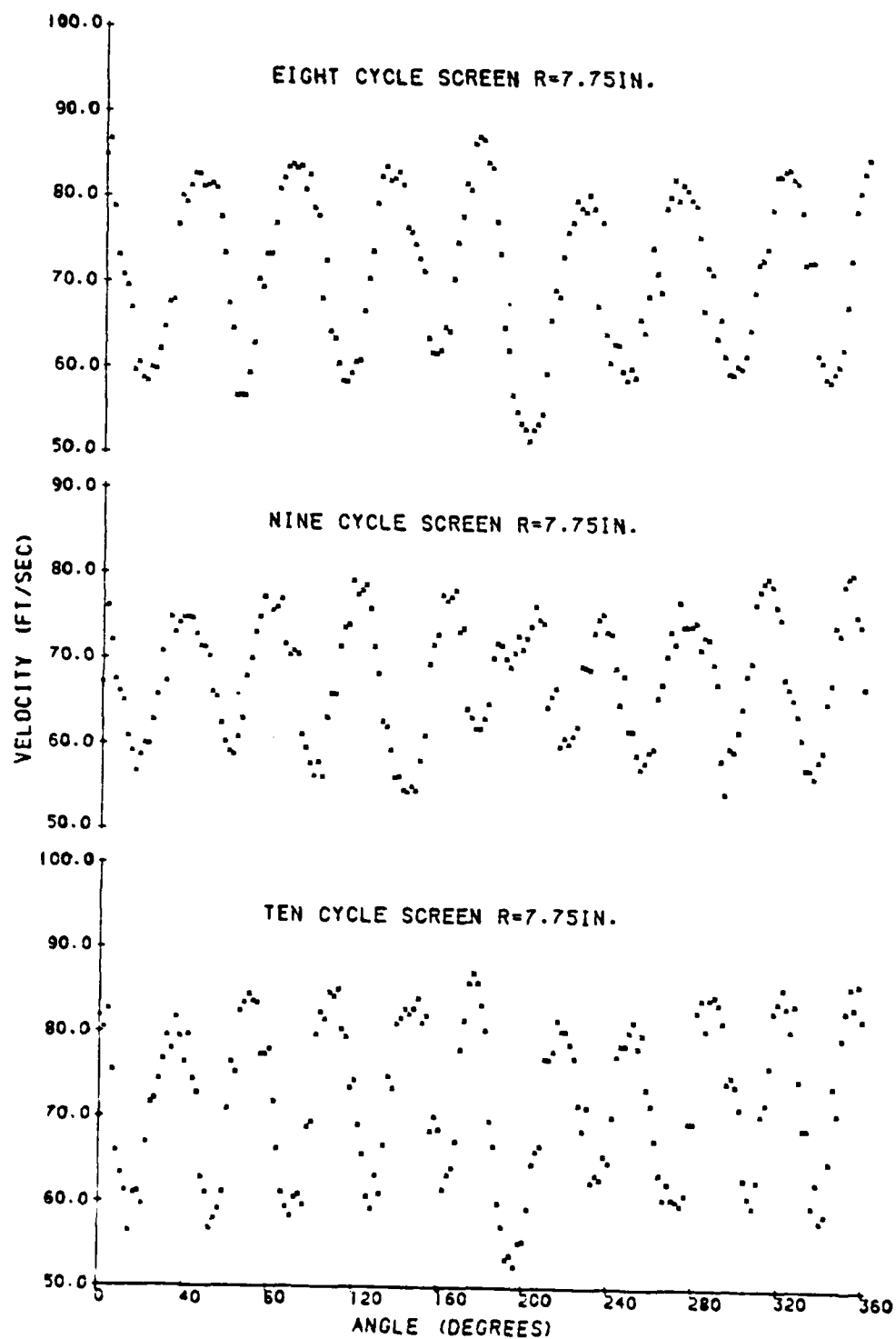


Figure 11. Typical Velocity Profiles for 8-, 9-, and 10-Cycle Distortion Screens at Rotor Midspan

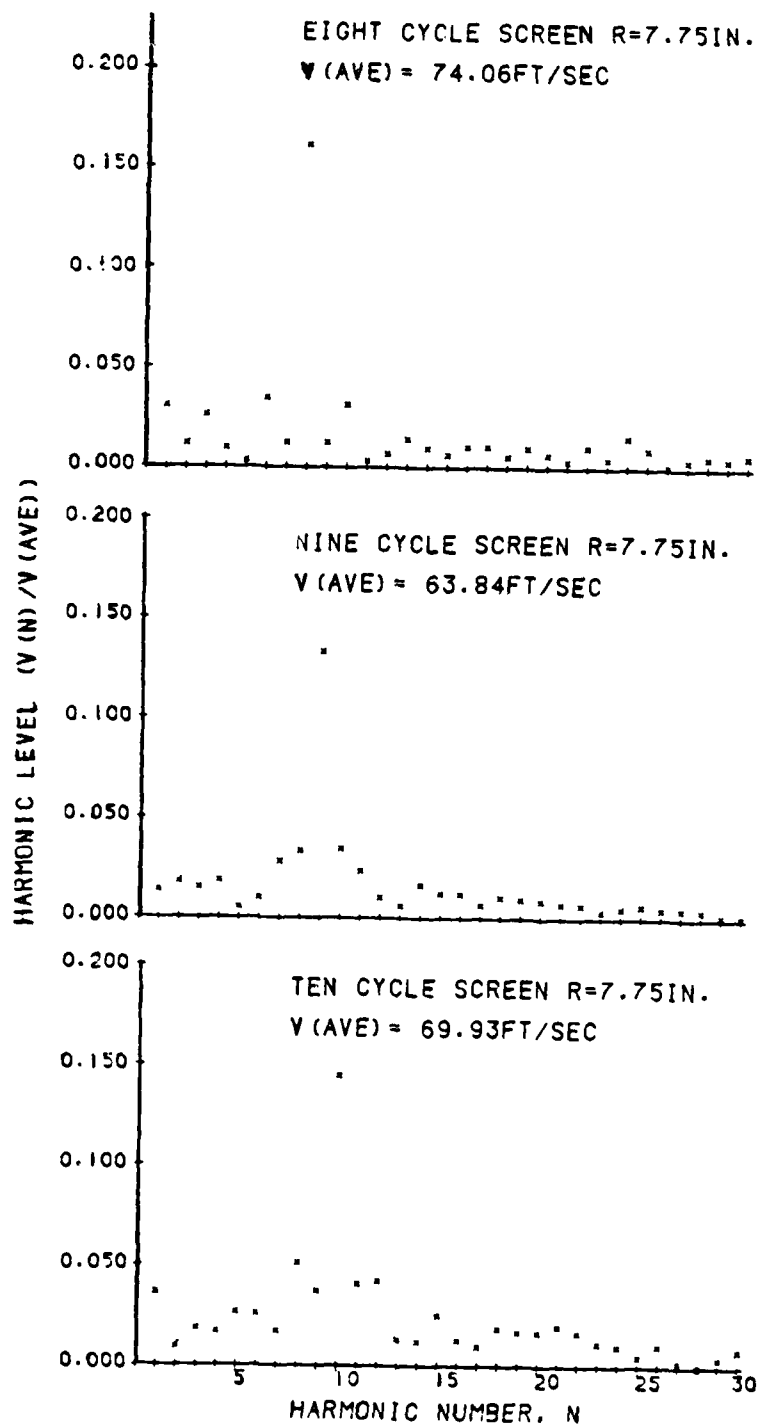


Figure 12. Typical Harmonic Level Plots for 8-, 9-, and 10-Cycle Distortion Screens at Rotor Midspan

for this study to investigate the (+1,0) mode, so more extensive calibration was performed on it than on the others.

2.5 Measurement

The velocity surveys served two purposes: (1) to calibrate the distortion screens, and (2) to set the conditions for the unsteady lift and acoustic measurements.

By monitoring the wall static pressures, P_s , near the bellmouth inlet during each survey, the mean axial velocity, \bar{V}_x , for each survey could be directly related to P_s at the duct open end. After all the surveys were completed, P_s was plotted versus \bar{V}_x for each screen. Therefore, \bar{V}_x could be set at a desired value by operating at a certain value of P_s .

In the unsteady pressure measurements, a constant mean blade incidence flow angle (i_m) was set for each rotor speed. In order to set this angle, a velocity vector diagram can be drawn as shown in Figure 13. Two sides of the triangle, \bar{V}_x and $r\omega$, where r is the rotor radius (chosen at midspan here since the strain gage is located at midspan) and ω is the angular speed of the rotor shaft, are vectorially combined to give W , the resultant velocity vector. The angle between W and the inlet blade angle of the rotor blades at midspan is i_m . Thus, if the rotor speed is varied, \bar{V}_x must be varied accordingly if the same i_m is desired. Since separate inverters ran the auxiliary fan motor and the rotor motor, the two could be adjusted independently to set the appropriate i_m for each rotor speed. Another method to designate the desired value of i_m is in terms of a flow coefficient, ϕ , where

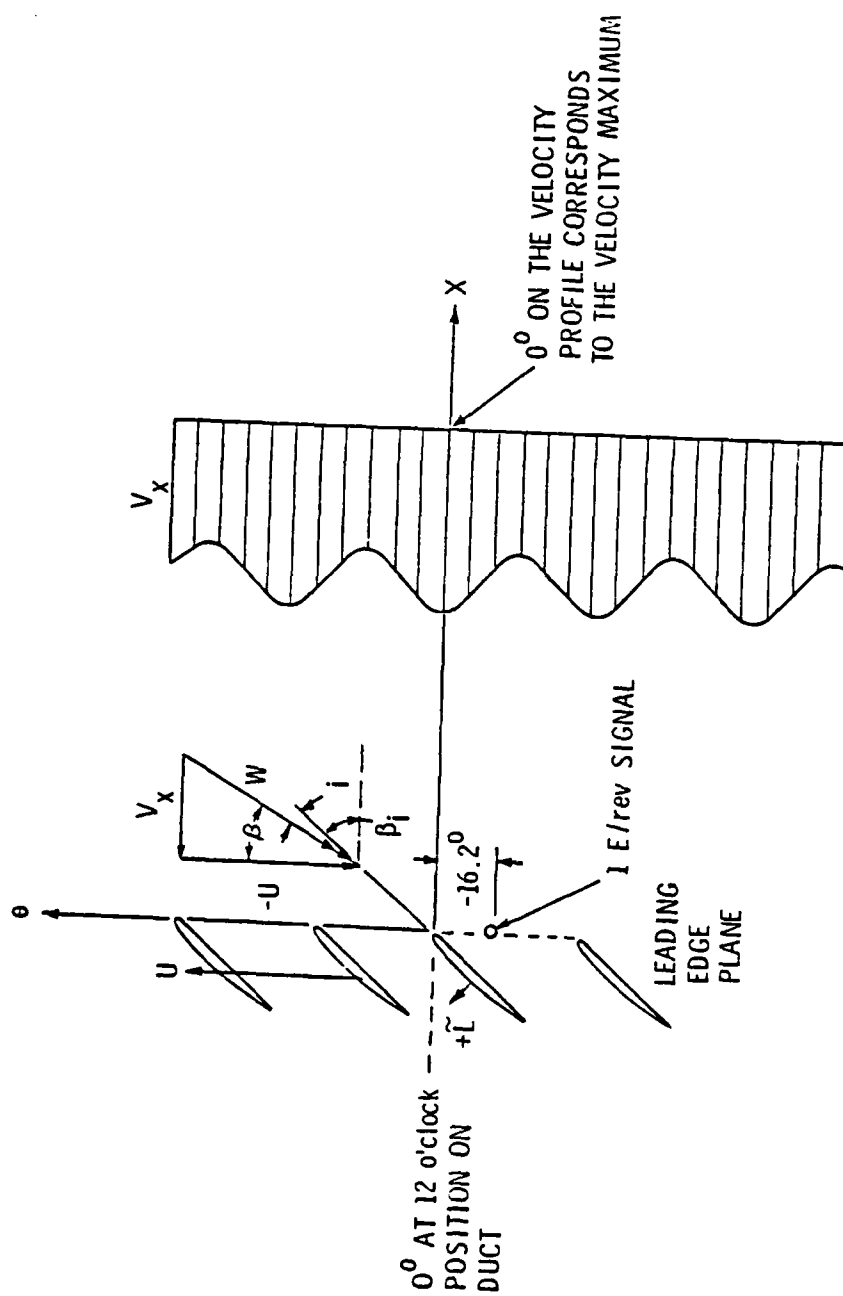


Figure 13. Flow Orientation and Reference for Phase Angle Measurement

$$\phi = \frac{\bar{V} x}{r\omega}$$

Thus, a varying ϕ means a varying i_m , and a constant ϕ designates a constant i_m .

Operation with $i_m = 0^\circ$, $\phi = 0.66$, would have been desirable for the experiment, but was not possible because of the power limitations of the auxiliary fan to maintain $i_m = 0^\circ$ over the range of test rotor speeds. The highest flow coefficient possible with the auxiliary fan over the test range was 0.60, which produced an $i_m = 2.9^\circ$.

The test matrix of the unsteady lift and acoustic pressure measurement is shown in Table II. The test variables are listed below:

- (1) The number of cycles of inflow distortion were varied.

The 8-, 9-, and 10-cycle screens were used to generate the co-rotational first higher order (1,0) mode, the plane wave (0,0) mode, and the counter-rotational (-1,0) mode, respectively, by generating flow distortions that interacted with the 9-bladed rotor. Each screen also produced a different reduced frequency. The zero-cycle distortion (a circumferentially uniform flow) represented the reference condition in which the background noise and unsteady lift levels were measured.

- (2) Two flow coefficients were considered, $\phi = 0.56$ and $\phi = 0.60$, corresponding to mean incidence angles of 4.6° and 2.9° , respectively. A study was also performed to investigate BPF tone levels for a range of flow coefficients. This is described in Appendix C.

- (3) Rotor speeds were chosen to have BPF's below, equal to, and above the cut-off frequency for the (1,0) mode of the duct. The

TABLE II
TEST MATRIX OF UNSTEADY LIFT AND ACOUSTIC
PRESSURE MEASUREMENTS

Test Variable		Measurement		Unsteady Lift	Acoustic Pressure
Disturbance Screen	Flow Coefficient	Rotor Speed (rpm)	Cutoff Ratio (f/f^*)	Spectrum/Harmonic	Spectrum/Harmonic
0-Cycle	0.56 and 0.60	1290	0.70	↓ ↓	↓ ↓
		1480	0.80		
		1760	0.95		
		1867	1.00		
		1900	1.025		
		1946	1.05		
		2038	1.10		
		2100	1.13		
9-Cycle	0.56 and 0.60	1290	0.70	↓ ↓	↓ ↓
		1480	0.80		
		1760	0.95		
		1867	1.00		
		1900	1.025		
		1946	1.05		
		2038	1.10		
		2100	1.13		
10-Cycle	0.56 and 0.60	1290	0.70	↓ ↓	↓ ↓
		1480	0.80		
		1760	0.95		
		1867	1.00		
		1900	1.025		
		1946	1.05		
		2038	1.10		
		2100	1.13		
8-Cycle	0.56 and 0.60	1110	0.60	↓ ↓	↓ ↓
		1290	0.70		
		1432	0.77		
		1480	0.80		
		1668	0.90		
		1760	0.95		
		1867	1.00		
		1900	1.025		
		1946	1.05		
		2038	1.10		
		2100	1.13		

cut-off ratio is the fraction of the generated BPF compared to the cut-off frequency for each duct mode. Selected rotor speeds were repeated for the 9- and 10-cycle screen tests for comparison with Lee's data. More speeds were considered for the 8-cycle tests since no previous data had been taken with the 8-cycle screen.

2.6 Experimental Accuracy, Repeatability, and Possible Sources of Error

2.6.1 Velocity Surveys

The Slo-Syn motor which rotated the duct section downstream of the distortion screen was controlled by an indexer with a resolution of 1/80th of a degree incremental adjustment. Since flow measurements were performed at two-degree circumferential increments, insignificant error could be expected to result from circumferential positioning. Each velocity measurement was repeated at least three times on different days and the computed harmonic levels repeated to within 10% of each other for all readings. The reference velocity profiles, shown in Figure 14, show up to a 7% variation of flow velocity from the mean closest to the duct wall. The ideal case for these surveys, of course, would be a straight horizontal line indicating a circumferentially uniform inflow. The nonuniformities evident in the flow thus introduce appreciable harmonic levels other than the fundamental. Limitations had to be made on screen design also, since the screening overlaps could only be cut so narrow before they would break apart. The ideal distortion screen would have to have infinitesimally small circumferential screen overlays to conform to a sinusoidal resistance coefficient versus circumferential angle

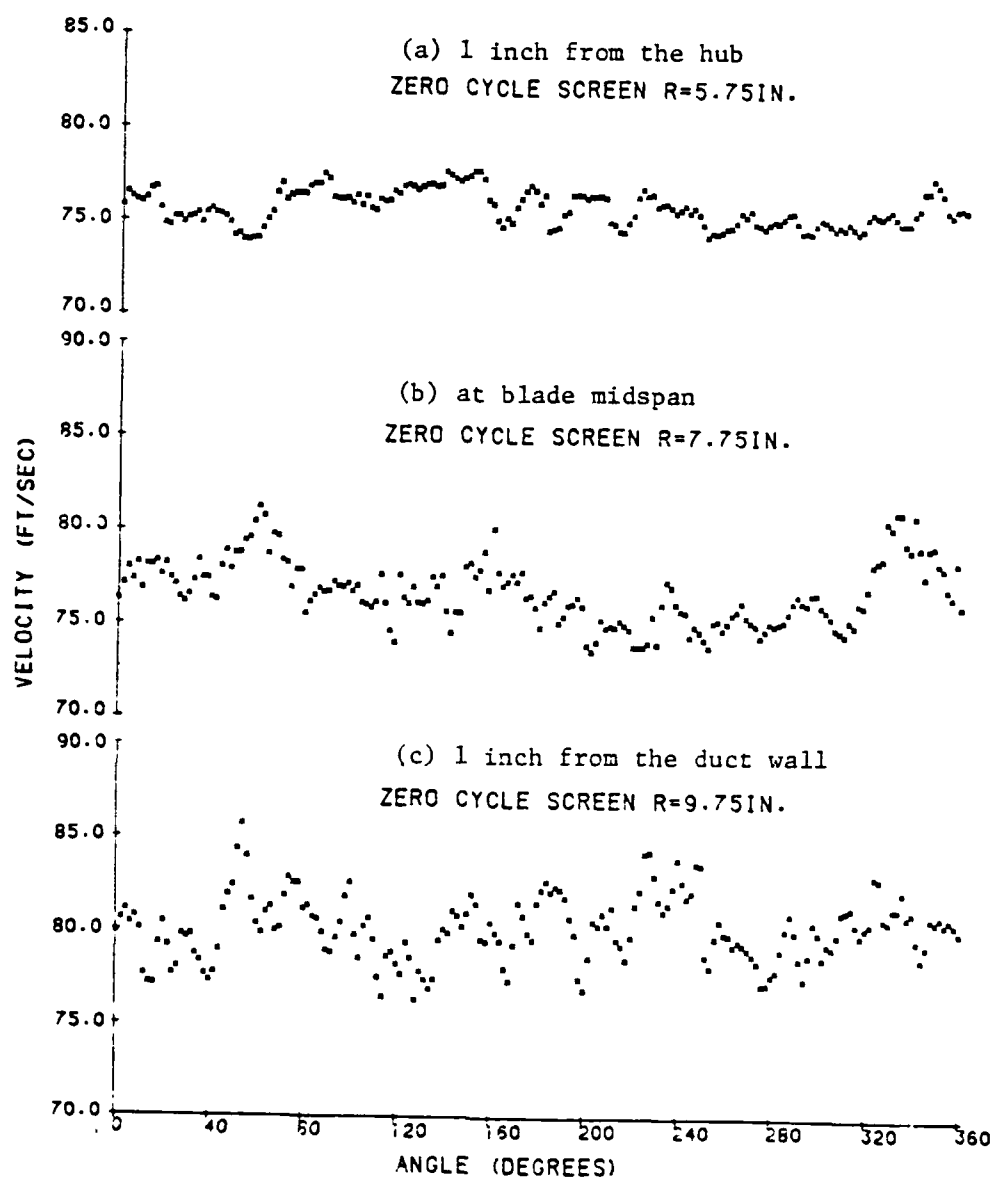


Figure 14. 0-Cycle Distortion Screen Velocity Profiles for Constant \bar{V}_x at Three Radial Locations

curve. Compromises also had to be made in choosing screen overlays according to screen size and mesh availability.

Different flow results from those of Lee can be expected since, when Lee performed his measurements, no anechoic chamber was around in the inlet. Before, during, and after the construction of the anechoic chamber, flow velocity surveys were performed with no distortion screen in the duct. Although these data are not presented, it was observed that the distortions in the inlet flow were significantly reduced during chamber construction and even more so after it was completely assembled. The remaining nonuniformity of the inflow may be a factor in the discrepancy between measured and predicted values.

The pressure transducer outputs with no flow drifted slightly between surveys so they had to be zeroed before each test. This zero shift during the survey could account for some data variation.

The paper tape output itself was found to have numerous obvious mistakes which had to be corrected manually. Therefore, a mispunched reading which did not deviate enough to be noticed could have altered the stated results.

Possible errors introduced through the use of Bernoulli's equation would depend upon the Kiel probe accuracy in measuring the total flow pressure and upon the accuracy of density readings. For the Kiel probe aligned with the flow, the errors are negligible according to the manufacturers (United Sensor). The digital voltmeter used was accurate to within 0.0005 mV and the density values were accurate to within 0.005 kg/m^3 . Substituting these values, with appropriate calibration conversion factors, into Bernoulli's equation and comparing with mean flow velocities, it can be seen that a maximum

error of 0.1% can occur by using these instruments, demonstrating that negligible instrument error is introduced.

With all of the factors owing to possible error, harmonic levels were still accurate enough to produce the desired conditions in the experiment.

2.6.2 Unsteady Lift and Acoustic Pressure Measurement

The signal coming from the microphone and lift gage were ensemble averaged 256 (2^8) times for both the spectrum and harmonic phase-locked analysis options on the SD 360 analyzer. Phase-locked analysis preserves periodic signals and tends to average out non-periodic signals due to the large number of sums (256) being taken. This isolates the desired periodic signals caused by the interaction between the distorted flow generated by the screens and the rotor by removing the uncorrelated effects. Furthermore, comparisons between spectral BPF levels and ninth harmonic levels for microphone readings were very good (to within ± 3 dB for most readings), indicating that the modes are being isolated properly by the screens and that these modes clearly dominate the sound pressure field in the duct. The main difference between these two types of measurements is that the spectral analysis involves both rotor-locked and turbulence energy levels while harmonic analysis averages out turbulence effects and only deals with rotor-locked levels. The comparison of these levels is discussed in greater detail in Appendix D.

Each unsteady lift and acoustic pressure measurement was repeated at least four times, each on a different day. One the whole, the acoustic pressure and unsteady measurements repeated to within

± 5 dB for low BPF's and to within ± 3 dB for BPF's above a cut-off ratio of 0.9. Phase angle readings varied to within $\pm 5^\circ$ for most cases.

The pistonphone calibrator for the microphone was stated by the manufacturer to be accurate to within ± 0.2 dB for the 124 dB reference tone level. However, levels were varied to within ± 1 dB between calibrations, which were performed each day before measurements commenced. The fragile nature of the microphones used required very careful handling when changing microphone positions and any slight unnoticed damage to a microphone diaphragm could cause extra variations in the data. The lift gage amplifier had to be zeroed before each test due to a zero drift which occurred during the experimentation capable of introducing errors of up to 2 dB. All readings were averaged for final inspection so the results listed are not those from one test only.

2.7 Background Levels and Data Validity

Figure 15 shows a typical spectrum plot of broadband noise levels of the AFRF for the range of rotor speeds under observation. It can be seen that BPF peaks are from 15 to 40 dB higher than broadband levels and the broadband level for the highest rotor speed observed is within 10 dB of the level for the lowest rotor speed. Thus, background levels due to the entire apparatus are much lower than those of interest (the discrete BPF peak levels).

Figure 16 shows a spectral comparison of microphone outputs with the rotor operating above cut-off for the first higher order mode with 0-, 8-, 9-, and 10-cycle screens installed. The zero-cycle screen measurements represent the background levels. It can be seen that,

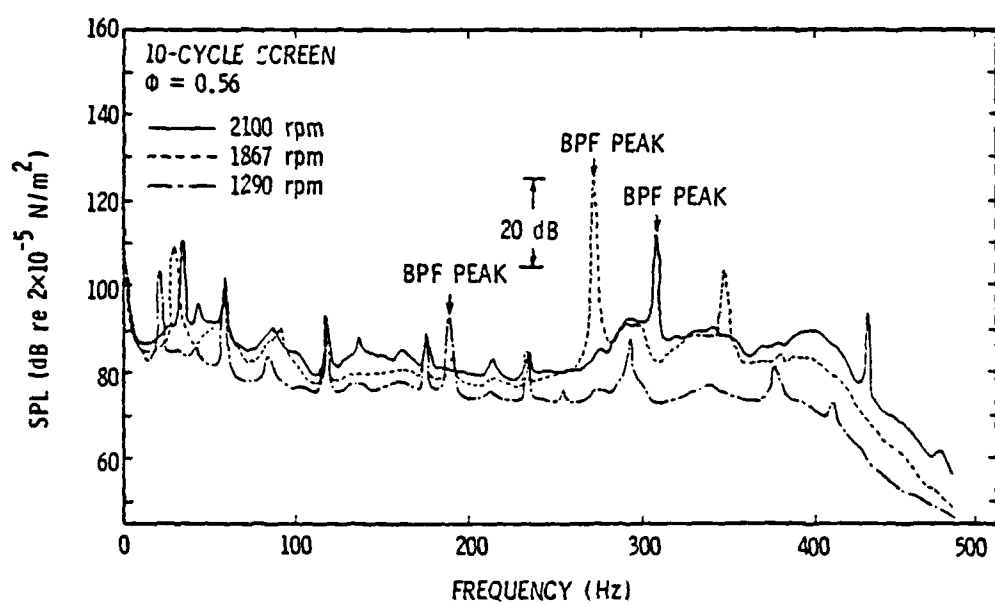


Figure 15. Typical Broadband Levels versus Rotor Speed for the AFRF

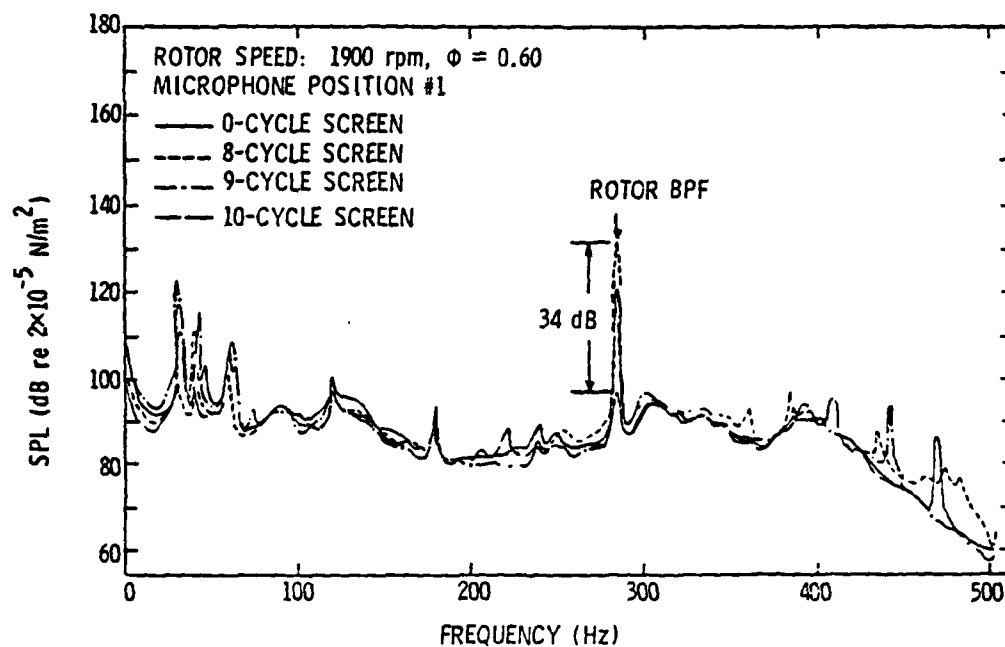


Figure 16. Spectral Comparison of Microphone Outputs Above the Cut-Off Frequency for the (1,0) Mode

at BPF for this rotor speed, the background noise level was 34 dB lower than the signal level for 8-cycle screen data and 24 dB lower than the signal level for 9- and 10-cycle screen data, which indicates an excellent signal-to-noise ratio. This difference in levels is due to the different fundamental harmonic levels for each screen.

Figure 17 shows a spectral comparison of lift gage outputs with the cascade operating above the cut-off for the first higher order mode with 0-, 8-, and 10-cycle screens installed. The tones at integer multiples of the shaft rotation frequency were generally within 5 to 10 dB of each other with any screen installed, but at the eighth harmonic of the shaft frequency for the 8-cycle screen and the tenth harmonic of the shaft frequency for the 10-cycle screen, there was a difference in levels of 30 and 32 dB, respectively. Since these were the frequencies of interest in the study, the plots show a signal-to-noise ratio which is high enough for the lift data to be considered valid.

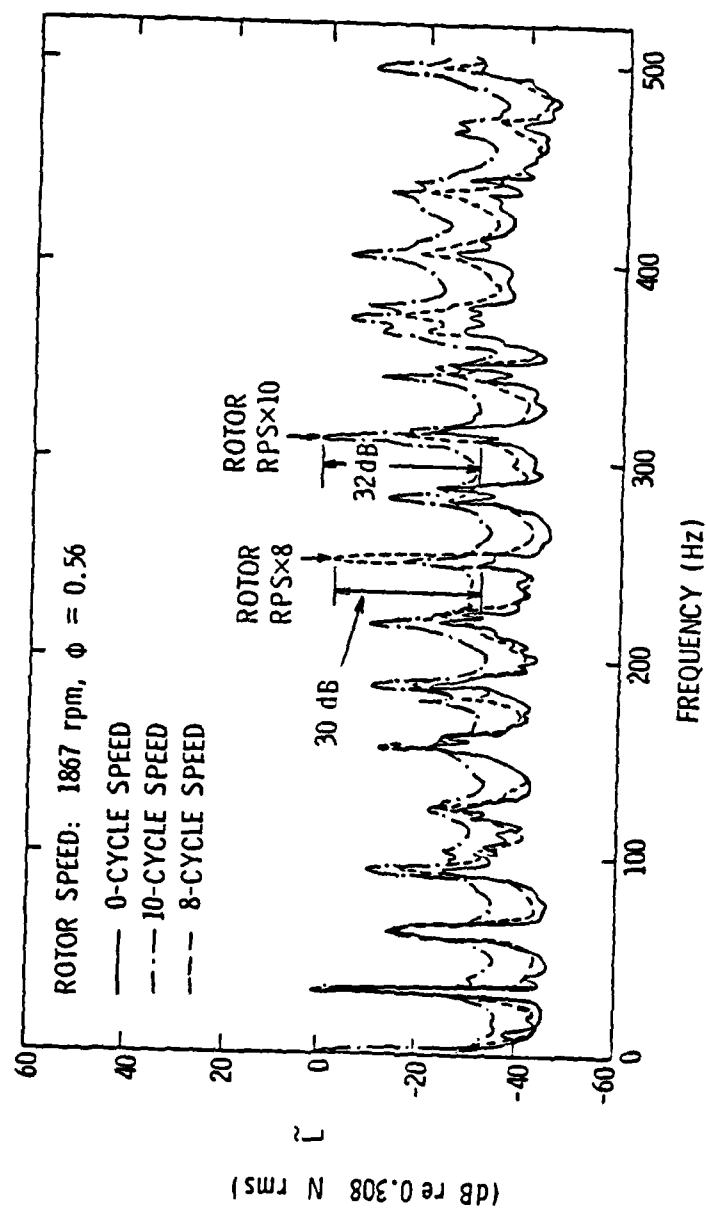


Figure 17. Spectral Comparison of Lift Gage Outputs Above the Cut-Off Frequency for the (1,0) Mode

CHAPTER III

THEORY, RESULTS, AND COMPARISON WITH THEORY

3.1 Acoustic Fields in Annular Ducts

3.1.1 General Acoustic Pressure Field

The solution to the wave equation in cylindrical coordinates, with appropriate boundary conditions applied, for a hard-walled annular duct with no mean flow is [23]:

$$p(r, \theta, x, t) = \sum_{mn} p_{mn} E_{mn}(k_{mn} r) \exp i(a_{mn} k_{mn} x + m\theta - t) \quad , \quad (1)$$

where m and n are the circumferential and radial mode orders, respectively. The axial wavenumber k_x is $a_{mn} k_{mn}$ which can be expressed as:

$$a_{mn} k_{mn} = k_x = k_{mn} \sqrt{1 - \frac{1}{\gamma^2}} \quad ,$$

or

$$a_{mn} = \frac{k_x}{k_{mn}} = \sqrt{1 - \frac{1}{\gamma^2}} \quad , \quad (2)$$

where γ is the cut-off ratio, which is the ratio of the modal frequency to the modal cut-off frequency, f^* , and E_{mn} is the radial mode function defined by:

$$E_{mn} = C_{mn} [J_m(k_{mn} r) + Q_{mn} Y_m(k_{mn} r)] \quad , \quad (3)$$

J and Y being Bessel functions of the first and second kind, respectively. The expansion coefficients, Q_{mn} , and the eigenvalues, k_{mn} , are determined from the duct inner and outer wall boundary conditions.

For a hard-walled duct, the radial pressure gradient must be zero at the walls, so

$$\frac{\partial}{\partial r} J_m(k'_{mn}) + Q_{mn} \frac{\partial}{\partial r} Y_m(k'_{mn}) = 0 \quad (4a)$$

and

$$\frac{\partial}{\partial r} J_m(k'_{mn}\sigma) + Q_{mn} \frac{\partial}{\partial r} Y_m(k'_{mn}\sigma) = 0 \quad (4b)$$

will determine Q_{mn} and k_{mn} . k'_{mn} denotes the modal wavenumber normalized by the duct outer radius, r_a , or

$$k'_{mn} = k_{mn} r_a$$

and σ is the hub-to-tip ratio. C_{mn} in Equation (3) is a normalizing constant ensuring that the integral of the pressure across the duct is unity, so C_{mn} is determined from

$$\frac{1}{C_{mn}^2} = \frac{\pi}{2} \left\{ \left[1 - \left(\frac{m}{k'_{mn}} \right)^2 \right] \left[J_m(k'_{mn}) + Q_{mn} Y_m(k'_{mn}) \right] - \left[\sigma^2 - \frac{m}{k'_{mn}} \right]^2 \left[J_m(k'_{mn}\sigma) + Q_{mn} Y_m(k'_{mn}\sigma) \right] \right\} \quad (5)$$

Observation of Equation (2) reveals that, below $\gamma = 1$ for a particular mode, k_x is purely imaginary and when replaced into Equation (1) introduces an exponential decay multiplication factor in the pressure field for that mode. Above $\gamma = 1$ for the same mode, k_x is purely real and yields real and imaginary, sinusoidally varying pressure fields in the duct. When $\gamma = 1$ for this mode, $k_x = 0$ and a non-decaying pressure field is attained. Physically, this means that sound generated in the duct below the frequency for which $\gamma = 1$ for a certain mode will decay exponentially along the duct, and for $\gamma \geq 1$, a pressure field will propagate along the duct. This frequency, the so-called cut-off frequency for a particular mode, is the frequency which satisfies Equation (4a) for a particular m and n value. Therefore, since the zeroes for the derivatives of Bessel functions increase with increasing order, the cut-off frequencies for higher order modes are successively higher.

f^* can also be expressed as:

$$f^* = \frac{k_{mn} c}{2\pi}, \quad (6)$$

c being the speed of sound. Due to the temperature dependence of c , f^* varies with temperature. Realizing that, for average room temperature ranges,

$$c = 20.05 \sqrt{273.2 + T} \quad (7)$$

for c in meters/second, and where T is the temperature in degrees centigrade, Equation (6) can be rewritten as:

$$f^* = \frac{k_{mn}}{\pi} 10.03 \sqrt{273.2 + T} \quad (8)$$

to yield an approximate cut-off frequency as a function of temperature. Since k'_{10} for the AFRF is 1.427 (computed from Reference [10]), a plot of f^* versus temperature can be generated (shown in Figure 18). This shows that, over a range of normal operating air temperatures (20°C to 35°C), f^* can vary as much as 7 Hz.

The lowest order mode, the (0,0) plane wave mode, always propagates axially along the duct and thus has a cut-off frequency of 0 Hz. For higher order modes and above cut-off, one can solve Equation (1) to find (setting the argument of the exponential equal to a constant) that the modal sound pressure field rotates or spins at a constant angular velocity around the axis of the duct as it propagates along the duct. This spinning mode wavefront travels at a helix angle, α , relative to the axial direction, given by:

$$\alpha = \sin^{-1} \left(\frac{1}{Y} \right) \quad . \quad (9)$$

Therefore, at cut-off, $\alpha = 90^\circ$ and α decreases with increasing modal tone frequency.

Characteristic constants for the AFRF are $Q_{10} = 0.258$ and $C_{10} = 1.018$ [23]. Convected effects were ignored in the above analysis since they alter predictions by a factor of $(1 - M^2)^{-1/2}$ and M , the Mach number, was less than 0.2 in these studies, making the maximum value of $(1 - M^2)^{-1/2} = 1.02$ which is sufficiently close to unity to be neglected.

3.1.2 Standing Wave Phenomena

Acoustic resonance phenomena occur in cylindrical ducts at eigenfrequencies dependent upon the duct geometry and boundary

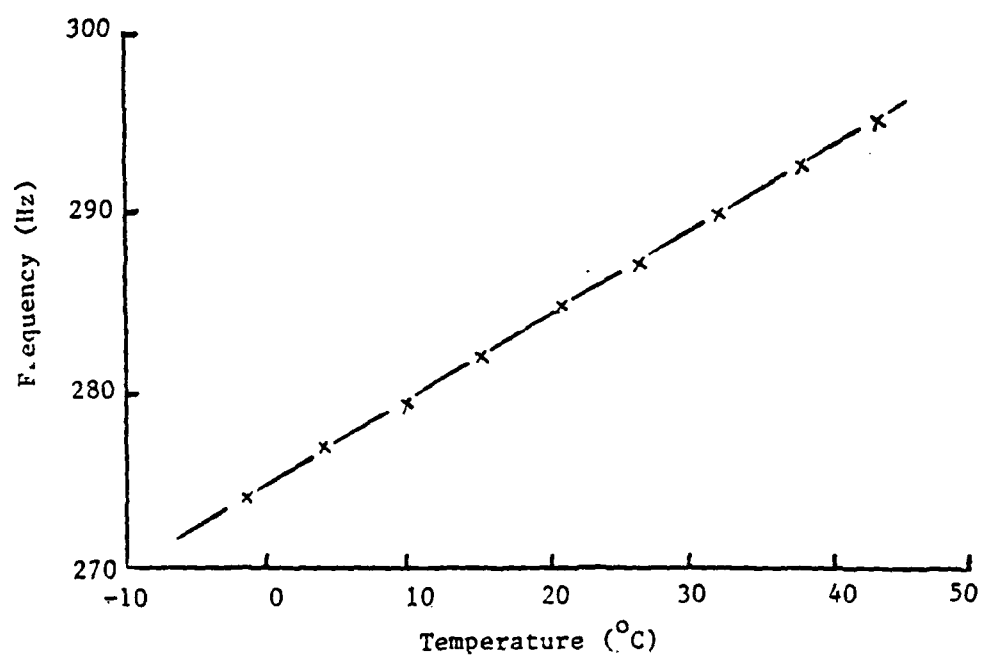


Figure 18. The Effect of Changing Temperature on the AFRF (1,0) Mode Cut-Off Frequency

conditions. Acoustic pressure measurements were performed on the duct wall between the rotor cascade and the AFRF bellmouth inlet, and lift measurements were taken at midspan of a rotor blade in the cascade, so the region of interest is between the rotor and the bellmouth inlet. At the inlet, there is an obvious open end (pressure-release) boundary condition. The rotor cascade, though not constituting a perfectly rigid boundary due to interblade spacings, should reflect some incident sound waves. The extent to which these incident waves are reflected by the rotor blades was studied in detail by Amiet [31], yet he did not take blade camber and diffraction effects into account in his analysis. Since the shortest BPF tone wavelength observed here was approximately 1.1 meters and the maximum interblade spacing of the rotor was approximately 0.2 meters, considerable diffraction around the rotor blades would be expected. Thus, acoustic pressure and impedance measurements must be performed in the vicinity (upstream and downstream) of the rotor to define the acoustic boundary condition at the cascade since Amiet's analysis would not satisfactorily model the situation. For the purposes of this study, however, suffice it to say that some reflection of acoustic pressure will occur at the rotor.

With this in mind, the AFRF (between the rotor and bellmouth inlet) could be modelled as a tube open at one end and closed at the other, in which standing waves could be set up at specific eigenfrequencies. To solve for these standing wave frequencies, each mode must be considered separately since each mode has associated with it a unique pressure pattern. Also, for an unflanged pipe with flow, an end correction factor, e , must be added [32] to the duct length, l , which is given by:

$$e = 0.6393 a - 0.1104 ka^2, \quad (10)$$

for $0.5 < ka < 2.0$ (which is the case for this study), where a is the duct radius and k is the wavenumber, $2\pi f/c$, dependent upon the modal tone frequency.

For the plane wave, wavefronts travel only axially along the duct. Therefore, the wavelength of the standing wave, $\lambda_{SW(0,0)}$, is simply $\ell + e$, or

$$\lambda_{SW(0,0)} = \ell + 0.6393 a - 0.1104 a^2 \frac{2\pi f_{(0,0)}}{c}. \quad (11)$$

Since the fixed-open end boundary conditions are assumed, standing waves should occur at odd quarter multiples of $\lambda_{(0,0)}$, or

$$\lambda_{SW(0,0)} = \frac{2n-1}{4} \lambda_{(0,0)}, \text{ where } n = 1, 2, 3, \dots \quad (12)$$

The relationship

$$f \lambda_{(0,0)} = c \quad (13a)$$

implies that

$$f \frac{2n-1}{4} \lambda_{(0,0)} = \frac{2n-1}{4} c \quad (13b)$$

which in turn implies that

$$f \lambda_{SW(0,0)} = \frac{2n-1}{4} c, \text{ for } n = 1, 2, 3, \dots \quad (13c)$$

from Equation (12). Therefore, replacing $\lambda_{SW(0,0)}$ in Equation (13c) with Equation (11), a quadratic equation in terms of $f_{SW(0,0)}$ results:

$$\left[\left(0.1104 \right) \left(\frac{2\pi a^2}{c} \right) \right] f_{SW(0,0)}^2 - (\ell + 0.6393a) f_{SW(0,0)} + \frac{2n-1}{4} c = 0, \quad (14)$$

where $f_{SW(0,0)}$ are the eigenfrequencies at which standing waves for the (0,0) mode will occur in the duct for $n = 1, 2, 3, \dots$. Due to the geometry of the AFRF and the frequency range under investigation, only the second overtone (or fifth harmonic, where $n = 3$) of the fundamental standing wave of the (0,0) mode could be encountered. This acoustic pressure pattern is shown in Figure 19. Equation (14) is thus a general expression which can be utilized for any ducted fan system whose boundary conditions approach that of a fixed-open cylindrical unflanged tube with BPF's in the range of $0.5 < ka < 2.0$.

To solve for the standing wave frequencies of the first higher order (1,0) mode, the analysis is different from that done for the (0,0) mode since spinning modes are now involved. In this case, the wavefronts are tilted at a helix angle, α , to the axial direction. Taking the boundary conditions into account and resolving into axial components, the duct length, ℓ , can be expressed as:

$$\ell = \left(\frac{2n-1}{4} \lambda_{(1,0)} - e \right) \cos \alpha, \text{ for } n = 1, 2, 3, \dots, \quad (15)$$

where e is the end correction factor defined by Equation (10) and $\lambda_{(1,0)}$ is the wavelength of the standing wave for the (1,0) mode. The helix angle, α , is defined by Equation (9) and therefore:

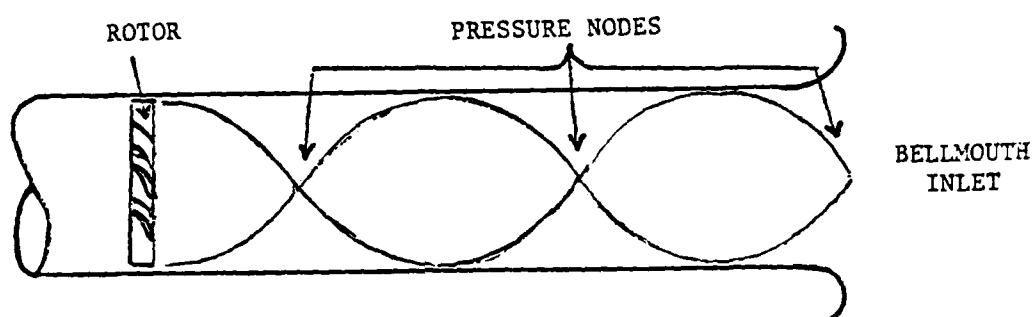


Figure 19. Acoustic Pressure Pattern for the Second Overtone (Fifth Harmonic) Standing Wave in the AFRF

$$\cos\alpha = \cos\left(\sin^{-1} \frac{f^*}{f}\right) \quad (16)$$

Tyler and Sofrin [10] identified a wavenumber, k_{xn} , for spinning duct modes as follows:

$$k_{xn} = \frac{m}{a} \sqrt{M_m^2 - \left(\frac{k'_{mn}}{m}\right)^2} \quad (17)$$

where k'_{mn} is the characteristic wavenumber associated with the hub-to-tip ratio, σ , and the number of circumferential (m) and radial (n) pressure nodal points across the annulus. Since

$$\lambda = \frac{2\pi}{k} \quad (18)$$

and

$$M_m = \frac{2\pi a f}{mc} \quad (19)$$

for the (1,0) mode:

$$\lambda_{(1,0)} = \frac{2\pi a}{\sqrt{\left(\frac{2\pi a f}{c}\right)^2 - \left(k'_{10}\right)^2}} \quad (20)$$

Substituting $\lambda_{(1,0)}$ from Equation (20), e from Equation (10), and $\cos\alpha$ from Equation (16) into Equation (15) yields:

$$\ell = \left\{ \frac{2n-1}{4} \frac{2\pi a}{\sqrt{\left[\frac{2\pi a f_{SW(1,0)}}{c} \right]^2 - \left[k'_{(1,0)} \right]^2}} - \left[0.6393a - 0.1104 \frac{2\pi a^2}{c} f_{SW(1,0)} \right] \right\} \cos \left[\sin^{-1} \frac{f^*}{f_{SW(1,0)}} \right], \quad (21)$$

where $f_{SW(1,0)}$ are the eigenfrequencies at which standing waves for the (1,0) mode will occur in the duct for $n = 1, 2, 3, \dots$. In this case, as is the case for the plane wave mode, duct geometry and operating conditions limit the possibilities of standing waves to the second overtone of the fundamental where $n = 3$.

With Equations (14) and (21), the acoustical resonance frequencies can be calculated for any duct. For the AFRE, Figure 20 shows where these standing waves should occur, according to the equations, for different temperatures. Note that the cut-off frequency for the (1,0) mode (taken from Figure 18) is, on the average, only 3.3 Hz less than the second overtone standing wave frequency for the (1,0) mode. This could cause difficulty in distinguishing between effects caused by each phenomenon.

3.2 Theoretical Coupling of Unsteady Lift Force to Acoustic Modal Pressures

In Lee's [23] attempt to couple unsteady lift to acoustic modal pressure, valid assumptions were used. His theoretical model was based on the assumptions of Whitehead [3, 4], Smith [5], and Shen [33] of:

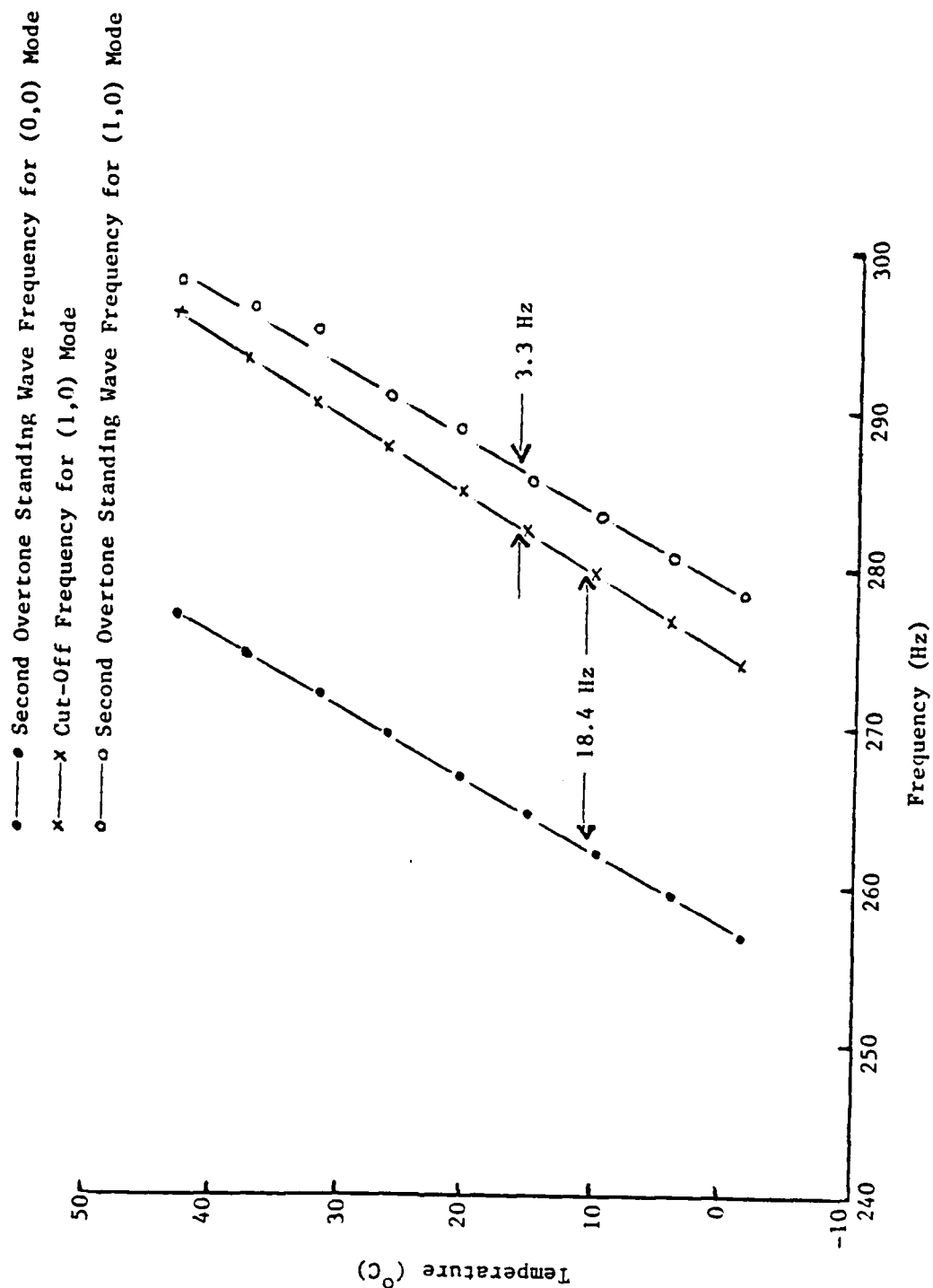


Figure 20. Temperature versus the AFRF (1,0) Mode Cut-Off Frequency and the Second Overtone Standing Wave Frequencies for the (0,0) and (1,0) Modes

- (1) two-dimensional, inviscid, and incompressible flow,
- (2) small disturbance velocity as compared with the mean velocity, W_m , and
- (3) the airfoil chamber is small enough so that the boundary condition is considered to be on the chord line instead of on the camber line.

The current test conditions are appropriate for linearized analysis and the above approximations. Lee used Shen's prediction program to calculate the unsteady lift as a function of spanwise location and employed the Tyler-Sofrin analysis to obtain the acoustic pressure by simply multiplying the lift from one blade by the total number of blades, B , in the cascade. He then resolved the lift force into the wavefront direction, spatially weighted the lift along the span of the blade by $E_{mn}(r)$, summed temporally for the unsteady force, and divided by the annular duct area to obtain the expression:

$$P_{mn} = \frac{B}{\pi(r_a^2 - r_b^2)} \int_{r_b}^{r_a} E_{mn}(r) \tilde{L} \sin(\xi + \alpha) \quad (22)$$

for the acoustic modal pressure. The unsteady lift coefficient (neglecting time harmonic dependence) used by Shen is:

$$\tilde{C}_L = \frac{\tilde{L}}{\pi C A_f \bar{V}_x W_m}, \quad (23)$$

where C is the chord line length and A_f is the fundamental harmonic of the flow from the distortion screen as compared with \bar{V}_x for each distortion screen (designed to be 0.20).

For the nine-bladed AFRF rotor cascade, velocity distortion harmonics A_8 , A_9 , and A_{10} excite the $(+1,0)$, $(0,0)$, and $(-1,0)$ modes, respectively. Figures 21, 22, and 23 show these harmonics versus mean axial velocity at three radial locations taken from the velocity surveys. These values can be read into Lee's prediction program which interpolates as necessary to obtain the values corresponding to the operating conditions.

Lee realized that reflections would be occurring in the duct which can cause standing waves, but he did not realize that they could affect the unsteady lift. His modal decomposition program calculated modal pressures at the source from the four microphone position measurements, but disregarded the effect of standing waves on the unsteady lift force. Therefore, his theoretical model with his data as input agreed well with predictions of Shen and Smith except for frequency areas around standing wave frequencies. Phase shifts for the lift measurements of up to 90° were also observed in these anomalous frequency regions, suggesting that these are resonance areas.

Accounting theoretically for these lift drops can only be accomplished qualitatively since the extent of the effect that these acoustical resonances have on the unsteady lift force is dependent upon the apparatus. Extensive measurements would have to be made in order to measure the rotor response to this back-reaction phenomenon with any reliability. A definite rise and drop in unsteady lift force is expected around standing wave frequencies for cut-on (propagating) modes. This back-reaction is physically realizable when acoustic pressure and lift values are compared. A typical acoustic SPL of

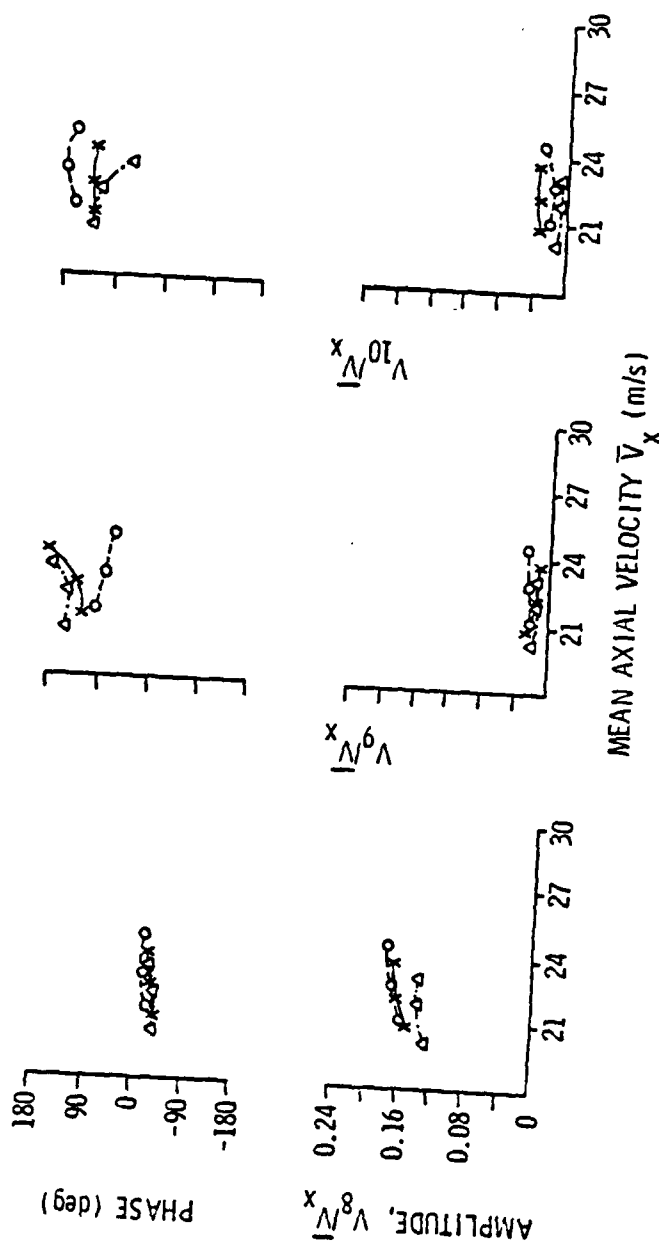


Figure 21. Fourier Harmonics of 8-Cycle Screen versus Mean Axial Flow Velocity for Current Work

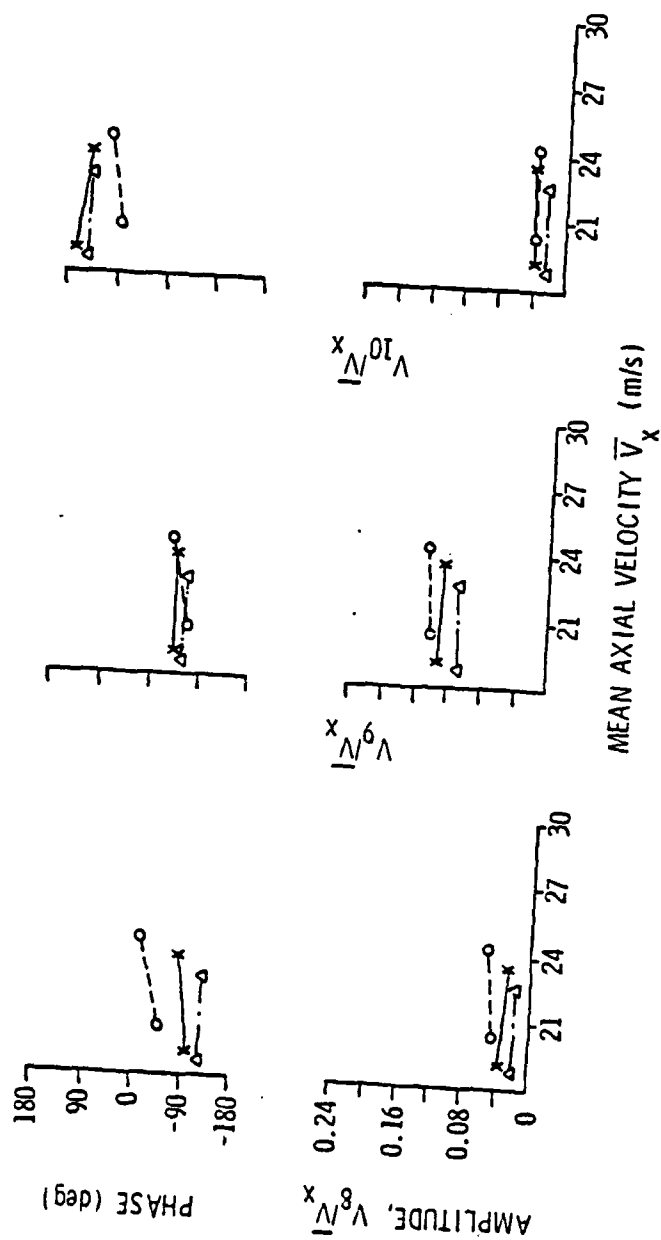


Figure 22. Fourier Harmonics of 9-Cycle Screen versus Mean Axial Flow Velocity for Current Work

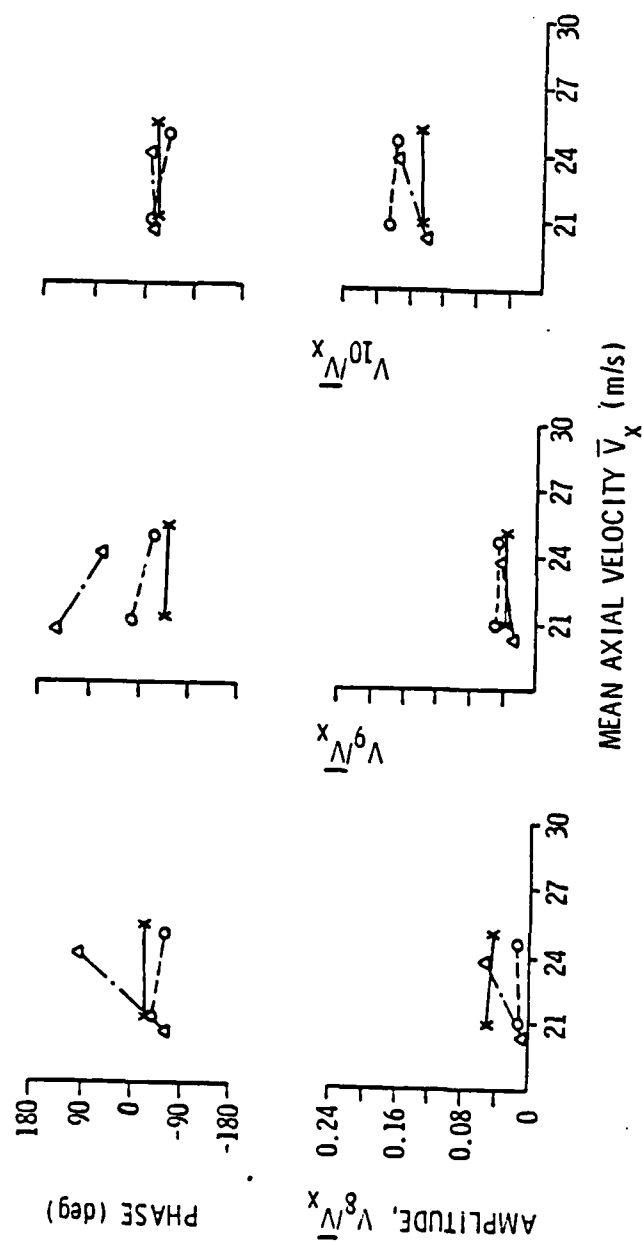


Figure 23. Fourier Harmonics of 10-Cycle Screen versus Mean Axial Flow Velocity for Current Work

125 dB (re $2 \times 10^{-5} \text{ N/m}^2$) corresponds to a pressure of 35.6 N/m^2 . When multiplied by the area of the instrumented section of the rotor blade in which the lift gage is encased ($3.87 \times 10^{-3} \text{ m}^2$), a maximum force of 0.138 N results on the lift gage as a result of the acoustic pressure. A correspondingly typical unsteady lift force level of 2 dB (re 0.308 N) applies to a lift force of 0.388 N. Therefore, it is expected that, near duct standing wave resonance, the maximum acoustic pressure may be comparable to the unsteady lift pressure. If there were to be an interaction between these two pressure fields, it would then be expected to be observed near these standing wave resonance frequencies.

Therefore, theoretically, Lee's analysis should be valid except for around standing wave BPF's, where reductions or increases in unsteady lift may occur due to acoustic back-reaction.

3.3 Comparison of Experimental Results With Theoretical Prediction

3.3.1 Propagation and Decay of Acoustic Modal Pressure Fields

In Section 3.1.1, the solution to the wave equation in cylindrical coordinates was shown to yield an infinite series of modal terms, each one exponentially decaying below a cut-off frequency and propagating above that frequency. It was stated that the plane wave (0,0) mode has a 0 Hz cut-off frequency and thus always propagates in the duct and the (1,0) mode has a cut-off frequency between 280 and 290 Hz, depending on the temperature (see Figure 18). In a separate test, these modal properties were determined by taking microphone

readings at nine different microphone positions (at identical circumferential duct locations) at rotor speeds corresponding to BPF's below and above cut-off for the $(1,0)$ mode. The results are plotted in Figure 24. Readings were taken with the 8-, 9-, and 10-cycle screens separately installed in the duct. Readings were also taken with no screen installed to determine the background levels. It can be seen that near-field effects tend to dominate the noise field at the first two microphone positions closest to the rotor and, starting at the third microphone position, the far-field modal pressure characteristics dominate the noise field. This is evident in the similar levels at the first two microphone positions as compared to the background (0-cycle screen) levels. Figure 24 shows propagation at all speeds observed for the 9-cycle screen levels, which agrees with theory since the 9-cycle screen was used to isolate the $(0,0)$ mode. The 8- and 10-cycle screen readings show a clear exponential decay for the two BPF's below cut-off for the $(1,0)$ mode and propagation for the one BPF above cut-off, which agrees very well with theory. Background levels were from 10 to 30 dB below any modal levels, making the readings experimentally valid.

Another point to note is that the distortion screen was located between the fourth and fifth microphone positions, after the near-field effects have disappeared. Because of the smooth character of the curves over this region, the distortion screen has essentially no effect on the upstream sound propagation and does not constitute any type of acoustical boundary. Thus, the decay and propagation theories for the $(0,0)$ and $(1,0)$ modes in the AFRF have been demonstrated experimentally.

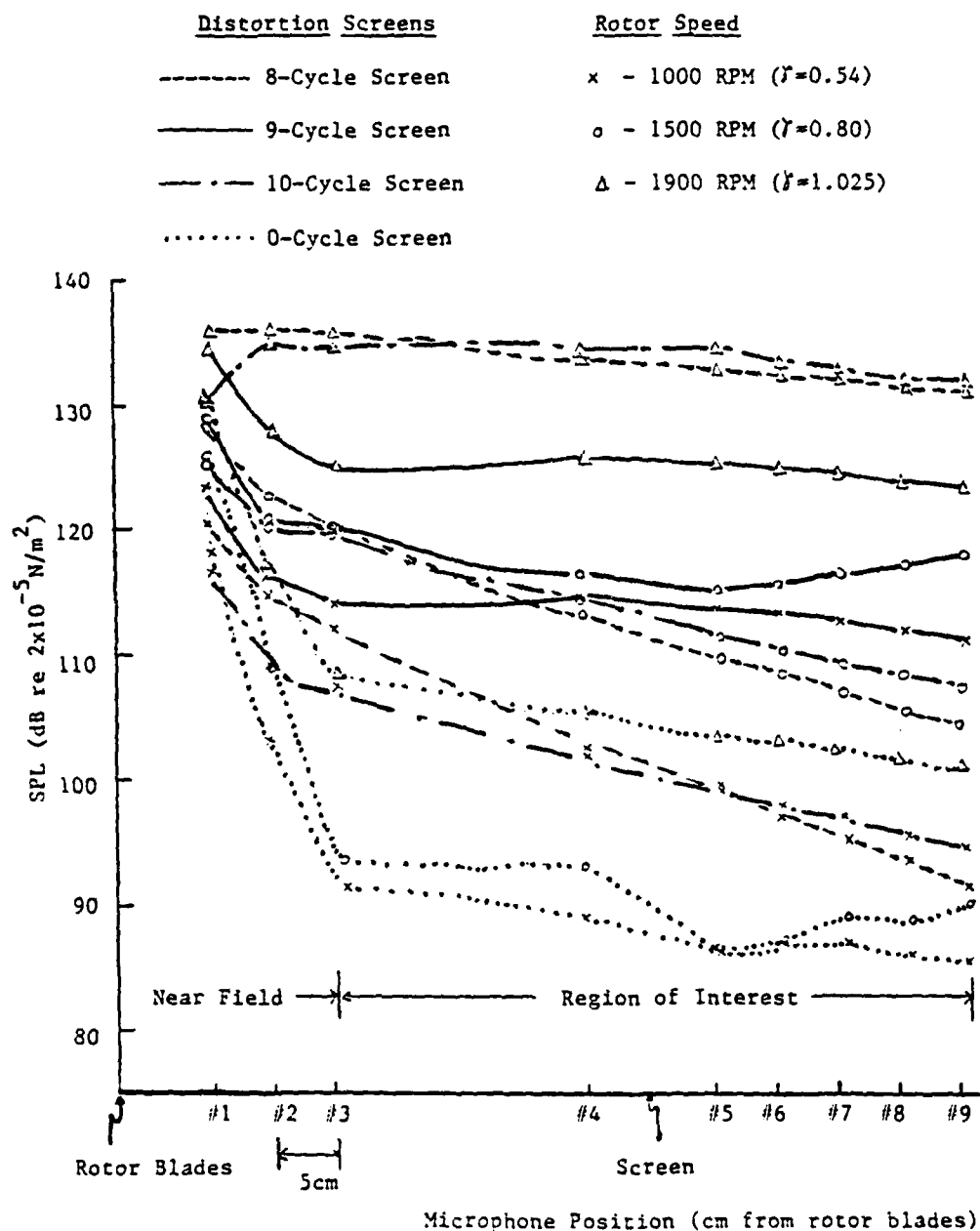


Figure 24. SPL versus Microphone Position with the 8-, 9-, and 10-Cycle Screens Installed in the Duct Below and Above the (1,0) Mode Cut-Off Frequency

3.3.2 Distortion Screen Performance

The distortion screens were designed so that the magnitude of the fundamental harmonic, A_n , non-dimensionalized by the free stream mean axial velocity, is 0.2, while all neighboring harmonics are relatively small. This results in a clear discrimination between acoustic mode generation, specifically the (0,0) and (1,0) in this case. The harmonic analysis for all screen calibrations are shown in Figures 25, 26, and 27 for the 8-, 9-, and 10-cycle screens, respectively. The 9- and 10-cycle screens had to be recalibrated because of the inflow characteristics imposed by the anechoic chamber and because of wear on the screen material. Lee reported higher levels, in general, than those observed here, yet the same basic flow characteristics as he encountered existed here also.

The coefficient A_n for the 8- and 10-cycle screens was found to be between 0.15 and 0.20, which conforms well with the design goals. Also, A_n for the 9-cycle screen was between 0.12 and 0.16, slightly lower than the design levels, yet neighboring harmonic levels were small enough for the screen to perform appropriately. For this screen, the highest neighboring harmonic to A_9 was A_8 , which was 37% of A_9 closest to the duct wall. A_{10} was the next largest harmonic level at 25% of A_9 . These would show contributions to the first higher order mode, but only manifest themselves above the cut-off frequency for that mode (i.e., 280 to 290 Hz).

The largest neighboring harmonic to A_{10} for the 10-cycle screen calibration was A_{11} at a level of 32% of A_{10} closest to the duct wall and A_9 was next higher at 26% of A_{10} . The coefficient A_9 corresponds

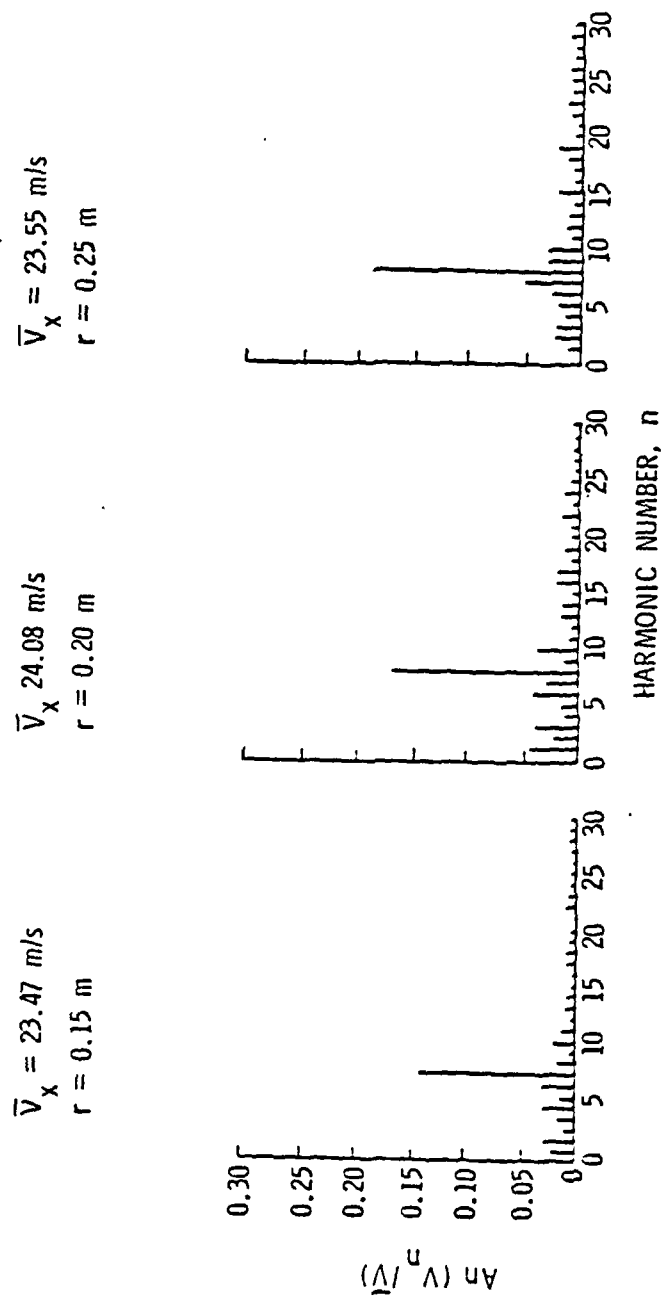


Figure 25. Fourier Harmonic Amplitudes of the 8-Cycle Screen

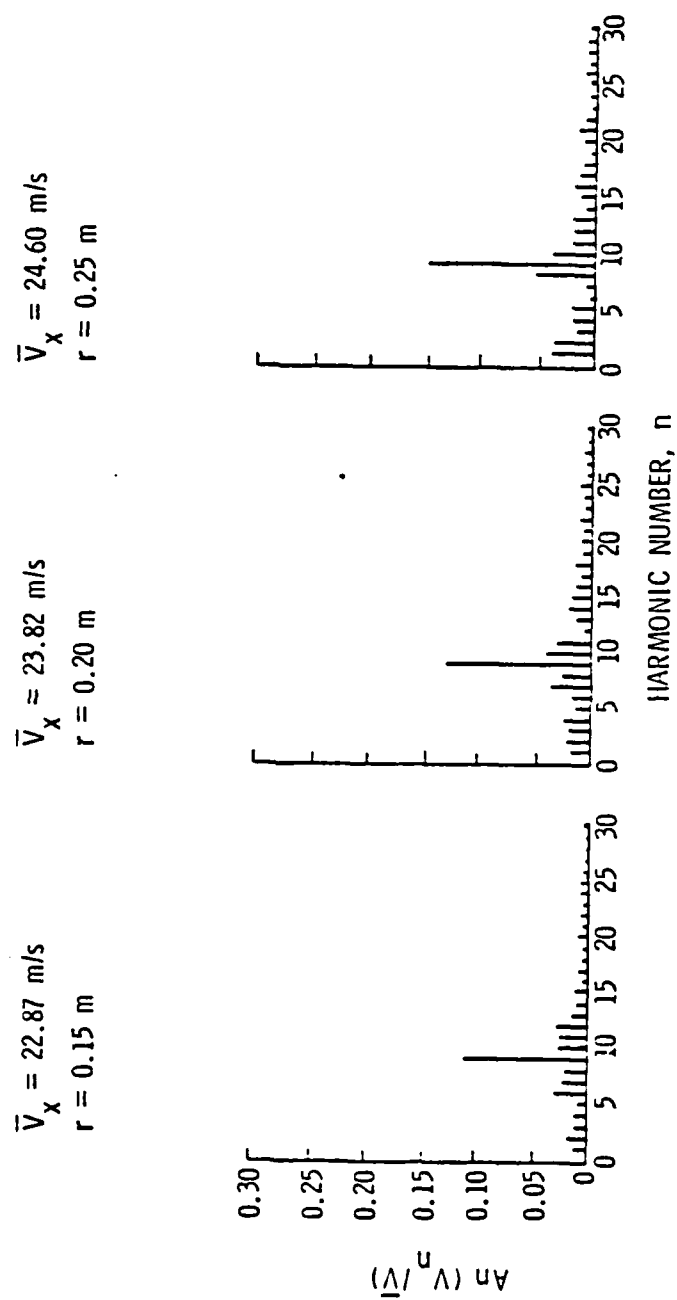


Figure 26. Fourier Harmonic Amplitudes of the 9-Cycle Screen

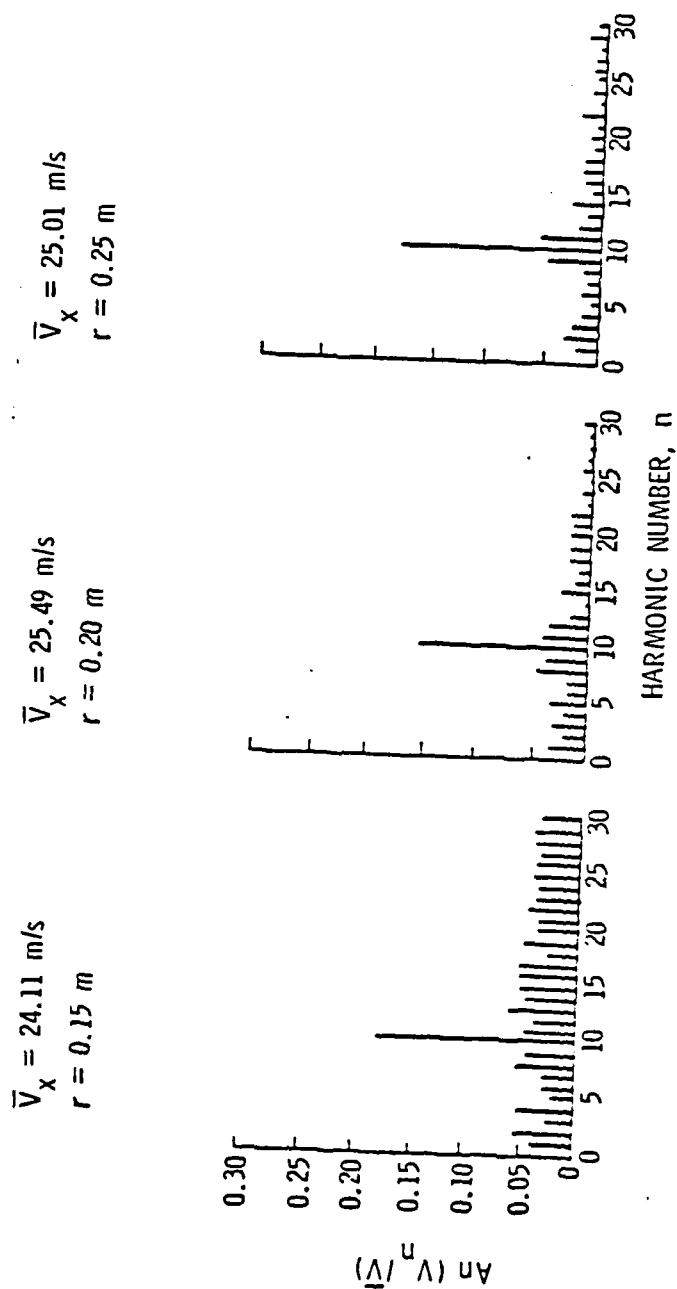


Figure 27. Fourier Harmonic Amplitudes of the 10-Cycle Screen

to the plane wave mode which always propagates in the duct, so its presence must be accounted for. Lee's decomposition model does take this into account and, since similar percentage levels were observed between calibrations, this part of the analysis seems valid. The coefficient A_{11} corresponds to the $(-2,0)$ mode which has a cut-off frequency of around 550 Hz, a BPF well out of the range of the BPF's observed in this study.

For the 8-cycle screen, A_7 was the highest neighboring harmonic to A_8 at 31% of A_8 , while A_9 and A_{10} were both approximately 18% of A_8 closest to the duct wall. The coefficients A_9 and A_{10} contribute to the $(0,0)$ and $(-1,0)$ modes, respectively, and A_7 contributes to the $(2,0)$ mode. As was stated above, the $(2,0)$ mode will only decay along the duct over the frequency range investigated here, and the plane wave and $(-1,0)$ mode have been compensated for in the decomposition model.

A further confirmation of the insignificance of the modes of order two and higher is a plot of an expression by Tyler and Sofrin [10] describing the decay rate of higher order modes (with $n = 0$) below cut-off given by:

$$\frac{\Delta dB}{\Delta x} = 8.69 \frac{2\pi}{c} \sqrt{f^* - f} \quad (24)$$

for the AFRF where x is axial duct distance. This plot is shown in Figure 28. It can be seen from this figure that, for the $(2,0)$ mode, the decay rate of the modal pressure is 69 dB/m (21 dB/ft) at the highest BPF (315 Hz) observed in this investigation and it decays even faster at lower frequencies. Also, each successively higher order mode decays at an even faster rate than that which occurs for

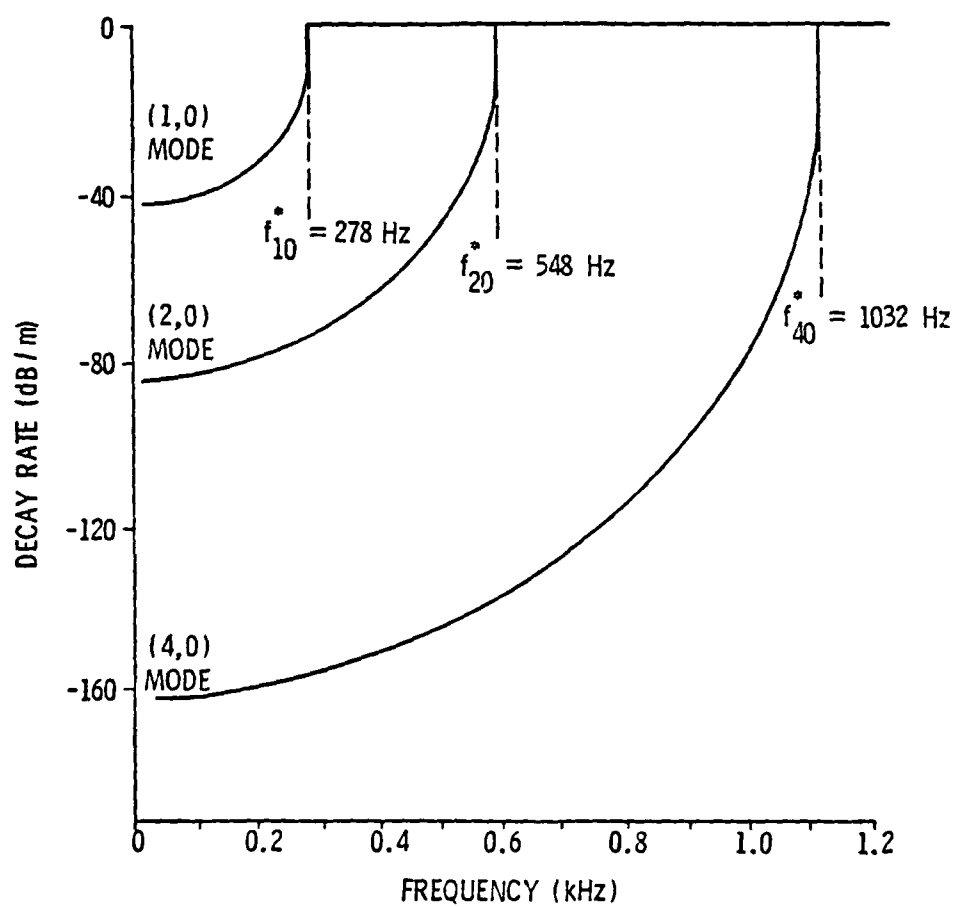


Figure 28. Modal Pressure Decay Rate for the AFRF

the (2,0) mode. Therefore, the modes of order $m = 2$ and higher can be considered negligible in contribution to the acoustic pressure field in this study and the screens perform well enough to approximate the theoretical conditions.

3.3.3 Unsteady Lift Force

Typical unsteady lift spectra are shown in Figures 29 and 30. Figure 29 shows the unsteady lift spectral peak of interest at the frequency of the rotor multiplied by the number of distortion screen cycles. The unsteady lift force at this frequency is directly associated with the acoustic modal pressure level at the rotor BPF. Figure 30 is a Fourier analysis of the output. The q value is an amplification factor which can be set on the analyzer for optimum level discrimination. The large peak level of the first harmonic is due to gravitational force and is independent of rotor speed. Further discussion of this point is presented in Lee's thesis [23]. The largest peak at the 16th harmonic is due to the mechanical resonance of the lift gage which occurs at around 500 Hz ($1900 \times 16/60 = 507$). As the shaft speed decreases, the peak moves to higher harmonic numbers. The peak of interest is at the same harmonic number as the number of distortion screen cycles (10 in the case of Figure 30).

Figures 31, 32, and 33 compare unsteady lift measurements from this investigation to those obtained by Lee on the same apparatus, non-dimensionalizing the \tilde{L} values in terms of the unsteady lift coefficient defined in Equation (23). The importance of non-dimensionalization cannot be overemphasized. Non-dimensionalization emphasizes the repeatability of the experiment under different

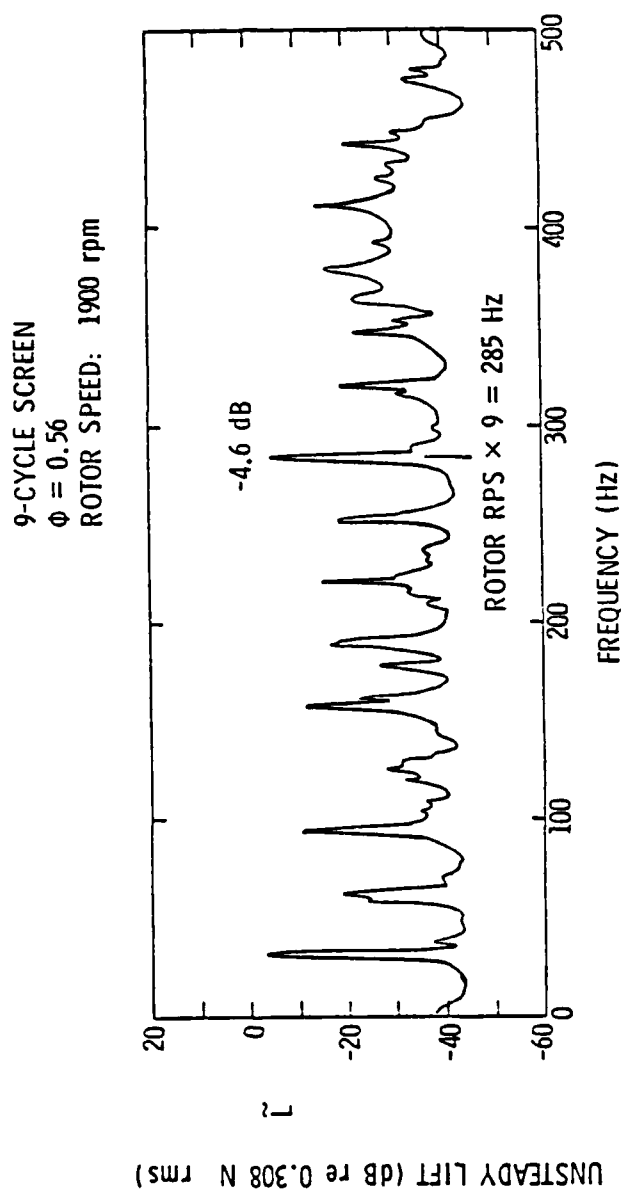


Figure 29. Typical Spectrum of Lift Gage Output

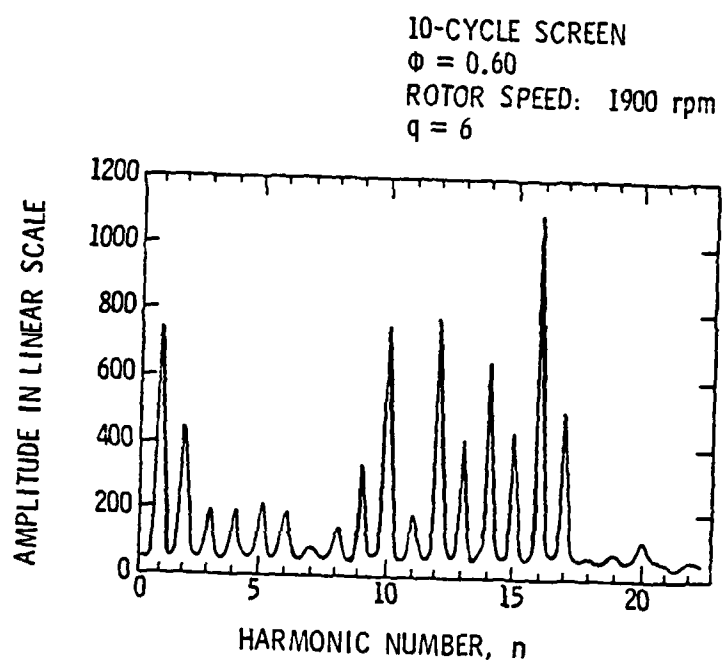


Figure 30. Typical Fourier Harmonic Analysis of Lift Gage Output

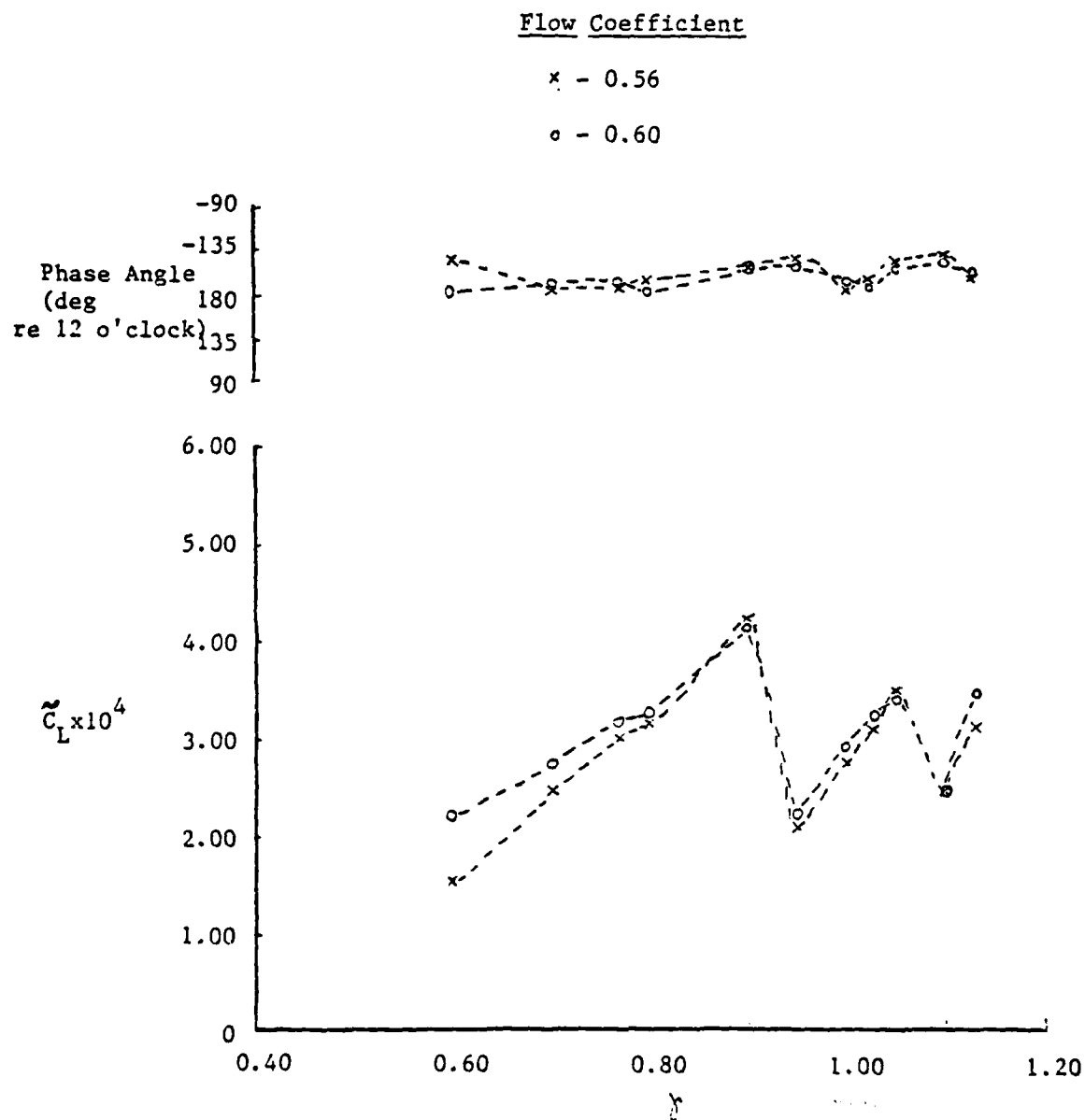


Figure 31. Unsteady Lift Coefficient versus (L/D) Ratio Cut-Off Ratio for 8-Cycle Screen Measurement for Current Work

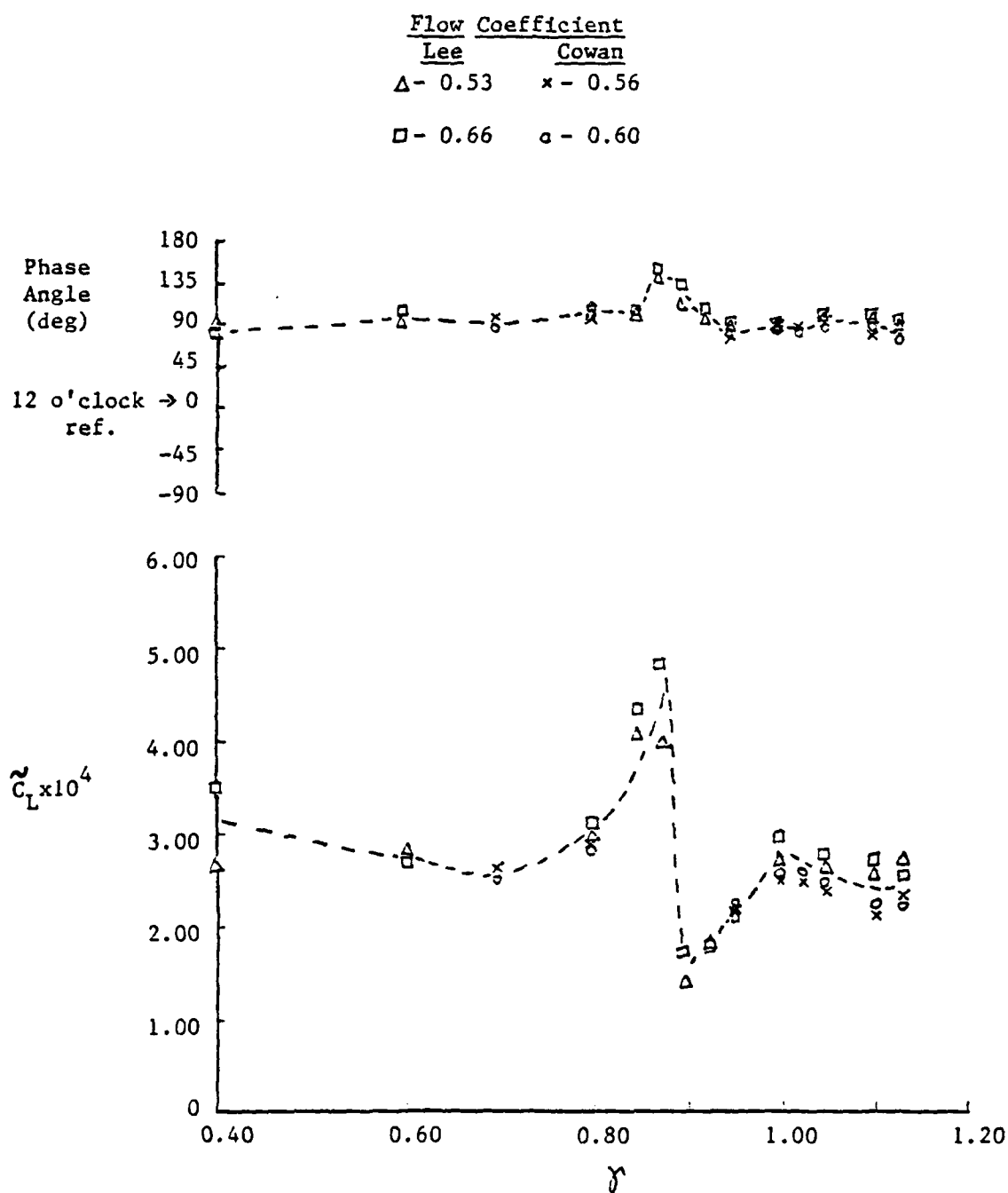


Figure 32. Unsteady Lift Coefficient versus (1,0) Mode Cut-Off Ratio for 9-Cycle Screen Measurement

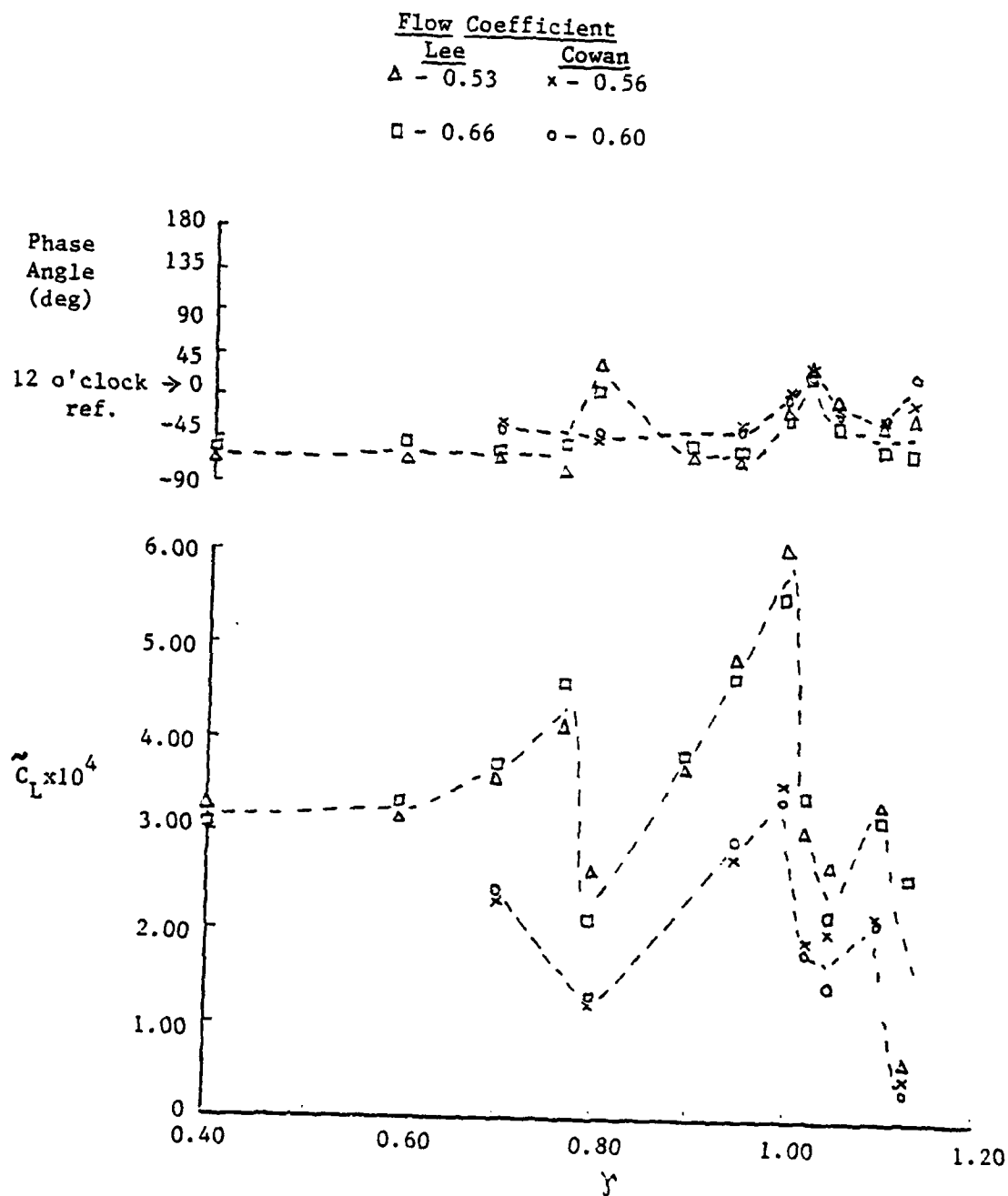


Figure 33. Unsteady Lift Coefficient versus (1,0) Mode Cut-Off Ratio for 10-Cycle Screen Measurement

operating conditions and different duct geometries. Certain significant effects may become more evident in this form which may be disregarded when observing dimensional data, as is evident from Lee's dimensional data presentation. Figure 34 presents comparisons between unsteady lift data for this and Lee's study in dimensional form with the 10-cycle distortion screen installed in the duct. General trends in the data are the same between Figures 33 and 34, yet the non-dimensional plots of Figure 33 show a significant difference in curve levels, especially around $\gamma = 1$ (which is not as clearly evident in Figure 34), between Lee's curves and those obtained here. This difference may not be considered significant if only Figure 34 were presented, yet there is some definite physical occurrence which is responsible for the level difference. The reason for these differing levels is not known and further work must be done to find this reason.

Another point to note about Lee's data is the need for a correction for the values of flow coefficient. He states that ϕ values of 0.56 and 0.70 were tested and that they correspond to mean flow incidence angles of 6.0° and 0.3° , respectively. However (looking at Figure 13), since

$$\begin{aligned}\tan \beta &= \phi, \\ 90 - \beta_i &= \beta + i_m,\end{aligned}$$

and β_i , the inlet flow angle, at midspan is 56.14° (from Table I), $\phi = 0.56$ and 0.70 correspond to $i_m = 4.6^\circ$ and -1.1° , respectively. The incidence angles quoted by Lee, $i_m = 6.0^\circ$ and 0.3° , actually correspond to $\phi = 0.53$ and 0.66 , respectively. Since Lee had performed measurements to verify his quoted i_m values, any data of

Flow Coefficient	
Lee	Cowan
Δ - 0.53	\times - 0.56
\square - 0.66	\circ - 0.60

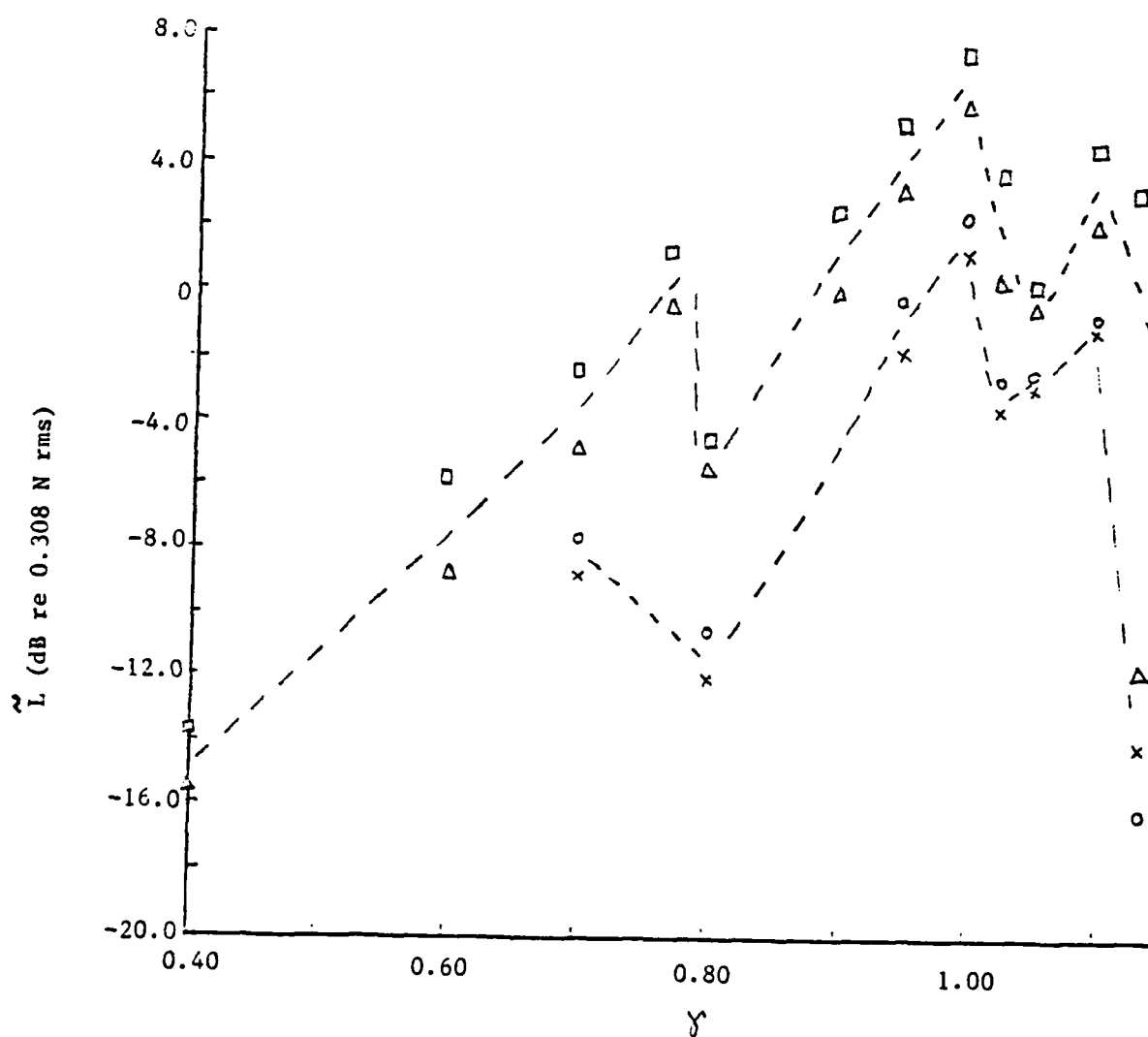


Figure 34. Unsteady Lift versus (1,0) Mode Cut-off Ratio for 10-Cycle Screen Measurement

Lee's labelled as $\phi = 0.56$ or 0.70 in his work is reported herein as $\phi = 0.53$ or 0.66 , respectively. The 0.53 flow coefficient is above the blade stall ϕ of 0.49 (solved for in Appendix C), so the measurements can still be considered valid. As is explained in Appendix C, this shift in ϕ should not vary the results substantially since the levels remain fairly close to each other within this ϕ range.

The problem remaining to resolve is that of the reduction in \tilde{L} which Lee attributed to back-reaction due to the $(1,0)$ mode cut-on phenomenon. This can be explained by the theory of Section 3.1.2. The 9-cycle screen \tilde{C}_L data (see Figure 32) exhibits one significant increase and reduction around $\gamma = 0.90$, corresponding to a BPF of 250 Hz. Substituting $n = 3$ (for the second overtone) into Equation (14) along with the proper duct geometry values yielded the left-hand side curve of Figure 20 which shows that the second overtone of the $(0,0)$ mode standing wave existed in the duct around a frequency of about 90% of f^* . Increases and reductions which occur in \tilde{C}_L for the 9-cycle screen data, occur in similar γ ranges for the 8- and 10-cycle screen data. Similarly, the unsteady lift phase shows a change of approximately 90° around this frequency. This degree of phase change indicates that there is a back-reaction effect of a value comparable to the lift (i.e., as the acoustic and lift pressure magnitudes indicate) and that this acoustic pressure back-reaction may change phase as would be expected for a single degree of freedom oscillator which would again be characteristic of the standing wave. Since, in the frequency range described above, the values of BPF are below the $(1,0)$ mode cut-off frequency, this plane standing wave

dominates the acoustic field in that frequency range with any of the three distortion screens installed in the duct. From distortion screen analysis, the ninth harmonic in Figures 25, 26, and 27 is more dominant (as was designed) for the 9-cycle screen than for the 8- and 10-cycle screens. Thus, the effect of the plane standing wave is expected to be slightly less on the \tilde{C}_L for the 8- and 10-cycle screen data than on the 9-cycle screen data. This, in fact, did occur; compare the \tilde{C}_L increase and reduction on Figure 32 with the first \tilde{C}_L increases and reductions of Figures 31 and 33. The comparable maximum acoustic pressure and unsteady lift magnitudes described in Section 3.2 also confirm the possibility of acoustic back-reaction on the rotor caused by a modal pressure standing wave.

Figures 31 and 33 exhibit a second \tilde{C}_L reduction above the (1,0) mode cut-off frequency which correspond to frequencies in the region of the second overtone of the standing wave for the (1,0) spinning mode by solving (with $n = 3$) Equation (21) for $f_{SW(1,0)}$. Phase shifts in this frequency region similar to those encountered above may indicate that resonance-related back-reaction effects are occurring. However, Figure 20 shows that there is a very small frequency difference between f^* for the (1,0) mode and $f_{SW(1,0)}$, yet they never coincide (in the temperature range of interest). There is no obvious way to determine the cause of this back-reaction due to this proximity in frequencies of interest. However, from the previous result, it would be expected that it is the standing wave rather than f^* which is controlling.

Therefore, all anomalies with Lee's data have been accounted for, both theoretically and experimentally. The data taken here agrees

AD-A124 819

INVESTIGATION OF THE COUPLING OF UNSTEADY LIFT TO LOW
ORDER ACOUSTIC DUCT..(U) PENNSYLVANIA STATE UNIV
UNIVERSITY PARK APPLIED RESEARCH LAB.. J P COWAN
17 JUN 82 ARL/PSU/TM-82-137

2/2

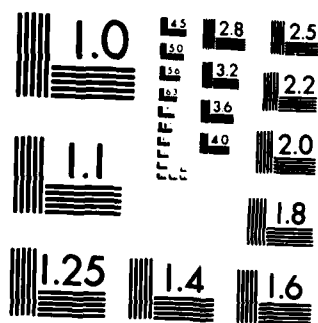
UNCLASSIFIED

F/G 20/1

NL

END
DATE
FILMED
4 83
DTIC

M-2



MICROCOPY RESOLUTION TEST CHART
NATIONAL BUREAU OF STANDARDS 1963 A

well with Lee's and, thus, without standing wave phenomena, it would agree quite well with theoretical prediction. Since Lee's data agree with prediction except near regions where the above effects would cause contamination, it would be redundant to compare the data taken here with theory and it is sufficient to compare data with that obtained by Lee.

3.3.4 Acoustic Modal Pressure

Typical acoustic pressure spectra are shown in Figures 35 and 36. Figure 35 shows a spectrum with a peak of interest at the BPF. A harmonic analysis of the phase-locked average signal is shown in Figure 36. The peaks at $n = 9$ and 18 correspond to the levels of the BPF signal and its first harmonic, respectively, since a nine-bladed rotor was used in the experiment. When the harmonic levels at $n = 9$ were converted to SPL values according to the analyzer calibration, they agreed to within ± 2 dB with spectral BPF peak readings, as is explained in Appendix D, showing strong modal isolation performance by each distortion screen.

The magnitude and phase angle readings at the four microphone positions are plotted in Figures 37, 38, and 39 with the 8-, 9-, and 10-cycle distortion screens, respectively, installed in the duct. Lee's data are also plotted in Figures 38 and 39 for comparison purposes. Note that all data quoted herein are averaged levels from at least three or four separate measurements. These comparisons reveal that, above the cut-off frequency of the dominant mode isolated by the distortion screen, Lee's BPF level readings were on the average 5 dB higher than those observed in this study. This can

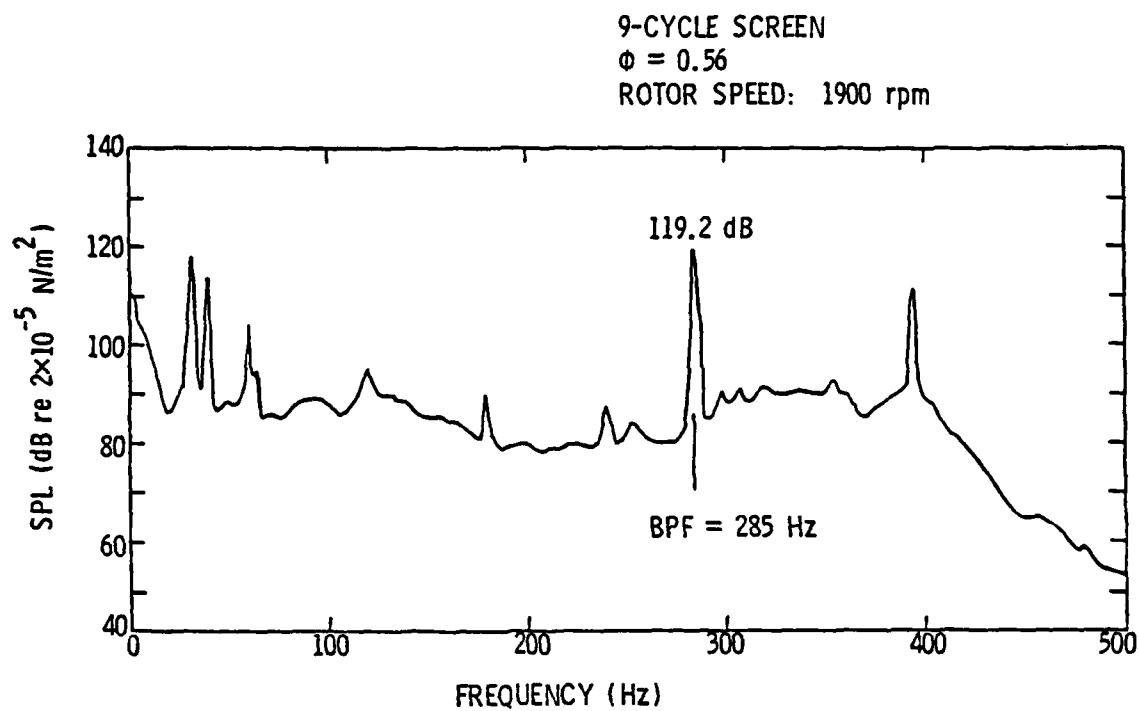


Figure 35. Typical Spectrum of Microphone Output

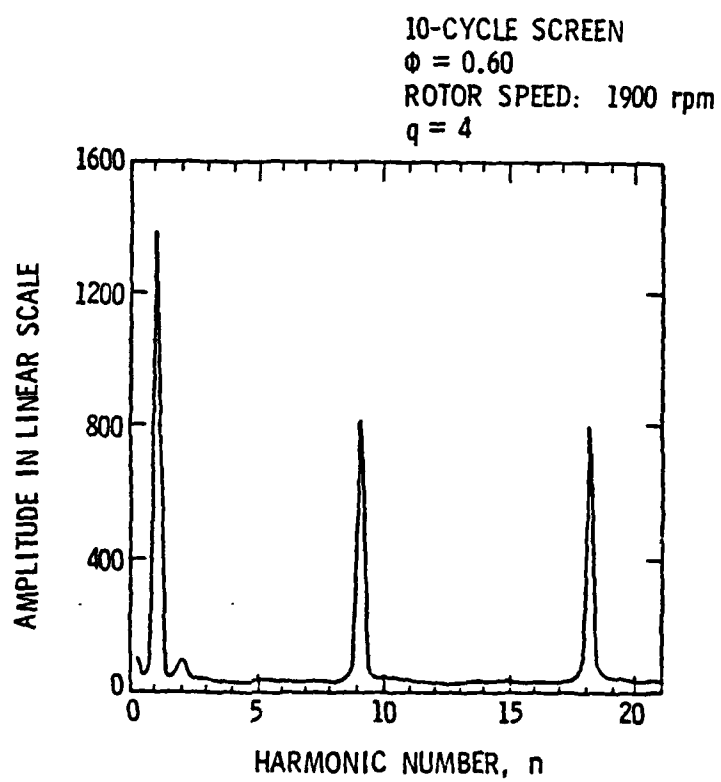
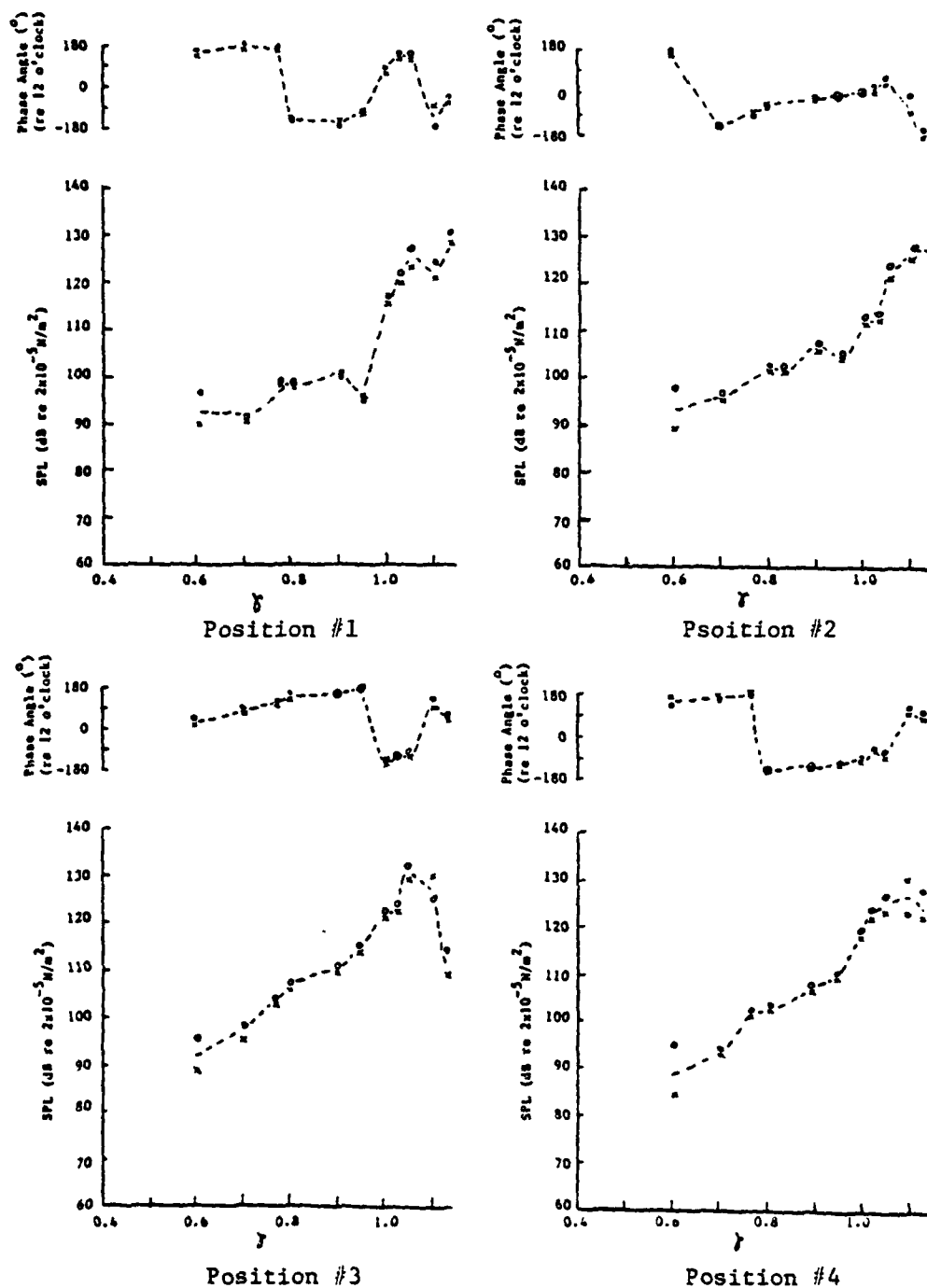


Figure 36. Typical Fourier Harmonic Analysis of Microphone Output



Flow Coefficient, Cowan: x - 0.56, o - 0.60

Figure 37. SPL Magnitude and Phase Angle Measurement versus (1,0) Mode Cut-Off Ratio for 8-Cycle Screen Measurement

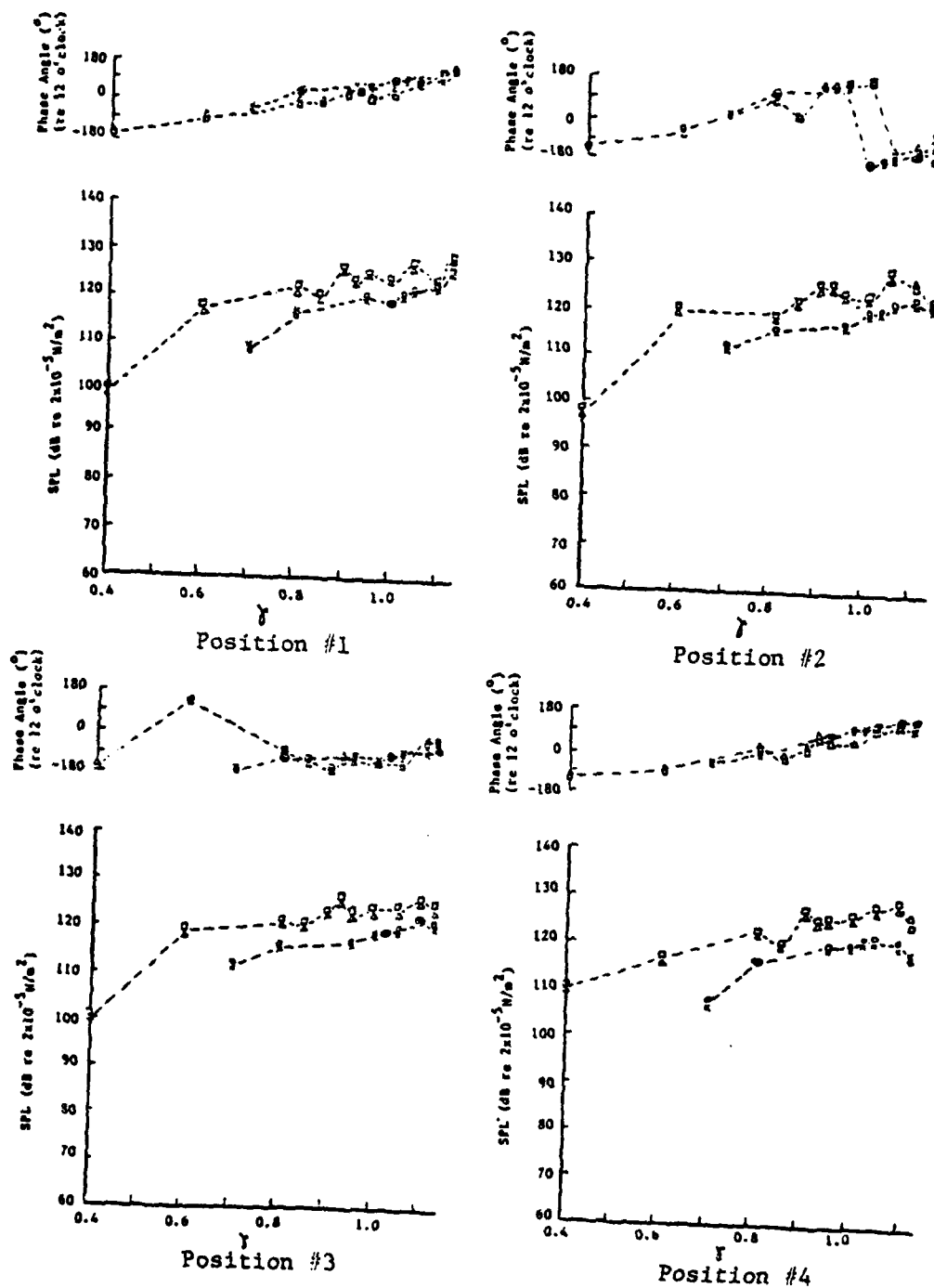


Figure 38. SPL Magnitude and Phase Angle Measurement versus (1,0) Mode Cut-Off Ratio for 9-Cycle Screen Measurement

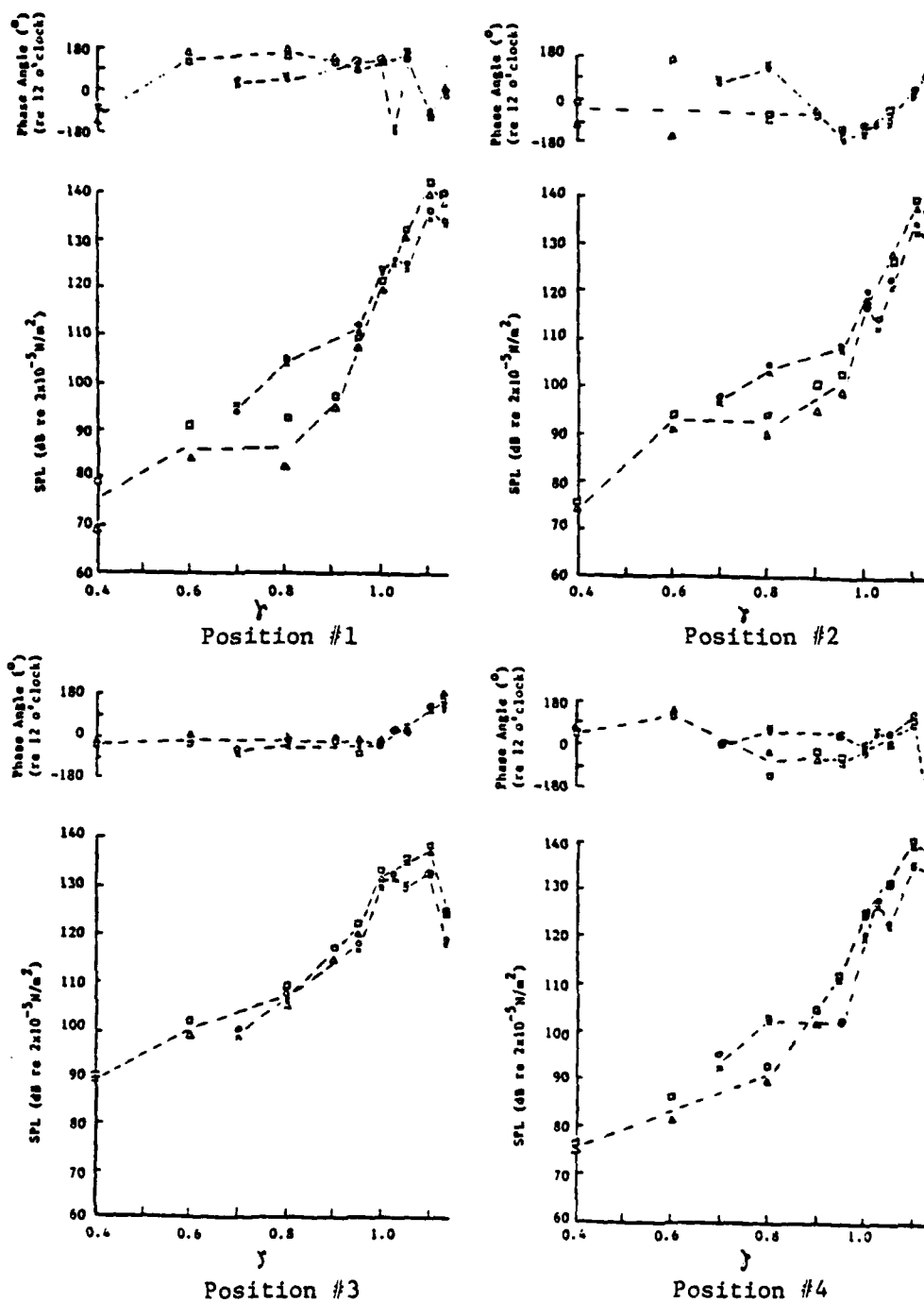


Figure 39. SPL Magnitude and Phase Angle Measurement versus (1,0) Mode Cut-Off Ratio for 10-Cycle Screen Measurement

be traced to the generally higher unsteady lift levels recorded by Lee shown in Figures 32 and 33. Below the (1,0) mode cut-off frequency for the 10-cycle screen data of Figure 39, Lee's data are comparable to data taken here.

The same general data trends observed by Lee were also observed here. Figures 37 and 39 show that a definite cut-off phenomenon existed which could also be heard by observers in the vicinity of the apparatus. The 9-cycle screen measurements of Figure 38 show little change of BPF levels with increasing rotor speed, an indication of plane wave isolation and propagation. Therefore, the acoustic pressure field in the duct was dominated by the plane wave (0,0) mode with the 9-cycle screen installed and by the (1,0) mode with the 8- and 10-cycle screens installed, conforming to basic design characteristics. In addition, the general acoustical duct theory of Section 3.1.1 were experimentally verified.

Lee theoretically predicted the steady state waveforms which would exist in the duct after reflections for the plane wave and (1,0) order modes. These plots are shown in Figures 40 and 41 along with actual data points measured at the four microphone positions. An accurate account of the integrity of these curves would obviously require many more data points to be taken along the duct. With only these four measurement locations, there is doubt as to the reliability of these curves. A much more extensive study would have to be performed in order to better describe the actual duct pressure pattern before an improvement on this theory could be attempted.

At a frequency around the plane wave second overtone standing wave frequency, readings from the four microphone positions reveal

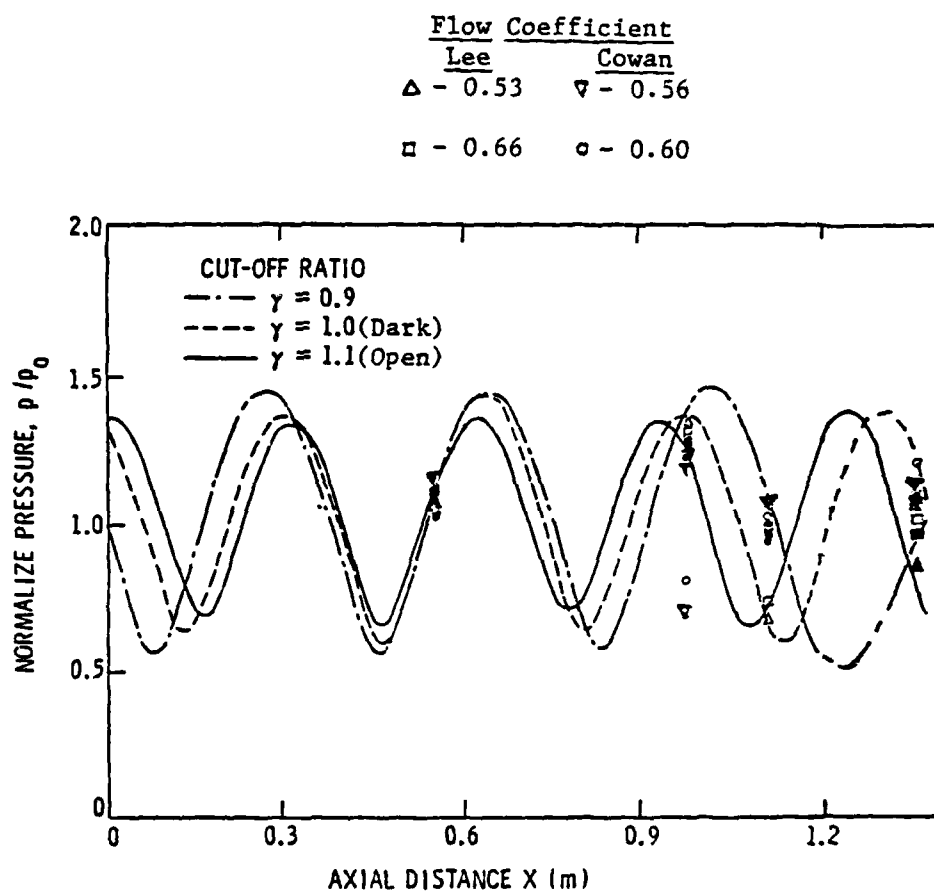


Figure 40. Predicted and Measured (0,0) Mode Steady State Waveform

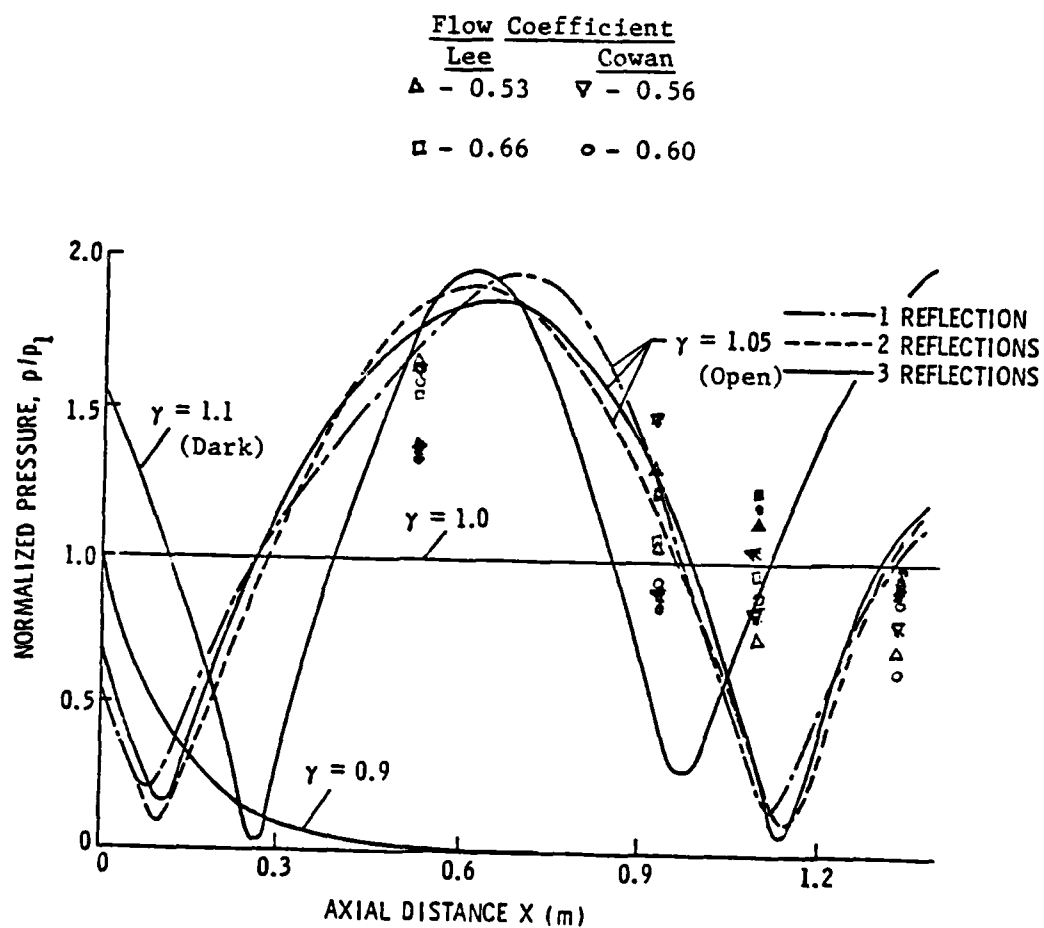


Figure 41. Predicted and Measured (1,0) Mode Steady State Waveform

standing waveforms, shown in Figure 42. Since the closest microphone position to the rotor was near the center of the region of the inlet to the rotor, half of a wave is expected to exist in the microphone region. This is precisely what can be traced from the data points, as can be seen in the plots. Therefore, the standing wave pressure pattern theorized seems by all indications to exist at this frequency. Similar pressure patterns exist for the frequency at which the second overtone of the standing wave for the (1,0) mode occurs. However, as is stated above, more extensive measurements must be performed in order to have a complete understanding of the pressure pattern in the duct.

3.3.5 Coupling of Unsteady Lift Force to Acoustic Modal Pressures

Lee wrote a computer program to couple the unsteady lift force to the acoustic modal pressure through the use of Equation (22). He compared his results with results from the theories of Shen and Smith and found discrepancies, especially around standing wave frequencies. Figures 43 and 44 show comparisons between predictions made with the lift data of this investigation using Lee's prediction program and lift data taken here and by Lee. The levels measured here are generally within 5 dB lower than those taken by Lee and within 10 dB lower than predicted levels. What Lee did not realize was that \tilde{C}_L increases and reductions could be accounted for and his prediction model seems to be valid.

The factor which caused results to differ from expected values is that the AFRF design did not conform to the assumptions of the

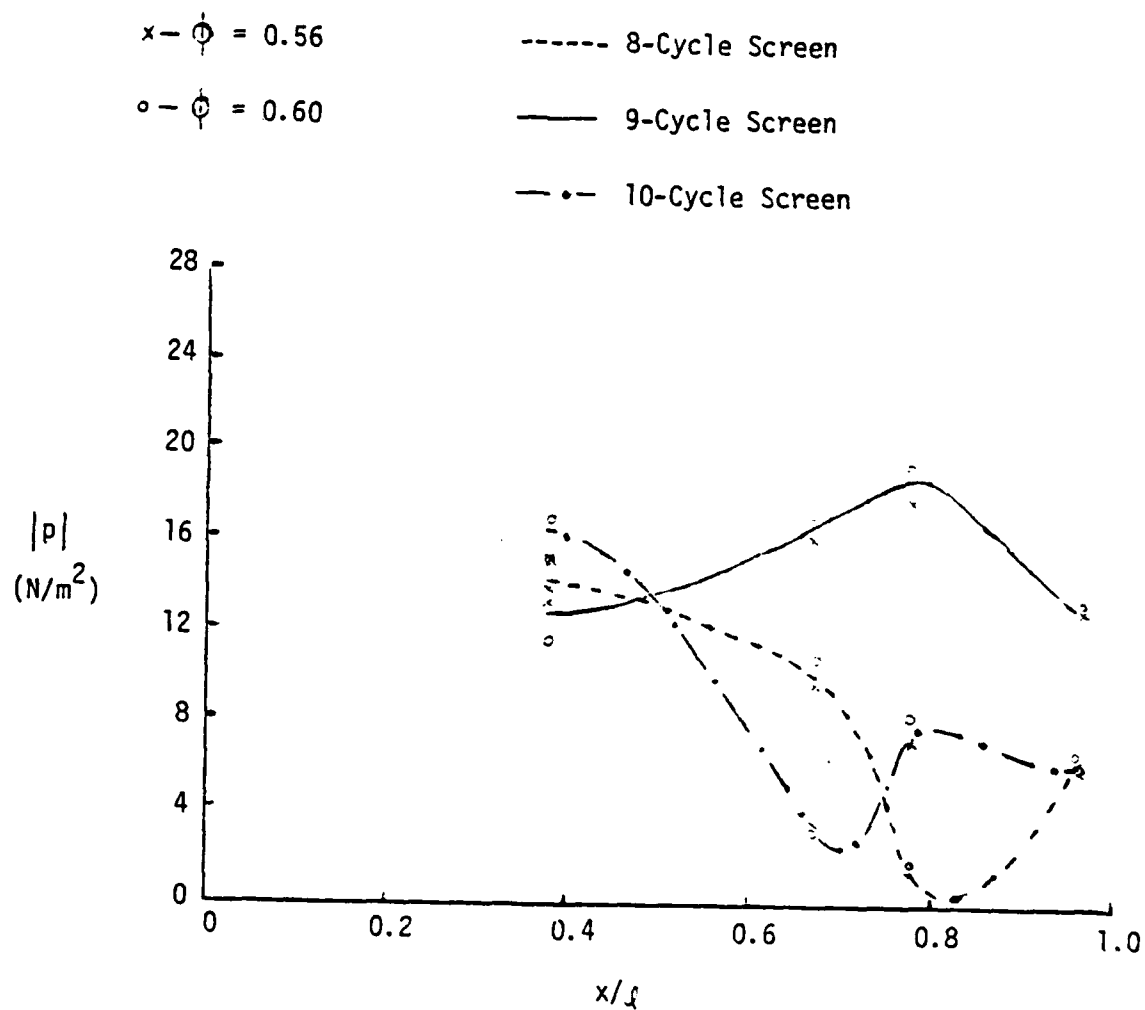


Figure 42. Measured SPL Waveforms at the (0,0) Mode Second Overtone Standing Wave Frequency

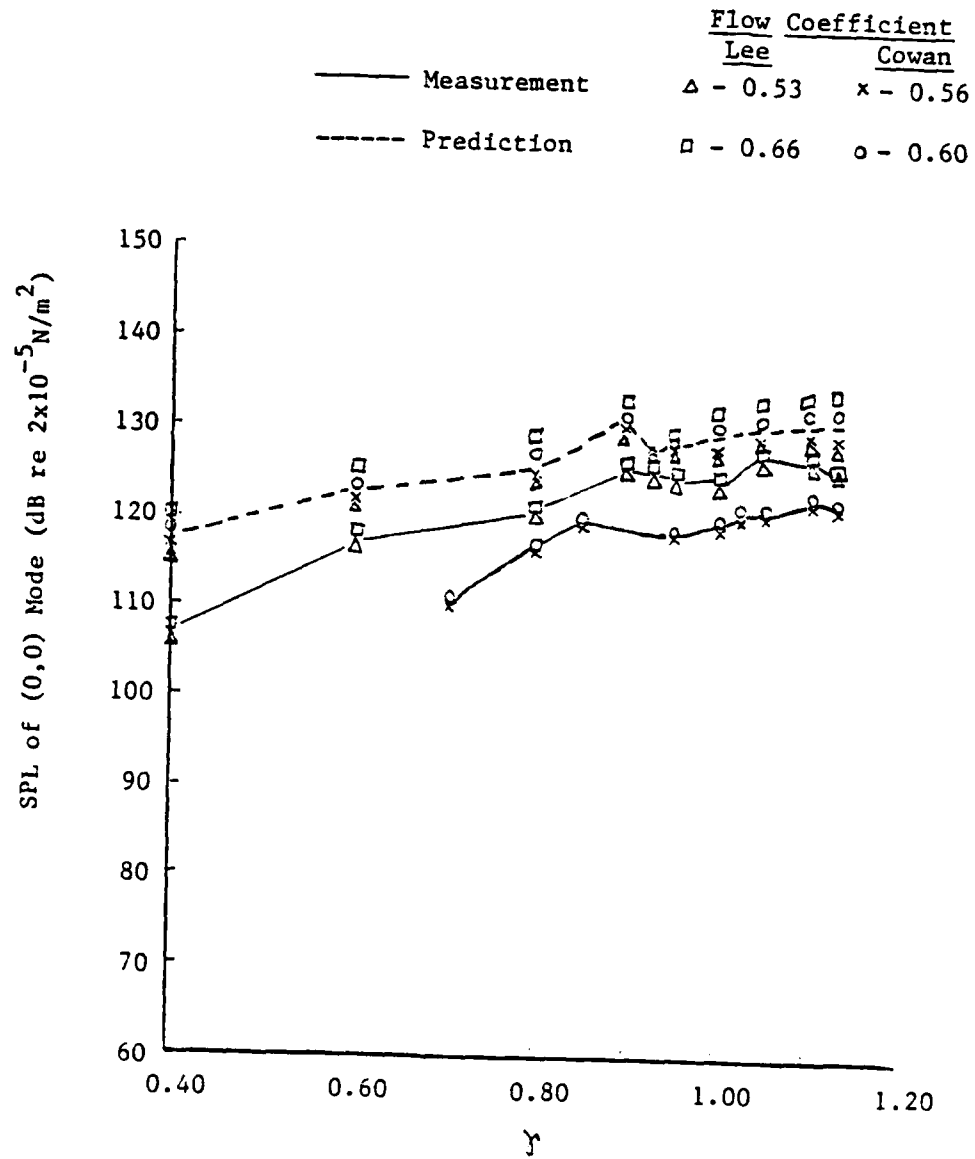


Figure 43. SPL of (0,0) Mode versus (1,0) Mode Cut-Off Ratio from 9-Cycle Screen Measurement

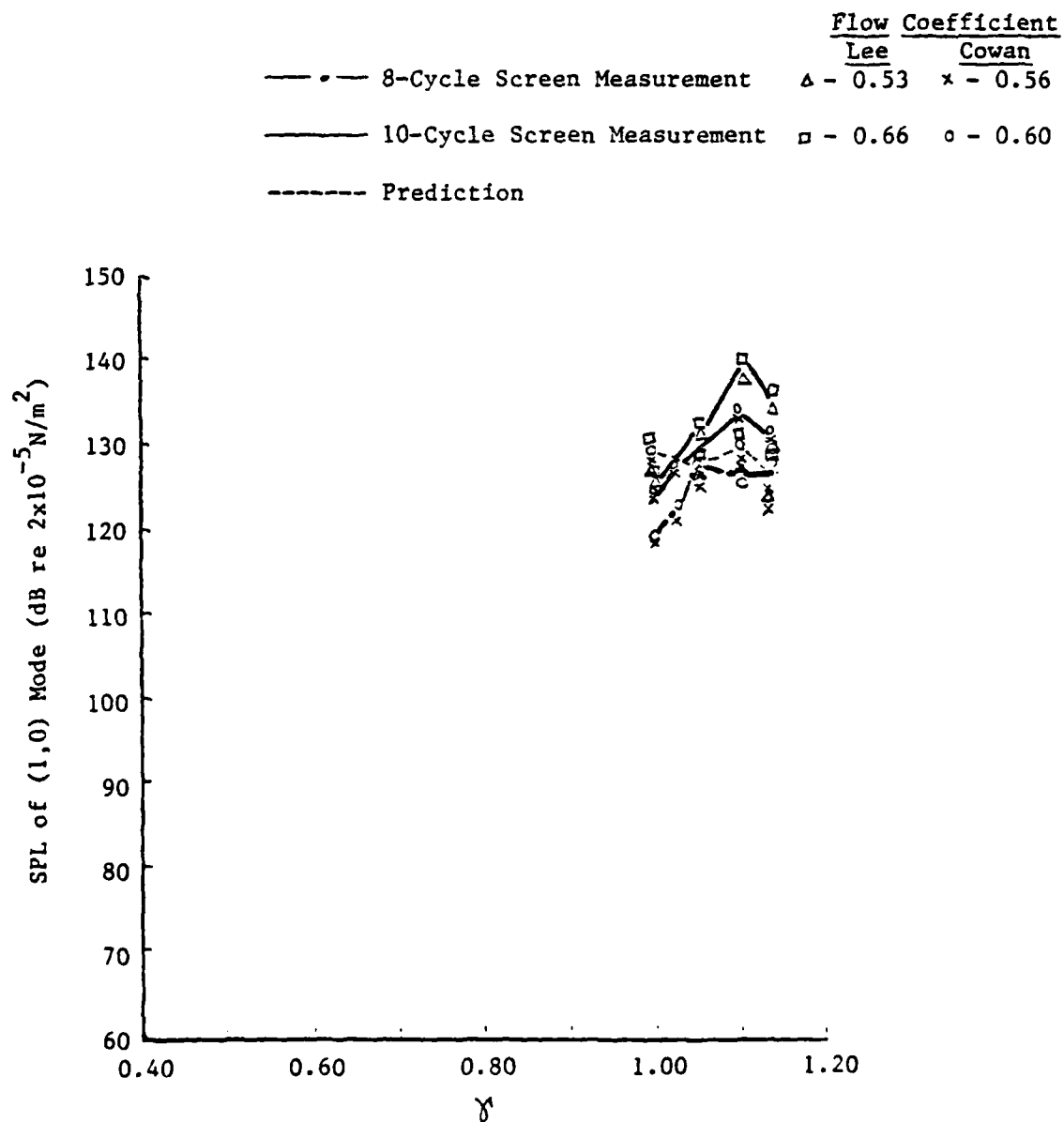


Figure 44. SPL of (1,0) Mode versus (1,0) Mode Cut-Off Ratio from 8- and 10-Cycle Screen Measurement

prediction model. The unsteady lift data which was input had a reduction from standing wave back-reaction effects that were carried through the analysis. Therefore, if the duct geometry were changed to rule out the possibility of standing wave generation over a prescribed BPF range, results should conform with prediction very well. If a more detailed experimental description of the back-reaction due to standing waves is desired, many more rotor speeds than were studied should be considered, especially in the vicinity of the standing wave frequencies.

In order to more fully understand the standing wave and general acoustic pressure wave propagation in the duct, impedance data must be acquired at the boundaries. This would result in accurate reflection coefficient data and nearly exact noise predictions would be able to be made. One restraint in the investigation of the entire coupling scheme between unsteady lift force and acoustic pressure is the near field of the rotor. The coupling must be described in terms of unsteady lift forces on the blades generating a certain far-field acoustic pressure. Turbulent mixing causes problems in making reliable acoustic measurements in this region.

The back-reaction and resultant unsteady lift decreases observed in this investigation raise interesting questions for application elsewhere. For instance, if a ducted ventilating system had its fan flow generator running at a standing wave frequency, the unsteady lift force on the fan blades would decrease, while simultaneously, a pressure node at the duct vent would cause minimal noise levels to be radiated at BPF. This is merely a proposal and efficiency studies would have to be performed to check the practicality

and feasibility of this idea, but acoustical back-reaction may prove to be a powerful tool.

Therefore, Lee's coupling scheme seems valid and it can be said that there is a definite proportionality between unsteady lift force on the rotor blades and on acoustic modal pressure in a duct. Cutting down on unsteady lift force should lower noise levels. As far as an actual coupling factor is concerned, each mode appears to have its own coupling factor dependent upon the duct geometry. Measurement of this factor would require extensive acoustical measurements under ideal modal isolation conditions. It can be reasonably concluded from this work, though, that there is a definite coupling between the two physical entities.

CHAPTER IV

SUMMARY, CONCLUSIONS, AND RECOMMENDATIONS

FOR FURTHER RESEARCH

4.1 Summary and Conclusions

In this investigation, flow velocity surveys, unsteady lift forces on a blade of a rotor, and acoustic modal pressures were measured to afford a better understanding of fan and compressor noise generating mechanisms. Through the use of flow distortion screens, the (0,0) order plane wave and (1,0) and (-1,0) first higher order spinning wave modes were generated upon flow interaction with a nine-bladed rotor. The signal-to-noise ratio was sufficient for unsteady lift and acoustic pressure measurements and, thus, the AFRF is a suitable apparatus for conducting acoustic modal pressure studies.

A distortion screen was designed, built, and tested to produce $\pm 20\%$ maximum variation from the mean flow velocity in sinusoidal flow velocity profiles. Two previously constructed screens were also tested. Adequate agreement was found between theoretical predictions for screen design and experimental measurement for the test purposes. The previously designed screens showed changes in test results due to wear, but they were still adequate for this experiment.

Using a phase-locked ensemble averaging technique, the magnitude and phase angle of unsteady lift force and acoustic pressure were measured simultaneously with good repeatability.

Based on the results obtained in this study, the following conclusions can be made:

- (1) The unsteady lift gage in the instrumented rotor blade was calibrated both statically and dynamically. The static calibration was found to be valid for the investigation since the dynamic calibration revealed a flat response from DC to the maximum frequency of interest.
- (2) Agreement between harmonic level and spectral level acoustic pressure data showed good modal isolation.
- (3) A cut-off phenomenon was observed for the $(-1,0)$ and $(1,0)$ modes conforming to theory.
- (4) Standing waves were set up in the duct between the rotor and the bellmouth inlet at certain frequencies which were theoretically predicted herein. Data indicates that these standing waves may have caused either an increase or a reduction in unsteady lift force and an unsteady lift phase shift from predicted levels which may be explained in terms of an acoustic pressure mode back-reaction.
- (5) Unsteady lift and acoustic pressure data varied only slightly over the range of flow coefficients observed but, in general, unsteady lift increased with steady lift.
- (6) Unsteady lift and acoustic pressure levels were lower than those predicted and those previously recorded.
- (7) Lee's modal coupling scheme would seem to be valid without standing wave back-reaction behavior.

- (8) There is a definite coupling between unsteady lift force and acoustic modal pressure, yet experimental measurement of a coupling factor would require much more extensive work than has been done here.

4.2 Recommendations for Further Research

Recommendations for further work on this study are:

- (1) In order to obtain a clear, complete picture of the back-reaction effect of the standing waves, more lift and acoustic data points should be taken in the vicinity of standing wave BPF's.
- (2) The duct geometry should be changed to ensure that the standing wave frequency and cut-off frequency are sufficiently separated to study separately the possibility of respective back-reactions.
- (3) The impedance at the duct inlet and rotor should be measured to obtain reflection coefficients in order to describe better the modal pressure patterns.
- (4) A study should be conducted to find out why unsteady lift and acoustic pressure levels were generally lower in this study than those observed by Lee on the same apparatus.
- (5) Taking data at many more microphone positions along the duct, both radial and circumferential, is necessary to provide a detailed picture of the pressure field in the duct.

- (6) An experiment should be conducted with a duct designed to have no standing wave effects present in the frequency range of interest to prove that Lee's theoretical predictions hold true when these effects are not present.
- (7) Rotor near-field measurements should be attempted for a certain isolated mode to measure a definite coupling factor between unsteady lift force and acoustic pressure.
- (8) Standing wave back-reaction behavior should be studied in the view of noise control for ducted ventilating systems.
- (9) In-duct measurements should be performed simultaneously with far-field acoustic measurements to verify existing theories of acoustic radiation.

REFERENCES

1. Kemp, N. H., and Sears, W. R. The Unsteady Forces Due to Viscous Wakes in Turbomachines. Journal of the Aeronautical Sciences, 1955, 22(7), 478-483.
2. Horlock, J. H. Fluctuating Life Forces on Aerofoils Moving Through Transverse and Chordwise Gusts. Journal of Basic Engineering, 1968, 90D(4), 494-500.
3. Whitehead, D. S. Force and Moment Coefficients for Vibrating Aerofoils in Cascade. Aeronautical Research Council R and M 3254, February 1960.
4. Whitehead, D. S. Bending Flutter of Unstalled Cascade Blades at Finite Deflection. Aeronautical Research Council R and M 3386, October 1962.
5. Henderson, R. E., and Daneshyar, H. Theoretical Analysis of Fluctuating Lift on the Rotor of an Axial Turbomachine. Aeronautical Research Council R and M 3684, September 1970.
6. Smith, S. N. Discrete Frequency Sound Generation in Axial Flow Turbomachines. Aeronautical Research Council R and M 3709, March 1972.
7. Kaji, S., and Okazaki, T. Generation of Sound by Rotor-Stator Interaction. Journal of Sound and Vibration, 1970, 13(3), 281-307.
8. Mani, R. Discrete Frequency Noise Generation from an Axial Flow Fan Blade Row. Journal of Basic Engineering, ASME Transactions, March 1970, 92D, 37-43.
9. Osborne, C. Unsteady Thin-Airfoil Theory for Subsonic Flow. AIAA Journal, February 1973, 11(2), 205-209.
10. Tyler, J. M., and Sofrin, T. G. Axial Flow Compressor Noise Studies. SAE Transactions, 1962, 70, 309-332.
11. Morfey, C. L. Rotating Pressure Patterns in Ducts: Their Generation and Transmission. Journal of Sound and Vibration, 1964, 1, 60-87.
12. Bruce, E. P. Axial Flow Rotor Unsteady Performance. Ph.D. Thesis in Aerospace Engineering, The Pennsylvania State University, 1979.

13. Satyanarayana, B., Henderson, R. E., and Gostelow, J. P. A Comparison Between Experimental and Theoretical Fluctuating Lift on Cascades at Low Frequency Harmonics. ASME Gas Turbine Conference, Paper No. 74-GT-78. Zurich, Switzerland, 1974.
14. Gallus, H. E., Lambertz, J., and Wallman, T. Blade-Row Interaction in an Axial Flow Subsonic Compressor Stage. ASME Gas Turbine Conference, Paper No. 79-GT-92. San Diego, California, 1979.
15. Sharland, I. J. Sources of Noise in Axial Flow Fans. Journal of Sound and Vibration, 1964, 1(3), 302-322.
16. Bragg, S. L., and Bridge, R. Noise from Turbojet Compressors. Journal of the Royal Aeronautical Society, January 1964, 68, (637), 1-10.
17. Lowson, M. V. Theoretical Studies of Compressor Noise. NASA, CR-1287, March 1969.
18. Benzakein, M. J. Research on Fan Noise Generation. Journal of the Acoustical Society of America, May 1972, 51(5)-1, 1427-1438.
19. Lipstein, N. J., and Mani, R. Experimental Investigation of Discrete Frequency Noise Generated by Unsteady Blade Forces. Journal of Basic Engineering, ASME Transactions, March 1970, 155-164.
20. Harel, P., and Perulli, M. Measurement in a Duct of the Space-Structure of the Discrete Frequency Noise Generated by an Axial Compressor. Journal of Sound and Vibration, 1972, 23(4), 487-506.
21. Moore, C. J. Measurement of Radial and Circumferential Modes in Annular and Circular Fan Ducts. Journal of Sound and Vibration, 1979, 62(2), 235-256.
22. Doak, P. E. Some Comments on Possible Back-Reaction Effects of Acoustic Fields on Aerodynamic Sound Sources. NASA SP-207, 1969, 469-472.
23. Lee, C. S. Coupling of Unsteady Lift to Acoustic Duct Modes in an Axial Flow Fan. M.S. Thesis in Mechanical Engineering, The Pennsylvania State University, 1980.
24. Archibald, F. S. Self-Excitation of an Acoustic Resonance by Vortex Shedding. Journal of Sound and Vibration, 1975, 38(1), 81-103.

25. Archibald, F. S. The Laminar Boundary Layer Instability Excitation of an Acoustic Resonance. Journal of Sound and Vibration, 1975, 38(3), 387-402.
26. Crow, S. C., and Champagne, F. H. Orderly Structure in Jet Turbulence. Journal of Fluid Mechanics, 1971, 48(3), 547-591.
27. Morfey, C. L. Rotating Blades and Aerodynamic Sound. Journal of Sound and Vibration, 1973, 28(3), 587-617.
28. Cumpsty, N. A. REVIEW - A Critical Review of Turbomachinery Noise. Journal of Fluids Engineering, ASME Transactions, 1977, 278-293.
29. Bruce, E. P. The ARL Axial Flow Research Fan - A New Facility for Investigation of Time-Dependent Turbomachinery Flows. ASME Joint Fluids and CSME Conference, Paper No. 74-FE-27. Montreal, Quebec, Canada, 1974.
30. Fitzgerald, J. M., and Marboe, R. C. The ARL/FED Anechoic Chamber. Applied Research Laboratory, The Pennsylvania State University, ARL TM 81-164, August 1981.
31. Amiet, R. K. Transmission and Reflection of Sound by a Blade Row. AIAA 9th Aerospace Sciences Meeting, Paper No. 71-181, New York, New York, 1971.
32. Davies, P. O. A. L., Coelho, J. L. B., and Bhattacharya, M. Reflection Coefficients for an Unflanged Pipe with Flow. Journal of Sound and Vibration, 1980, 72(4), 543-546.
33. Shen, I. C. Unsteady Pressure Distributions on Airfoils in Cascade. M.S. Thesis in Mechanical Engineering, The Pennsylvania State University, 1980.
34. Shapiro, A. H. The Dynamics and Thermodynamics of Compressible Fluid Flow, Vol. I. New York: The Ronald Press Company, 1953.
35. Bruce, E. P. Design and Evaluation of Screens to Produce Multi-Cycle $\pm 20\%$ Amplitude Sinusoidal Velocity Profiles. AIAA 8th Aerodynamic Testing Conference, Paper No. 74-623. Bethesda, Maryland, 1974.
36. McCarthy, J. H. Steady Flow Past Non-Uniform Wire Grids. Journal of Fluid Mechanics, 1964, 19, 491-512.
37. Lieblein, S. Experimental Flow in Two-Dimensional Cascades. NASA, SP-36, 1965, 183-226.

APPENDIX A

DISTORTION SCREEN DESIGN

Tyler and Sofrin [10] stated that the circumferential order of an acoustic duct mode generated by rotor-stator interaction can be expressed as:

$$m = nB + kV ,$$

where

B = number of rotor blades,

V = number of stator blades or circumferential distortion wakes of the inlet flow,

n = BPF harmonic number, and

k = an integer (... , -1, 0, 1, ...)

Since a nine-bladed rotor was used in this study, the above equation indicates that the plane wave (0,0) mode and the first higher order co-rotational (1,0) and counter-rotational (-1,0) modes can be generated by 9-, 8-, and 10-cycle circumferential distortions, respectively.

8-, 9-, and 10-cycle distortion screens were used in this experiment. The 9- and 10-cycle screens were fabricated by Bruce and Lee, respectively, and the 8-cycle screen was designed and constructed for this work. They were designed to produce circumferentially sinusoidal velocity flow profiles with $\pm 20\%$ variation from the mean axial velocity, \bar{V}_x . Flow interactions with typical wakes of stator blades introduce many velocity distortion

harmonics. However, by using sinusoidal distortion patterns, the experiment is much easier to perform. By Fourier analysis, sine waves can be combined to describe the more complicated waveforms encountered in the practical world by superposition. A 20% \bar{V}_x variation was found [35] to be appropriate for harmonic isolation and for application of linearized theories for predicting rotor response.

Bruce [35] described the screen design in detail. Using McCarthy's single overlay technique [36], screen segments with different flow coefficients were laid onto a background support screen to approach the intended sinusoidal flow resistance variation. Ideally, a large number of screen segments, each of infinitesimal thickness, would have to be adjacently mounted to achieve the sinusoidal velocity profile desired. Due to the limited types of screening available and the brittle nature of the screen material, two steps of resistance coefficient, K , changes were chosen in designing the 8-cycle screen. Figure A1 shows the theoretical and designed 8-cycle screen characteristics for one distortion cycle, and Figure A2 shows the actual screen. The lowest level of the resistance coefficient, K_{\min} , corresponds to the K of the support screen, which is 0.343 for the 8-cycle screen. Figures A3 and A4 show the theoretical and design characteristics for one cycle of the 9- and 10-cycle screens respectively.

Results of the velocity surveys shown in Chapters II and III prove that the limitations of design were appropriate to set the intended conditions to within 5% of the fundamental harmonic level. Results of the overall work show strong modal isolation and thus distortion screen design limitations did not handicap the desired flow characteristics.

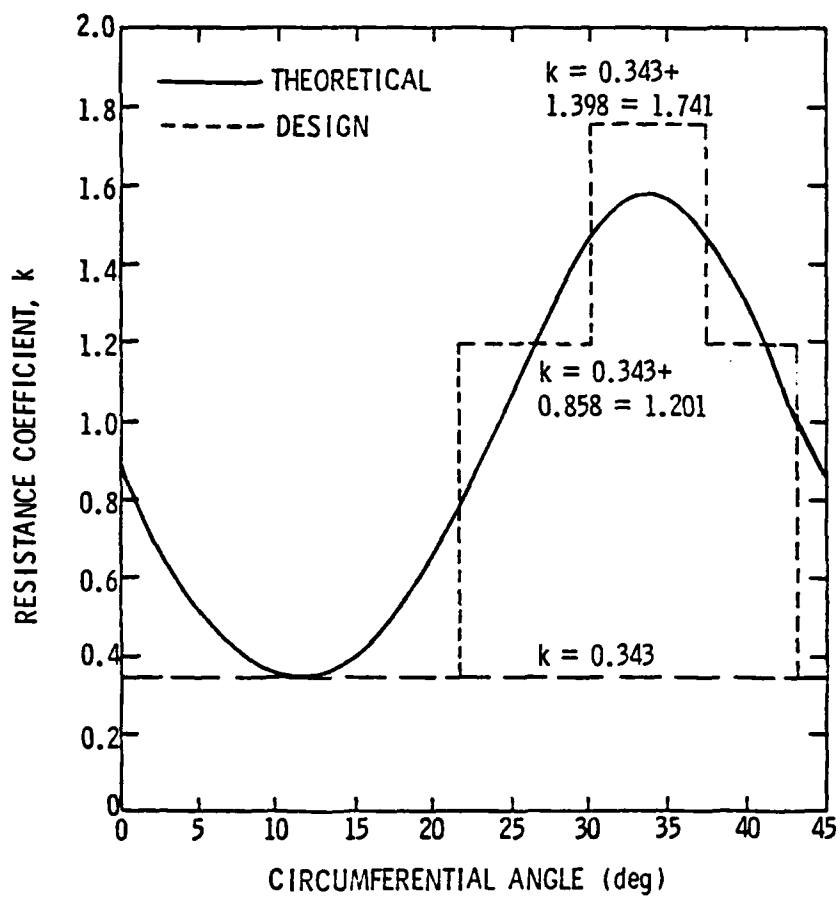


Figure A1. Theoretical and Designed Resistance Coefficient Variation for the 8-Cycle Distortion Screen

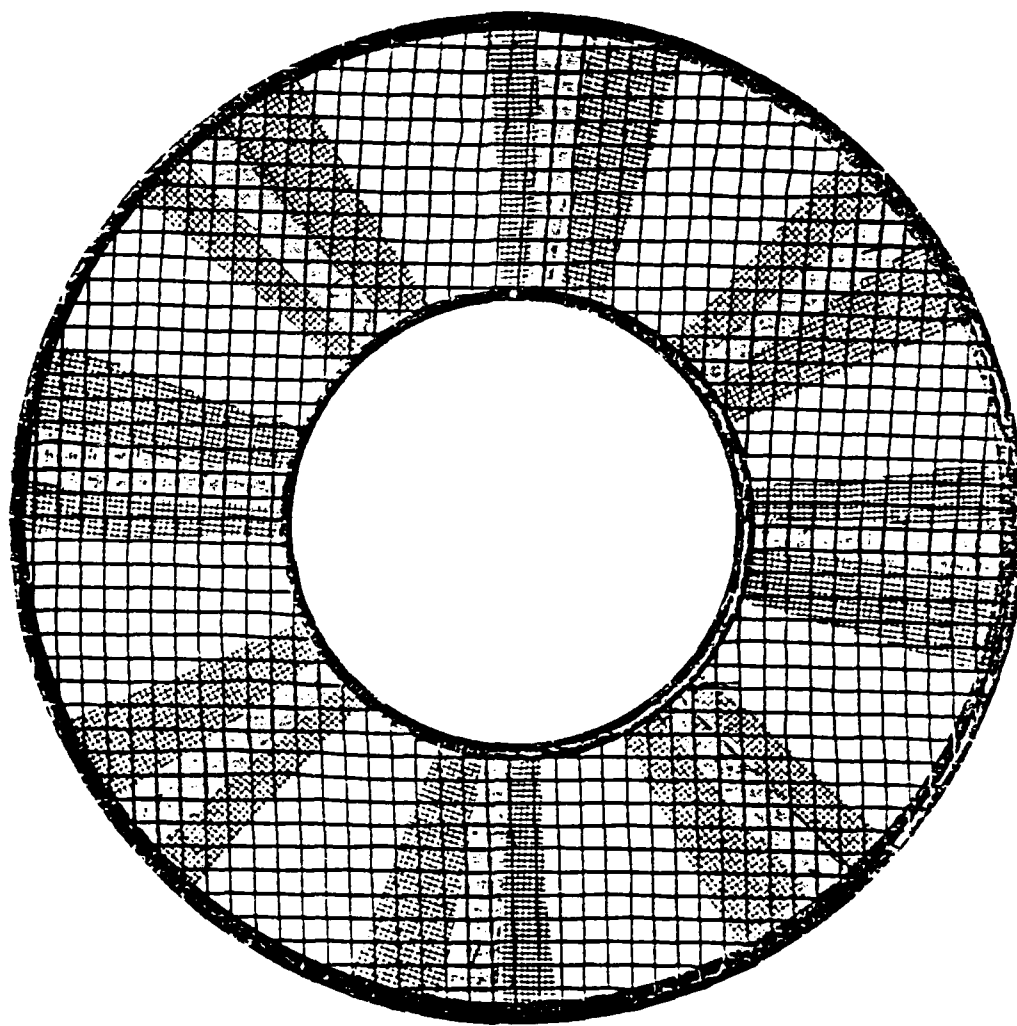


Figure A2. The 8-Cycle Distortion Screen

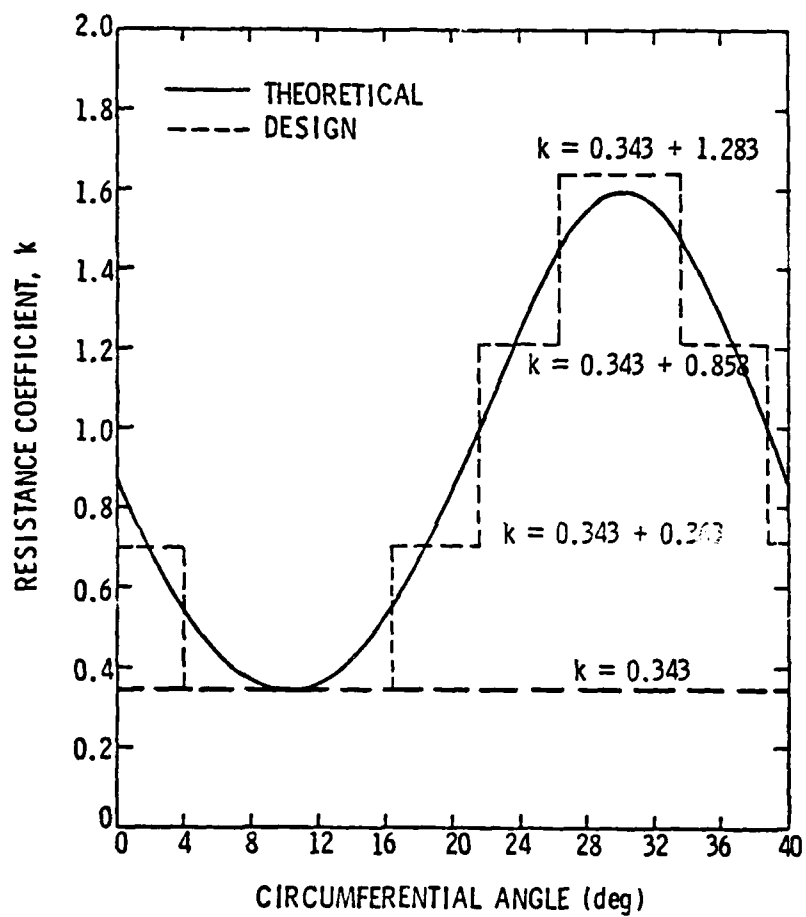


Figure A3. Theoretical and Designed Resistance Coefficient Variation for the 9-Cycle Distortion Screen [35]

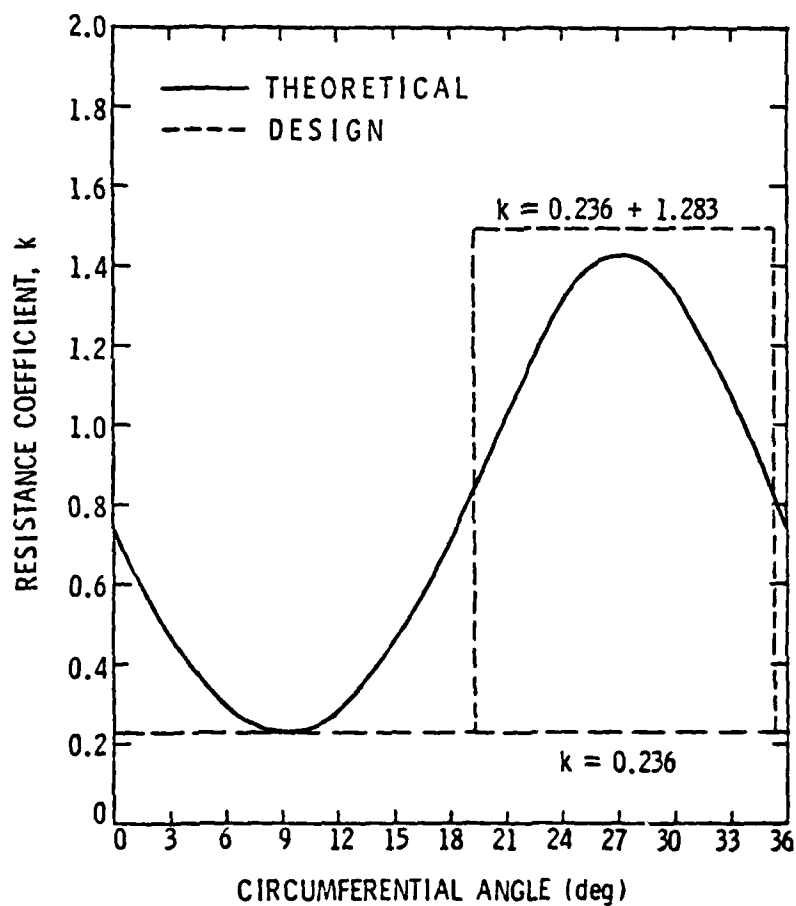


Figure A4. Theoretical and Designed Resistance Coefficient Variation for the 10-Cycle Distortion Screen [23]

APPENDIX B

DYNAMIC LIFT GAGE CALIBRATION

Dynamic calibration of the lift gage was necessary due to the blade mechanical resonance effects. A static calibration was performed by varying the masses loaded on the instrumented blade (this setup is shown in Figure B1). Static lift gage calibration can be used for dynamic measurements only if the response is flat from DC to the maximum frequency of interest.

Looking at Figure 9, it appears that a resonance peak occurs at around 500 Hz. This was confirmed by the dynamic calibration which is described below.

A small electrodynamic shaker was used originally in the setup shown in Figure B2. The frequency was varied, using a frequency counter, with a constant force applied to the blade and the voltage output on an oscilloscope showed a resonance frequency at approximately 380 Hz. The three force levels used were comparable to the lowest, middle, and highest forces encountered by the blades in the actual experiment; i.e., at 742 rpm, the lowest speed, the blade force was approximately 0.09 N, and at 2100 rpm, the highest speed, the blade force was approximately 0.93 N. The three forces used were 0.22 N, 0.44 N, and 0.89 N. Since this disagreed with Figure 9, it was assumed that the mass of the entire system (blade, shaker, etc.) caused the decrease in resonance frequency value.

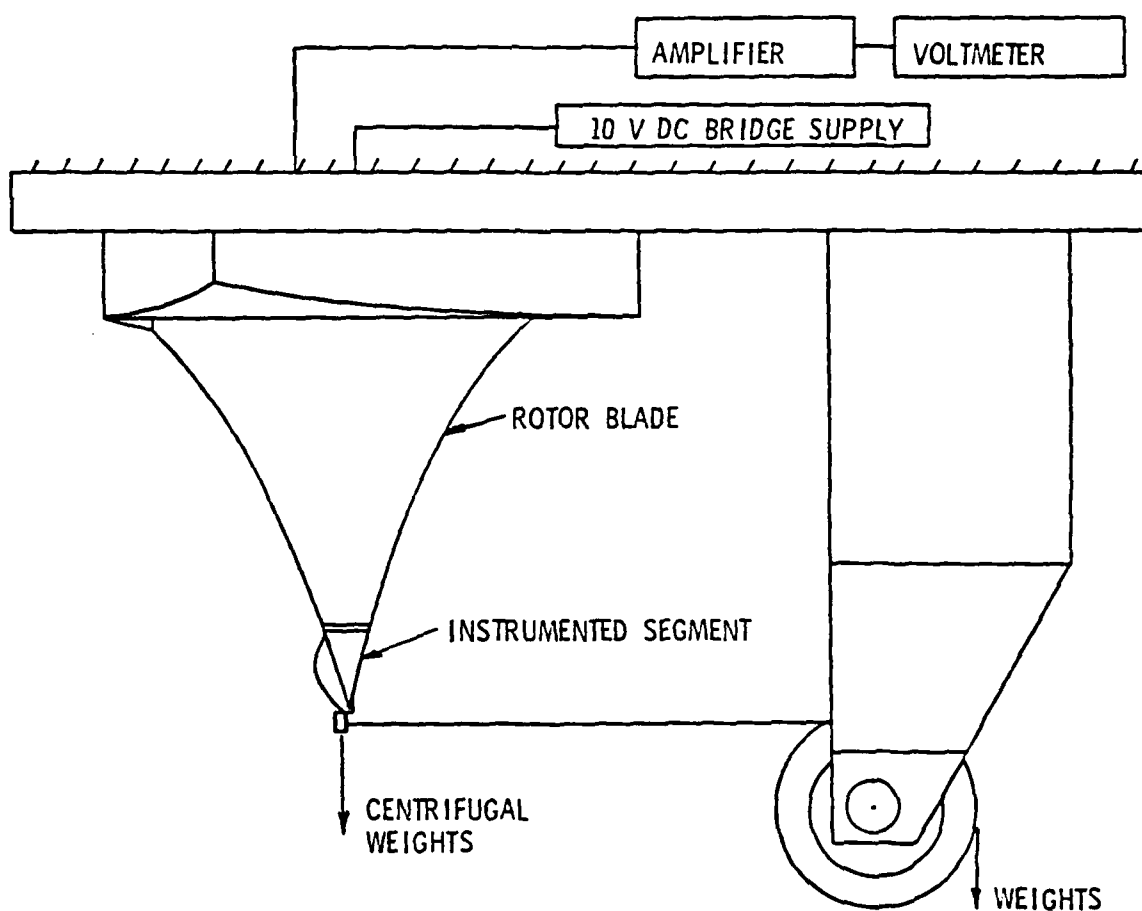


Figure B1. Instrumentation Setup for Static Calibration of the Lift Gage

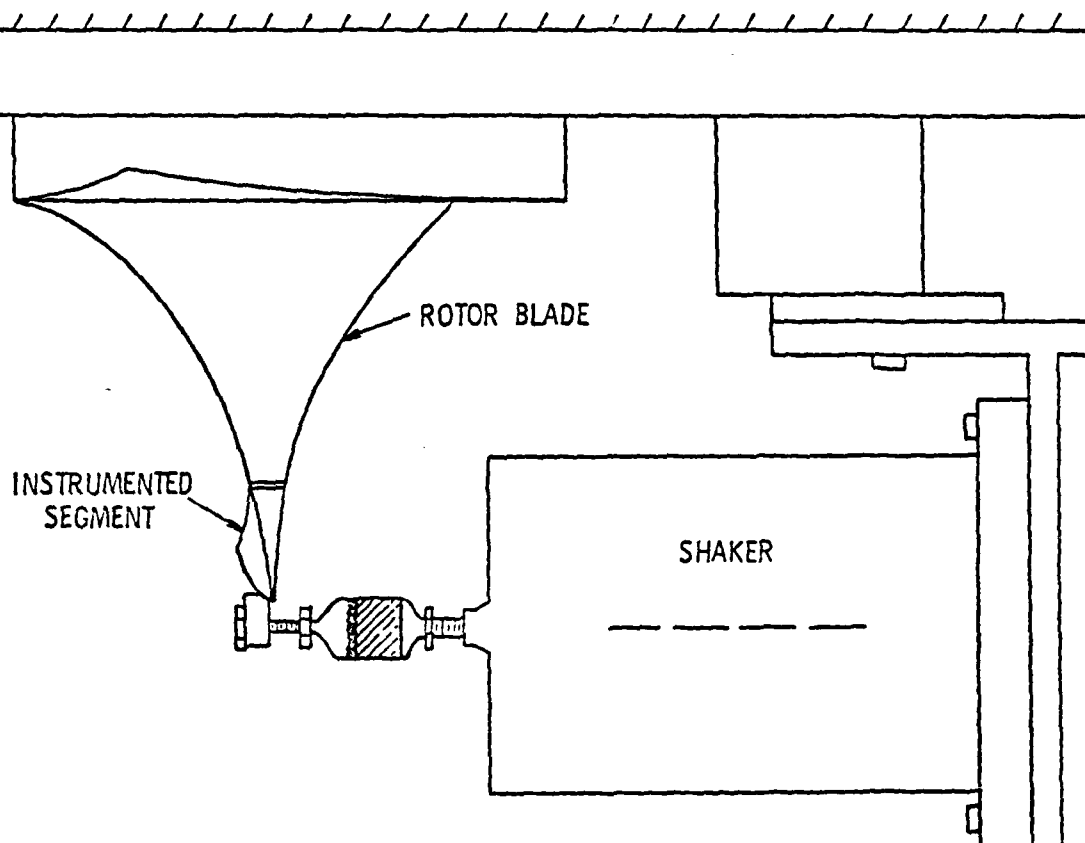


Figure B2. Setup for Dynamic Lift Gage Calibration Using a Small Shaker

The shaker and force gage were then detached from the blade and the voltage output was observed on the oscilloscope after tapping the blade with the end of a pencil. Measuring the distance between peaks in the decaying sine wave showed the resonance frequency as being around 500 Hz, which indicated that the shaker assembly was responsible for the difference. Another confirmation that the added mass lowered the resonance frequency of the system was the measurement of a resonance frequency of approximately 450 Hz when a 7-gram accelerometer was attached to the blade and tapped as was done previously.

Since the interest here was in the instrumented segment of the blade itself, yet another method to show that resonance occurred at around 500 Hz was necessary. It was decided to mount the blade on a large shaker so that the resonance of the shaker would be substantially different from that of the blade due to the large mass difference (see Figure B3 for the setup). Observing the voltage output on the oscilloscope screen, resonance occurred at around 350 Hz when the tip piece of the blade was not attached. When the tip piece was attached, resonance seemed to occur at approximately 475 Hz. In order to take readings at the same three constant force levels that were used with the smaller shaker, a seismic acceleration technique was utilized. By this technique, a 7-gram accelerometer (the same as used before) was attached to the blade and hooked up to the oscilloscope. Since the mass of the system is constant, the force applied to the blade will be constant if the acceleration can be held constant.

Because the acceleration is proportional to the displacement by a factor of $-\omega^2$, ω being angular frequency, the display on the

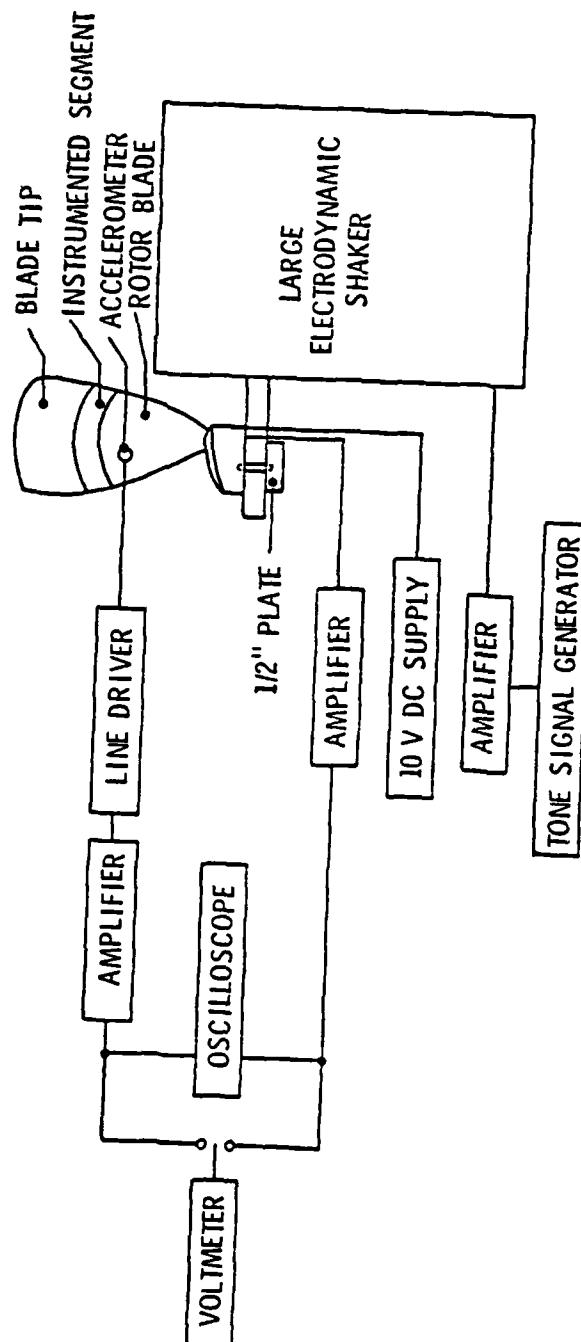


Figure B3. Instrumentation Setup for Dynamic Lift Gage Calibration Using a Large Shaker

oscilloscope can be thought of as a displacement plot. Therefore, if the amplitude of the signal from the accelerometer is held constant, the acceleration and, thus, the force applied to the blade is held constant.

To set the force at the same values as those used with the small shaker, the voltage output at 100 Hz (well below resonance) was used to set the acceleration level when using the large shaker. Frequency was varied and acceleration amplitude was kept constant. The results are presented in Figure B4. The data is fairly linear with increases in applied force and resonance is shown by the peaks at 510 Hz. It can be seen in the plots of Figure B4 that the response is relatively flat up to 400 Hz.

Therefore, the resonance frequency is around 500 Hz as indicated in Figure 9 and the static calibration data can be reliably used for the data reduction since the response is flat through the frequency range of interest.

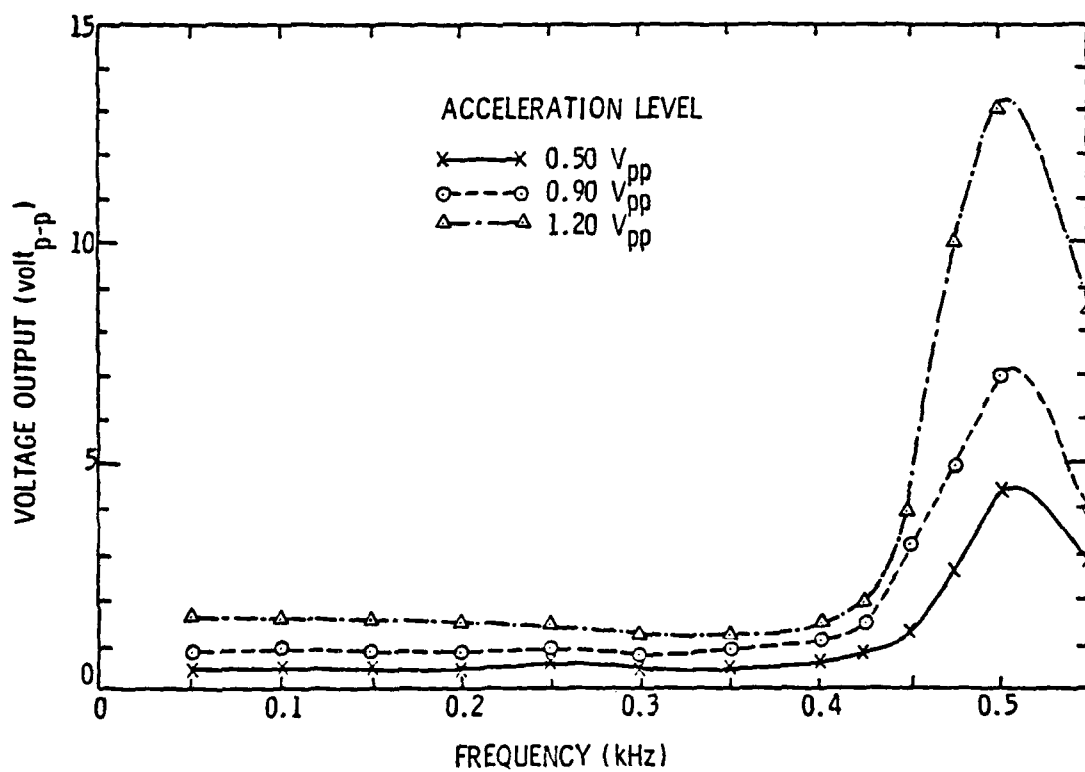


Figure B4. Dynamic Response of the Lift Gage from the Large Shaker Calibration Technique

APPENDIX C

EFFECTS OF VARYING FLOW COEFFICIENTS

A test was performed to observe the effects of varying the flow coefficients, and thus, the flow incidence angles on the unsteady lift forces and acoustic duct pressure. The range of flow coefficients was from the ϕ corresponding to blade stall ($\phi = 0.49$) to the highest ϕ the AFRF was capable of achieving ($\phi = 0.60$) in its location and environment. Five ϕ values were observed.

The rotor blade stall limit was defined by Lieblein [37] in terms of a diffusion factor, D , which is expressed as:

$$D = 1 - \left[\frac{\cos \beta_i}{\cos \beta_e} \right] + \left(\frac{s}{C} \right) \left[\frac{\cos \beta_i}{2} \right] \left[\tan \beta_i - \tan \beta_e \right] , \quad (C1)$$

where

β_i = the inlet flow angle,

β_e = the rotor outlet flow angle, and

$\frac{s}{C}$ = the rotor blade space-to-chord ratio.

The unstalled condition corresponds to $D < 0.6$. Including the flow incidence angle in the β_i term and taking values at blade midspan (the location of the unsteady lift gage) from Table I, stall can be calculated (letting $D = 0.6$ and solving for β_i) to occur when $i_m = 7.91^\circ$, corresponding to $\phi = 0.49$ by velocity triangle analysis. Using this simple velocity triangle analysis technique, the incidence angles for flow coefficients of unstalled blades can be calculated. A plot of ϕ versus i_m is shown in Figure C1. On it is shown that

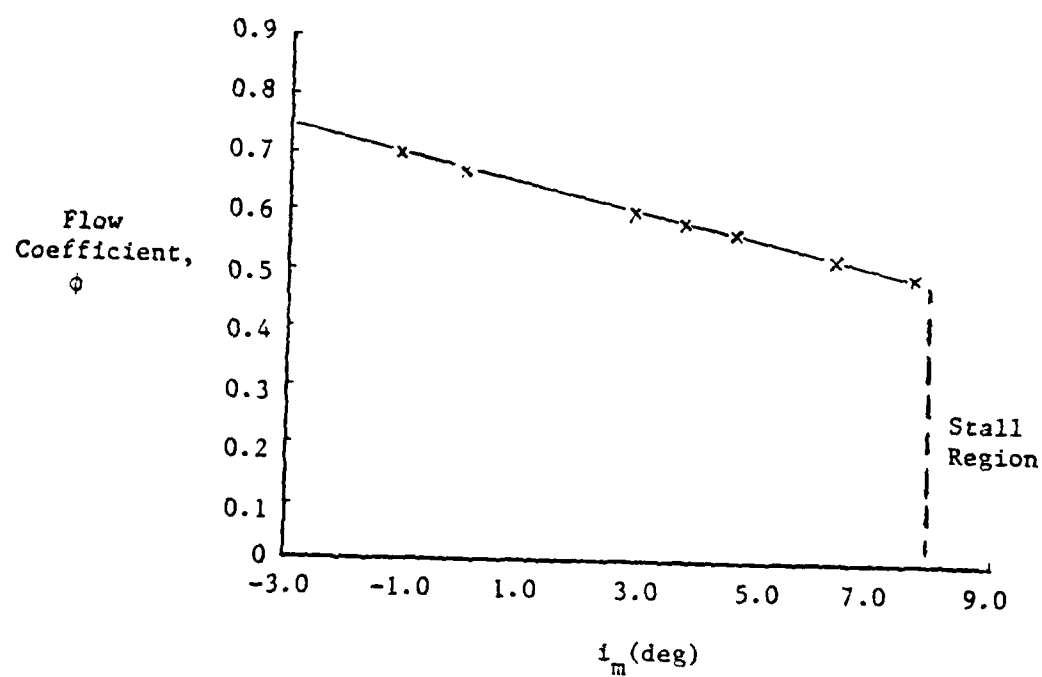


Figure C1. Flow Coefficient versus Mean Flow Incidence Angle

the ideal case of zero degree incidence corresponds to a $\phi = 0.66$. Lee had observed this case, but it could not be attained in this work due to the anechoic chamber as was previously stated.

Figure C2 shows the effect of varying the flow coefficient on the acoustic pressure at a microphone position for cut-off ratios below, at, and above the cut-off frequency for the (1,0) mode. All data here were acquired while the 10-cycle distortion screen was installed in the duct. Inspection of the phase angle data reveals that they remained fairly constant with increasing ϕ for each cut-off ratio. SPL levels show the lowest levels around stall and increasing levels with increasing flow coefficient. Readings seem to remain fairly constant to within +5 dB beginning at $\phi = 0.56$ above cut-off. In general, for all data taken in the entire experiment, acoustic measurements varied to within +5 dB between $\phi = 0.56$ and 0.60 .

Unsteady lift data behaved similarly to the acoustic pressure data. This is shown in Figure C3. The phase angles had steadily increasing variation below cut-off and remained fairly constant with increasing ϕ when the (1,0) mode was cut on. Lift magnitude measurements were generally lowest around stall and steadily increased with increasing ϕ for speeds below cut-off. Above the (1,0) mode cut-off frequency, unsteady lift levels were within +5 dB of each other starting when $\phi = 0.56$. A more extensive ϕ study with many more ϕ values being observed would better reveal the total picture of the effect of varying ϕ on lift and acoustic pressure, but the general trends observed here are sufficient for the intent of the study.

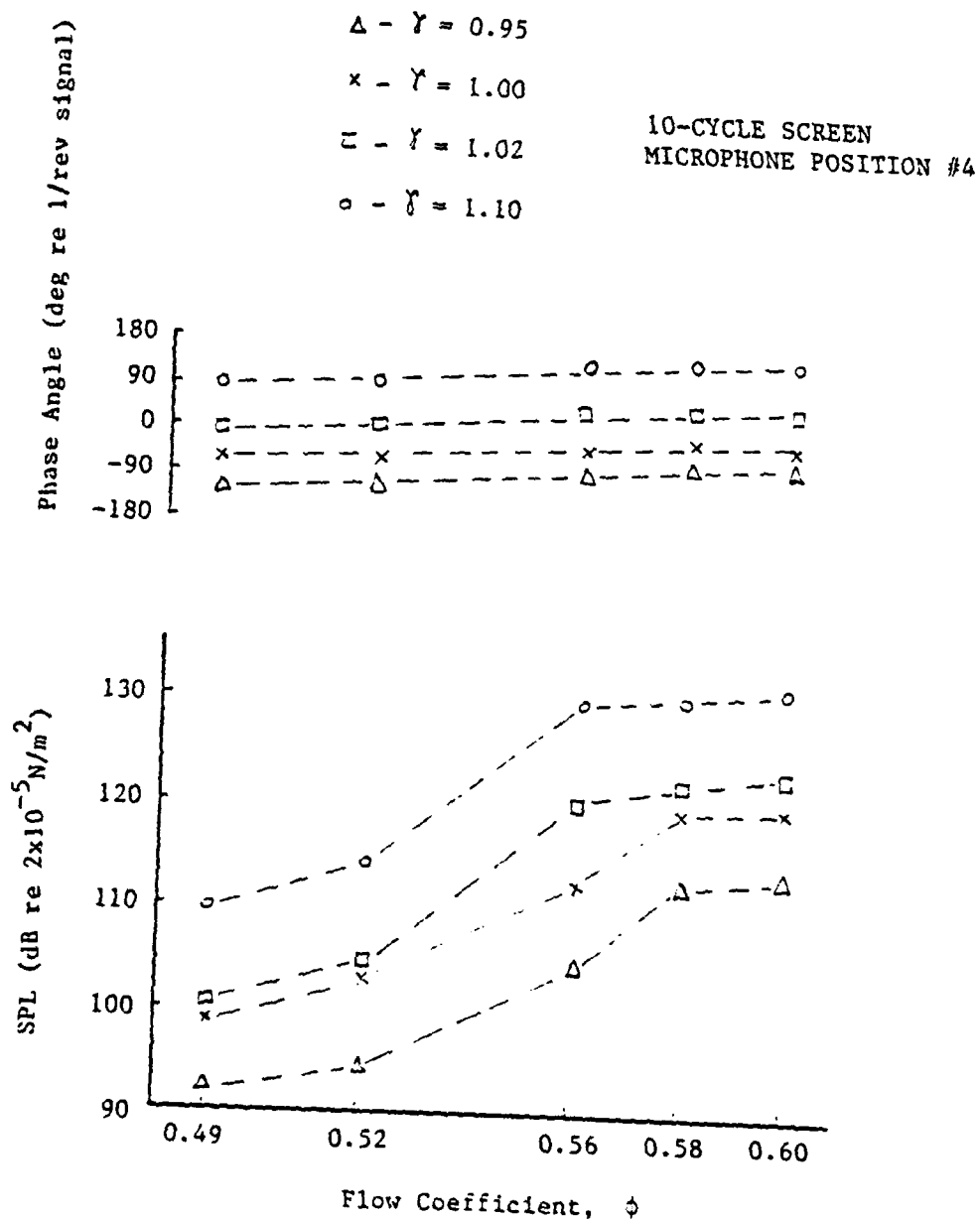


Figure C2. SPL versus Flow Coefficient

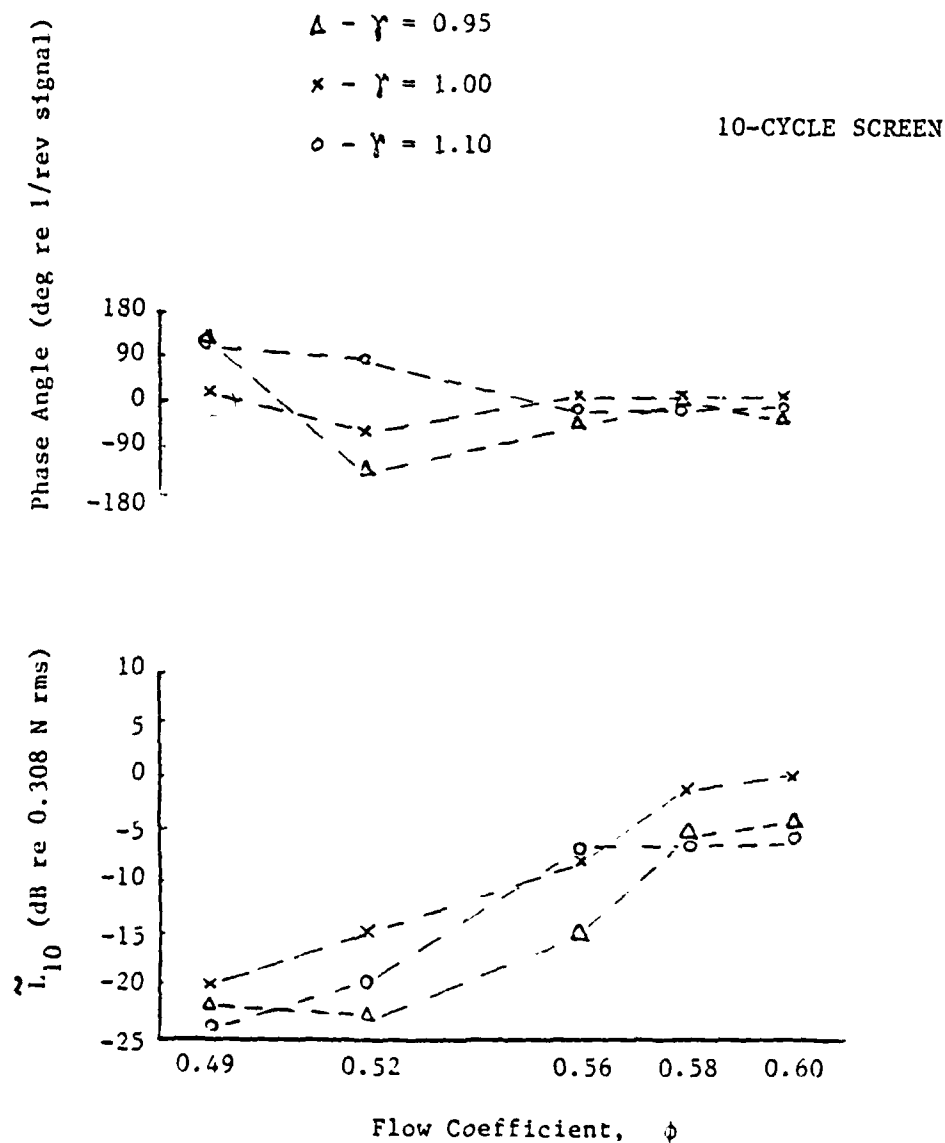


Figure C3. Unsteady Lift versus Flow Coefficient

Therefore, unsteady lift and acoustic pressure measurements behaved similarly with varying flow coefficients (and thus varying flow incidence angle) over the ϕ range studied. This is yet another factor which suggests a coupling between unsteady lift and acoustic duct pressure in an axial flow fan.

An important point to note is the small variation in unsteady lift and acoustic pressure level readings between $\phi = 0.56$ and $\phi = 0.60$, the two flow coefficients set in the main test. Since the levels are fairly close to each other for the same rotor speed, it can be said (for the purposes of this study) that the levels in this experiment are ϕ independent. Thus, levels here can be compared with those obtained by Lee with confidence.

APPENDIX D

CORRELATION OF MEASURED AND HARMONIC LEVELS

As is stated in Chapter II, unsteady lift and acoustic pressure measurements were performed using two different functions on the SD 360 analyzer. One function resulted in a spectral output of SPL versus frequency. The other resulted in a harmonic output of harmonic linear magnitude versus harmonic number. A sample of each of these plots is shown in Figures 35 and 36. For a given microphone output signal, a BPF sound pressure level in dB (re 2×10^{-5} N/m²) was recorded from the output of spectral analysis. When a corresponding microphone output signal was analyzed using harmonic analysis, a harmonic linear magnitude and amplification factor was recorded for the ninth harmonic (corresponding to the number of blades in the rotor cascade). This magnitude was then converted to a sound pressure level in dB (re 2×10^{-5} N/m²) by the relationship:

$$\text{SPL} = 20 \log \left(\frac{\text{CLM}}{676} \right) ,$$

where CLM is the corrected linear magnitude which is expressed as:

$$\text{CLM} = \text{LMD} \times 10^{A/20} \times \frac{1}{2^q} ,$$

where LMD is the linear magnitude display taken from the analyzer output, A is the attenuation level (in dB) set on the analyzer, and q is a signal amplification factor set to obtain the most accurate linear magnitude level without overloading the display.

The interaction of the flow coming from a distortion screen with the rotor cascade flow mainly excites one or two acoustic duct modes, depending on the number of distortion cycles on the screen. The evidence of this excitation is the strong (well above broadband levels) tone detected at the BPF (which is the ninth harmonic of the shaft speed). Thus, a check as to the isolation of modes by distortion screen-rotor flow interaction can be accomplished by comparing BPF and harmonic levels. Since the modes being observed in this study are assumed to be isolated by the distortion screens, this exercise can serve as a calibration for the performance of distortion screen modal isolation.

The results of this study were very good. Figure D1 shows typical results for 8-, 9-, and 10-cycle screen measurements. Spectral and harmonic measurements were within ± 2 dB of each other for all measurements and within ± 1 dB for most measurements. Also, neighboring harmonics to the ninth were within 5% of the ninth harmonic levels, illustrating sufficient modal isolation for the tests performed.

The same type of analysis was performed on the unsteady lift data (but at the harmonic number corresponding to the number of distortion screen cycles) and similar results to the acoustic pressure measurements were found, as can be seen from the plots in Figure D2. These comparisons do not have any modal significance, though. They merely confirm the validity of the spectral lift measurements.

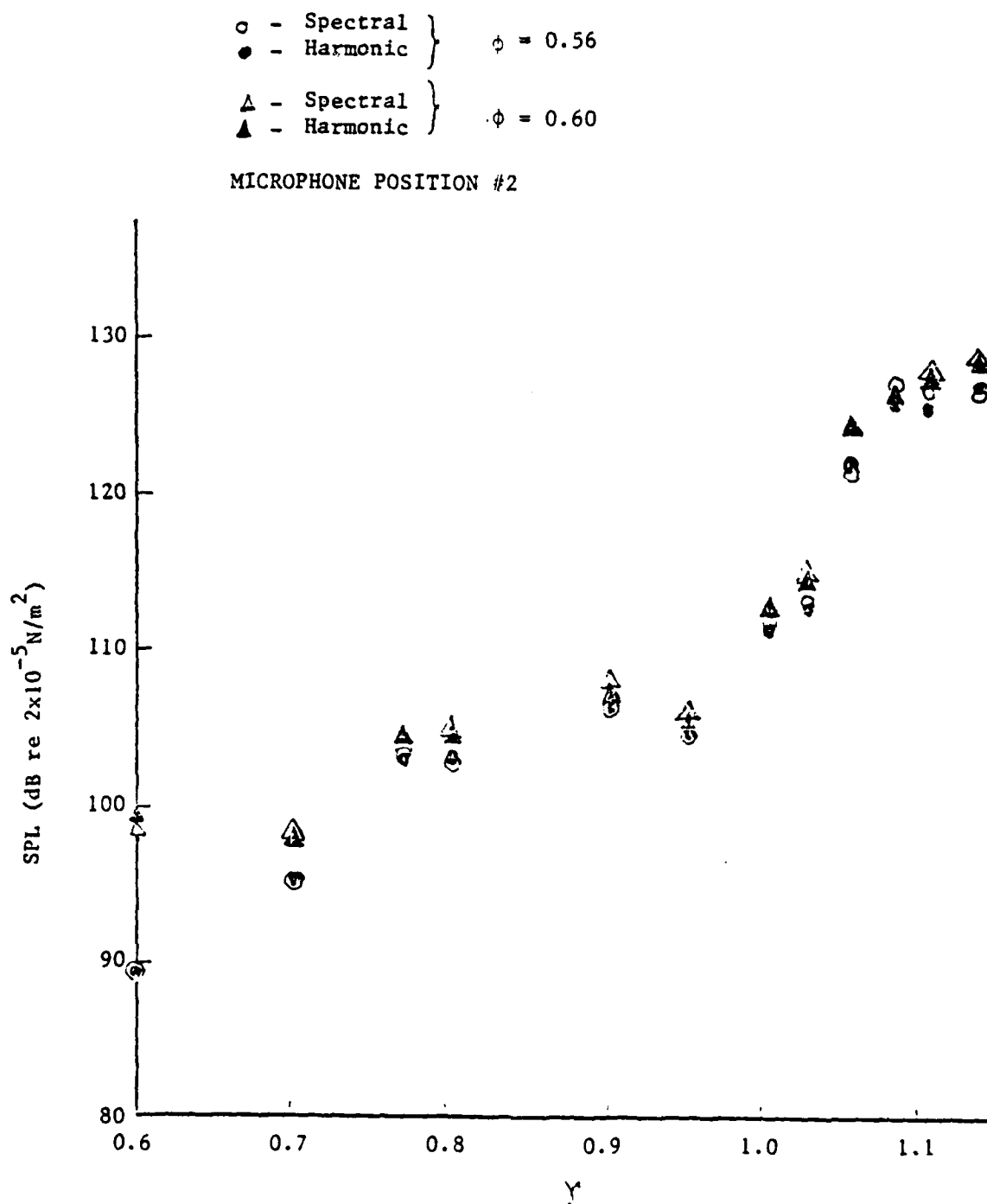


Figure D1. Comparison of Spectral to Harmonic SPL Data
 (a) 8-Cycle Screen Data

○ - Spectral } $\phi = 0.56$
 ● - Harmonic }

△ - Spectral } $\phi = 0.60$
 ▲ - Harmonic }

MICROPHONE POSITION #2

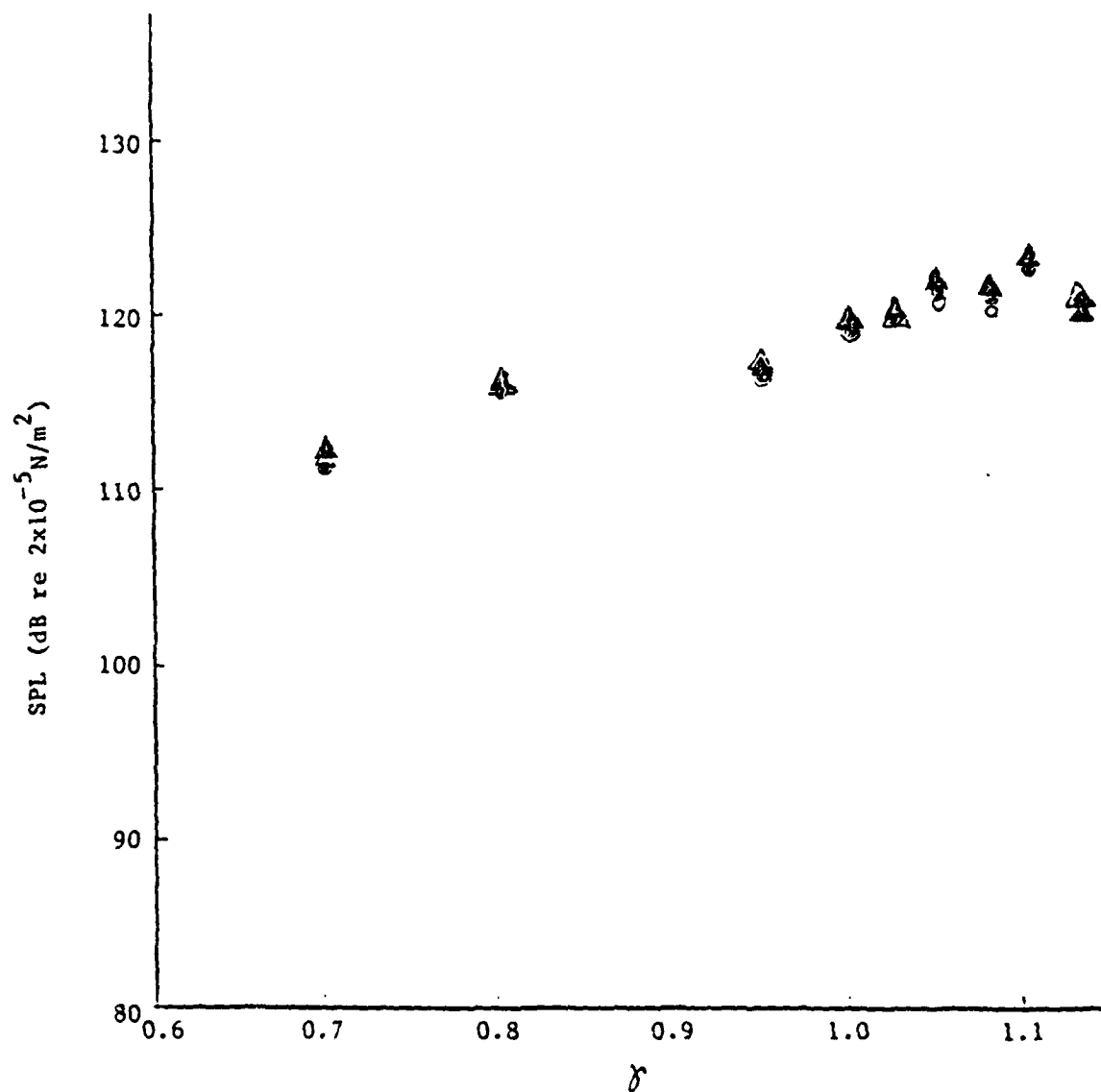


Figure D1. (b) 9-Cycle Screen Data

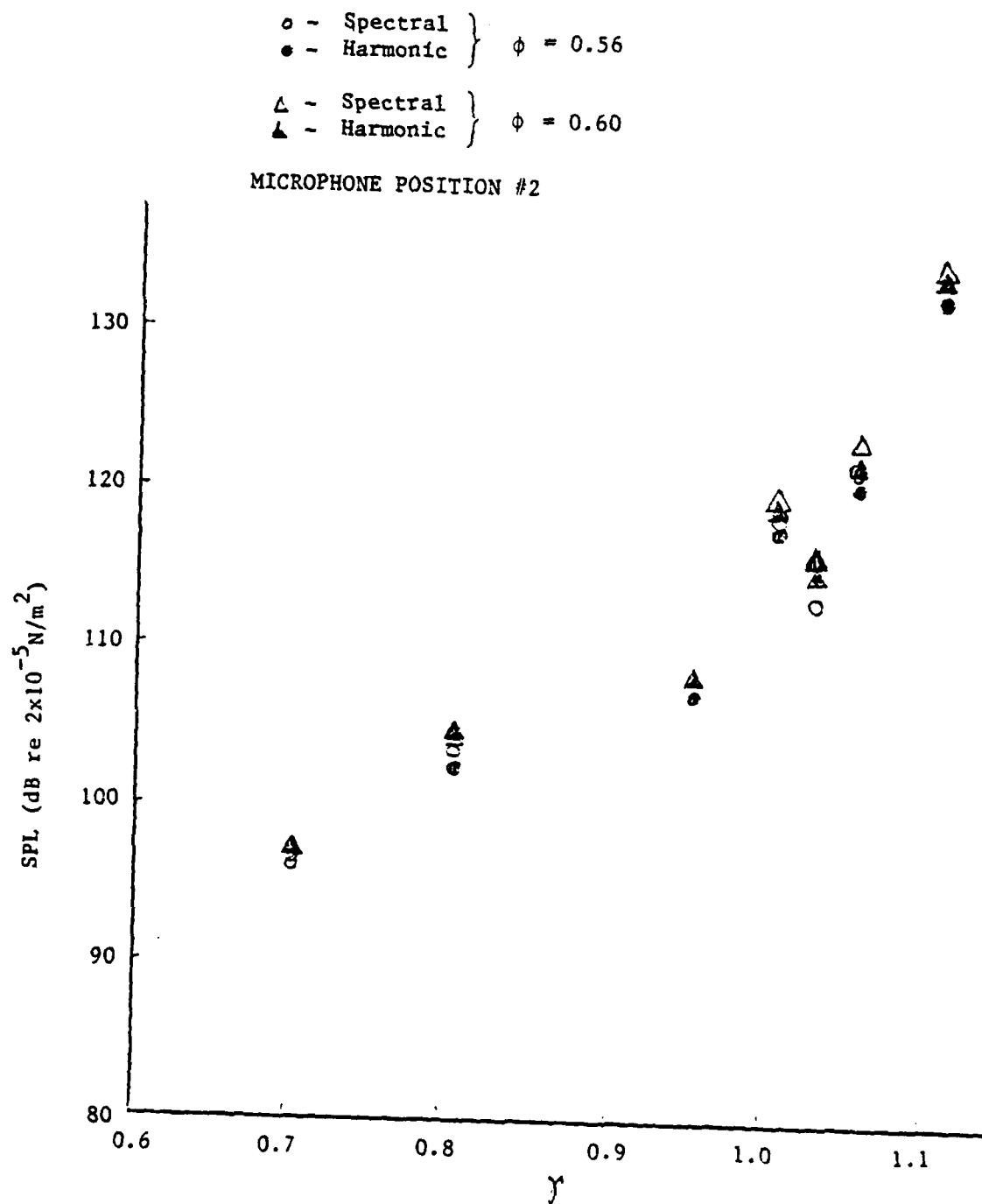


Figure D1. (c) 10-Cycle Screen Data

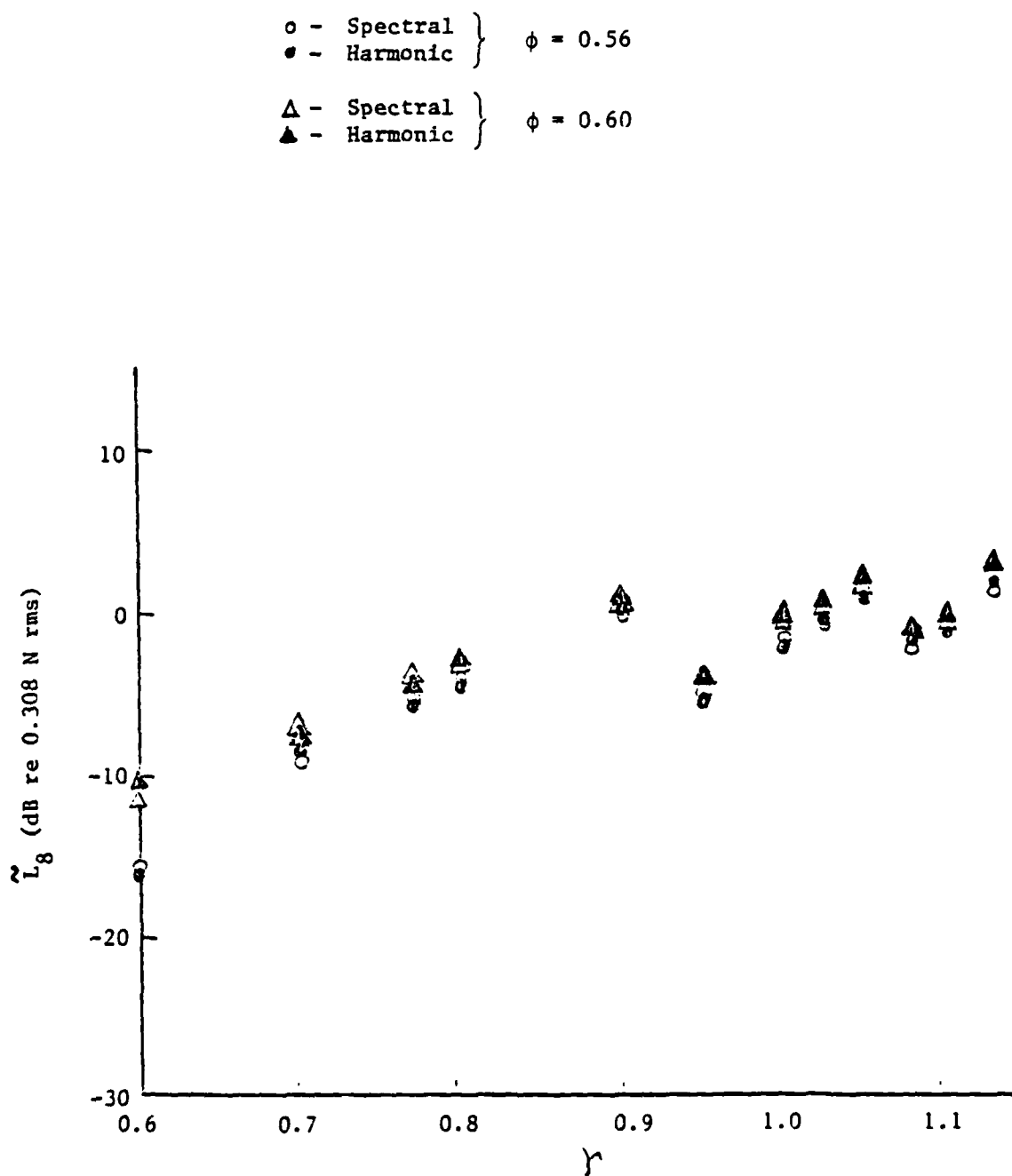


Figure D2. Comparison of Spectral to Harmonic Unsteady Lift Data
 (a) 8-Cycle Screen Data

○ - Spectral } $\phi = 0.56$
 ● - Harmonic }
 △ - Spectral } $\phi = 0.60$
 ▲ - Harmonic }

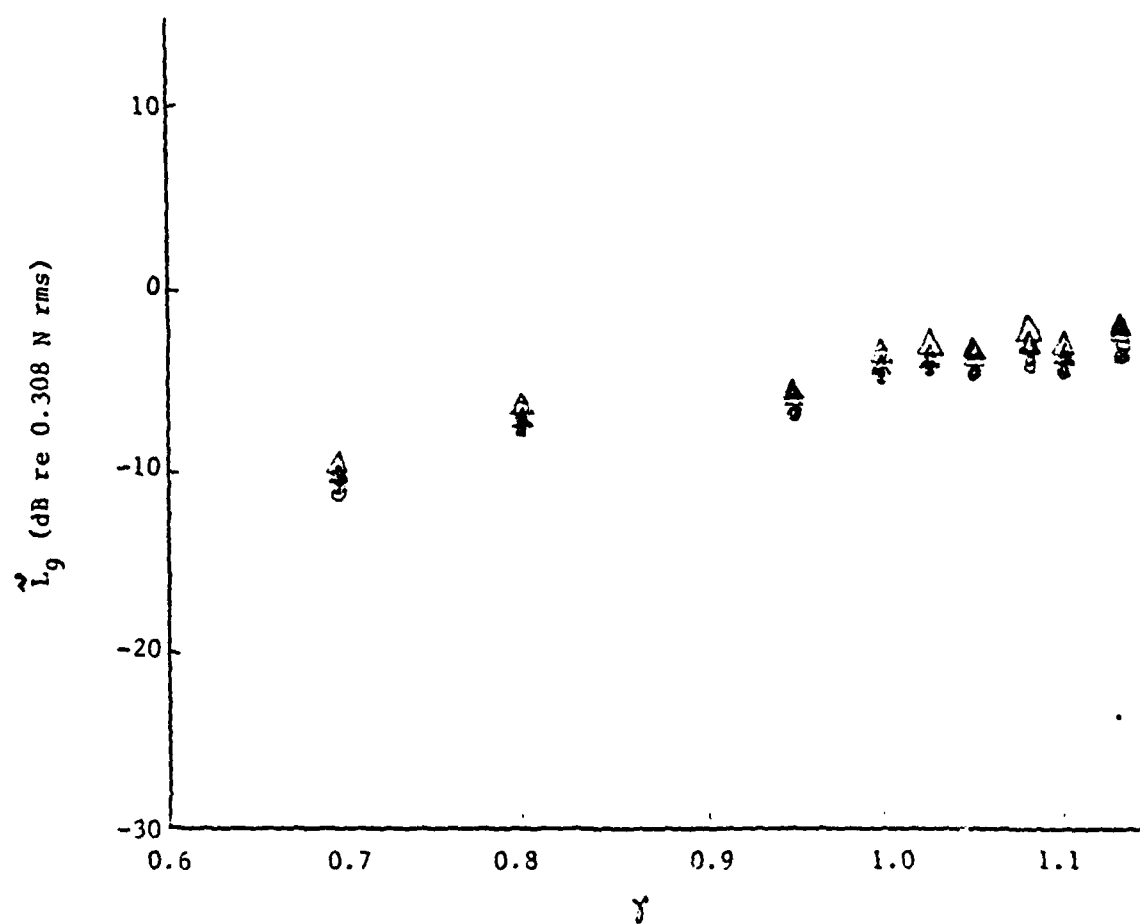


Figure D2. (b) 9-Cycle Screen Data

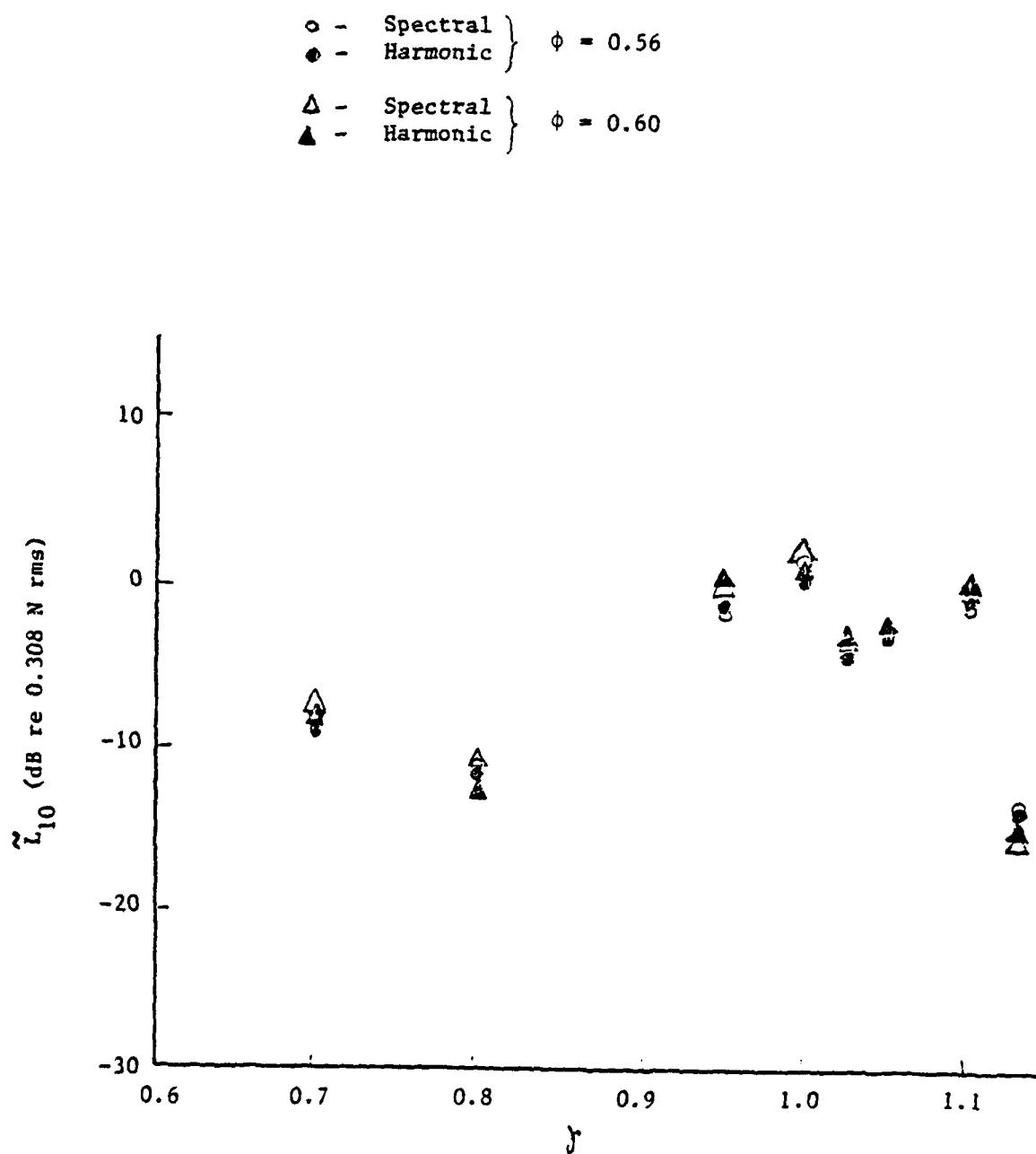


Figure D2. (c) 10-Cycle Screen Data

DISTRIBUTION LIST FOR TM 82-137

Commander (NSEA 0342)
Naval Sea Systems Command
Department of the Navy
Washington, DC 20362

Copies 1 and 2

Commander (NSEA 9961)
Naval Sea Systems Command
Department of the Navy
Washington, DC 20362

Copies 3 and 4

Defense Technical Information Center
5010 Duke Street
Cameron Station
Alexandria, VA 22314

Copies 5 through 10

INVESTIGATION OF THE COUPLING OF UNSTEADY LIFT TO LOW
ORDER ACOUSTIC DUCT MODES IN AN AXIAL FLOW FAN

James P. Cowan

Technical Memorandum
File No. TM 82-137
June 17, 1982
Contract No. N00024-79-C-6043

Copy No. _____

The Pennsylvania State University
Intercollege Research Programs and Facilities
APPLIED RESEARCH LABORATORY
Post Office Box 30
State College, PA 16801

APPROVED FOR PUBLIC RELEASE
DISTRIBUTION UNLIMITED

NAVY DEPARTMENT

NAVAL SEA SYSTEMS COMMAND

DISTRIBUTION LIST FOR TM 82-137

Commander (NSEA 0342)
Naval Sea Systems Command
Department of the Navy
Washington, DC 20362

Copies 1 and 2

Commander (NSEA 9961)
Naval Sea Systems Command
Department of the Navy
Washington, DC 20362

Copies 3 and 4

Defense Technical Information Center
5010 Duke Street
Cameron Station
Alexandria, VA 22314

Copies 5 through 10